

ABSTRACT

Study of Pumping Conditions on Output of
Optically Pumped Interband Cascade Lasers

Kyler A. Stephens, M.S.

Mentor: Linda J. Olafsen, Ph.D.

This thesis presents the results of optically pumping two interband cascade laser (ICL) semiconductor samples and measuring both their output power and spectral data. The samples were prepared by the Naval Research Laboratory using molecular beam epitaxy. These samples were pumped with a Nd:YAG laser in conjunction with an optical parametric oscillator that allowed for tunable pump beam wavelength. The peak output power from the samples was plotted versus pump intensity to create light-light curves. A novelty of this work was that the ICLs were optically pumped with a range of pump wavelengths from 1800 nm to 1950 nm. Additionally, the temperature of the sample was varied from 80 K to 220 K. The temperature dependence of threshold pump intensity as well as slope efficiency of ICL semiconductor samples is discussed. Also, how the spectral output of the samples changes with temperature and pump wavelength is presented, particularly with respect to the effect of applying a graphene monolayer top contact to the ICL surface.

Study of Pumping Conditions on Output of Optically Pumped Interband Cascade Lasers

by

Kyler Stephens, B.S.E.E.

A Thesis

Approved by the Department of Electrical and Computer Engineering

Kwang Lee, Ph.D., Chairperson

Submitted to the Graduate Faculty of
Baylor University in Partial Fulfillment of the
Requirements for the Degree
of
Master of Science in Electrical and Computer Engineering

Approved by the Thesis Committee

Linda J. Olafsen, Ph.D., Chairperson

Seunghyun Kim, Ph.D.

Jonathan Hu, Ph.D.

Carolyn Skurla, Ph.D.

Accepted by the Graduate School

August 2021

J. Larry Lyon, Ph.D., Dean

Copyright © 2021 by Kyler A. Stephens

All rights reserved

TABLE OF CONTENTS

LIST OF FIGURES	vi
LIST OF TABLES	xi
ACKNOWLEDGMENTS	xiii
DEDICATION	xiv
CHAPTER ONE	1
Introduction.....	1
CHAPTER TWO	5
Laser Theory and Background Information.....	5
General Laser Theory	5
Introduction to Semiconductors.....	8
Semiconductor Laser	16
Graphene	24
CHAPTER THREE	26
Methods and Experimental Setup	26
Laser and OPO	26
Beam Path	34
Spectrometer	42
Data Collection	45
Calibrations	46
Data Processing.....	50
ICL Samples.....	51
CHAPTER FOUR.....	54
Results.....	54
Light-Light.....	54
CHAPTER FIVE	75
Conclusion	75
APPENDIX A.....	78
LabVIEW Program Figures	78
OPO LabVIEW Control.....	78
Light-Light Program Control.....	81
APPENDIX B	86
Additional Data Tables	86
Center Wavelengths	86
Threshold Intensities.....	93

Slope Efficiencies	101
References.....	109

LIST OF FIGURES

Figure 1.1. Diagram of “W” active region employed in ICLs. The conduction band is shown in black, while the valence band is shown in red. The dashed black and red lines indicate quantized states for electrons and holes respectively [15].....	2
Figure 2.1. A visual representation of absorption, spontaneous emission, and stimulated emission [20]	7
Figure 2.2. Graphical representation of the difference between insulator, conductor (metal) and semiconductor energy bands [25].....	10
Figure 2.3. Plot of Fermi distribution for multiple temperature values [26].	11
Figure 2.4. Three different types of semiconductor heterostructures. Each is defined by the relationship between conduction and valence band minima and maxima. ΔE_v is the difference in valence band energies and ΔE_c is the difference in conduction band energies [29].....	13
Figure 2.5. An infinite square well potential with width d [30].	14
Figure 2.6. First two quantized energy levels in an infinitely deep Quantum well defined by Equation (2.12) [30].....	16
Figure 2.7. Example of a Type-I heterostructure like those used in diode lasers where the blue line is the conduction band and the red line is the valence band. The green trace represents the electron wave function, and the yellow/orange trace represents the hole wave function [32].....	17
Figure 2.8. Comparison of intersubband (right) and interband (left) transitions. The vertical red lines represent electron transitions and the horizontal red lines represent emitted photons. The solid lines represent conduction or valence bands, and the dashed lines are energy levels within the bands [33]	18
Figure 2.9. Simple diagram of intersubband transitions and the cascade arrangement. The red, solid black, and dashed lines are the same as those in Figure 2.7 [33]	18

Figure 2.10. More detailed depiction of the conduction band of a QCL. The straight black lines represent the conduction band, while the curved red and black lines show electron potentials, which are found by solving the Schrödinger equation. The curved green lines represent emitted photons [34].....	19
Figure 2.11. 1.5 periods of an ICL showing the active, electron injection, and hole injection regions [36]	21
Figure 2.12. Diagram depicting how the semimetallic interface in an ICL is formed under bias. On the left, the overlap between a conduction and valence band is shown under no bias. On the right is the same overlap but with some bias. The holes (red circles) and electrons (blue circles) are repelled from the barrier, in the direction of the corresponding arrows, due to the applied field [37]	23
Figure 2.13. Graphene, which is a single layer of hexagonally arranged carbon atoms [42]	24
Figure 2.14. Graphical example of an optically pumped ICL laser utilizing Graphene [43]	25
Figure 3.1. Four level transition diagram of Nd:YAG laser [45]	26
Figure 3.2. Energy level diagram for neodymium-doped yttrium aluminum garnet [45].....	27
Figure 3.3. Diagram of Q-switch inside of the pump laser used in this Procedure [45].....	29
Figure 3.4. A very general model of how an OPO crystal is utilized [46]	30
Figure 3.5. Basic schematic of the beam path for this procedure with all lenses, windows and other optical equipment. See table 3.1 for the key to each listed number	35
Figure 3.6. Both samples mounted on the copper block with silver paint. The top sample did not have graphene, while the bottom sample had a graphene contact.	38
Figure 3.7. Picture of nitrogen dewar, transfer line, sorption vacuum pump, and cryostat setup.....	39
Figure 3.8. Close up picture of the cryostat used in this procedure.....	40
Figure 3.9. Depiction of the beam path from the cryostat to the Judson Detector [43]	41

Figure 3.10. Top down diagram of beam path from cryostat to spectrometer.....	41
Figure 3.11. Diagram of the Horiba iHR 550 Spectrometer that was used to collect spectral data for this thesis [47].....	43
Figure 3.12. Relative spectral response for the DSS-IS020L detector [48].....	44
Figure 3.13. Illustration of the knife edge method of beam profile collection. (a through (h) diagrams how the knife edge is used to progressively block more and more of the pump beam. (i) shows the corresponding intensity data points for (a) though (h). (j) shows the derivative of (i), which is the actual beam profile [50].....	46
Figure 3.14. Plot of pulse duration response verses pulse duration to show the necessary pulse duration to achieve a full detector response [50].....	49
Figure 3.15. Plot of pulse widths for the OPO idler at each of the pertinent pump wavelengths	49
Figure 3.16. Structure of optically pumped ICL [43].....	52
Figure 4.1 Plot of peak output power versus pump intensity for sample B at 1800 nm pump wavelength and 180 K	55
Figure 4.2 Fan of light-light curves for sample A over a range of temperatures being pumped at 1950 nm	57
Figure 4.3 Plot of light-light curves for sample B over a range of temperatures with a pump wavelength of 1950 nm.....	58
Figure 4.4 Threshold pump intensity versus temperature for samples A and B at 1950 nm pump. Exponential fits were applied to both curves and the relevant fit data is shown in the included tables	59
Figure 4.5 Plot of slope efficiency versus temperature for samples A and B 1950 nm pump wavelength.....	61
Figure 4.6 Fan of light-light curves for sample A at 100 K over a range of pump wavelengths	62
Figure 4.7 Fan of light-light curves for sample B at 100 K over a range of pump wavelengths	62
Figure 4.8 Plot of threshold intensity versus pump wavelength for samples A and B at 100 K. Linear fits were applied to both data sets and the pertinent fit data is included in the corresponding tables	63

Figure 4.9 Plot of slope efficiency versus pump wavelength for samples A and B at 100 K. Linear fits were applied to both data sets and the pertinent fit data is included in the corresponding tables	65
Figure 4.10 Spectral output of sample A at 80 K over a variety of pump wavelengths.....	67
Figure 4.11 Spectral output of sample B at 80 K over a variety of pump wavelengths.....	67
Figure 4.12 Spectral output of sample A at 1800 nm pump wavelength and temperatures from 80 K to 200 K	68
Figure 4.13 Spectral output of sample A at 1800 nm pump wavelength and temperatures from 80 K to 200 K	69
Figure 4.14 Center wavelength versus temperature for Sample A	70
Figure 4.15 Center wavelength versus temperature for Sample B	71
Figure 4.16 Range in sample A and B center wavelengths versus temperature	71
Figure 4.17 Plot of the change in center wavelength per degree Kelvin for both samples A and B. Linear fits were applied to both data sets and the pertinent fit values are shown in the included tables	74
Figure A.1 Connection control panel of OPO program.....	78
Figure A.2 Manual command input panel of OPO program	79
Figure A.3 The program control panel of OPO program.....	80
Figure A.4 The auto create new program panel of OPO program.....	80
Figure A.5 The manually create/edit program panel of OPO program	81
Figure A.6 The computer-controlled equipment panel of the light-light program.....	82
Figure A.7 The output file panel of the light-light program.....	82
Figure A.8 The instrument settings/general info file panel of the light-light program.....	83
Figure A.9 The experimental parameters panel of the light-light program	83

Figure A.10 The results/output panel of the light-light program.....84

Figure A.11 Block diagram of light-light program when doing a single scan. Not shown in this figure is the many sub layers in this loop, the loop doing configuration, and setup to the left of this figure, and the process of closing any opened files and putting equipment in standby mode to the right of this figure84

Figure A.12 Block diagram of light-light program when doing a hysteresis scan. Not shown in this figure is the many sub layers in this loop, the loop doing configuration, and setup to the left of this figure, and the process of closing any opened files and putting equipment in standby mode to the right of this figure85

LIST OF TABLES

Table 3.1. Descriptions of the optics and equipment listed in Figure 3.5.....	36
Table 3.2. FWHM data for the horizontal and vertical directions of the pump beam.....	47
Table 3.3. “W” active region layer thicknesses in angstroms (Å).....	51
Table 3.4. Semiconductor ICL Samples Used in This Thesis	52
Table 4.1 Change in center wavelength per degree Kelvin for both samples.....	73
Table B.1 Center wavelength data for Samples A and B over a range of temperatures being pumped at 1800 nm	86
Table B.2 Center wavelength data for Samples A and B over a range of temperatures being pumped at 1825 nm	87
Table B.3 Center wavelength data for Samples A and B over a range of temperatures being pumped at 1850 nm	88
Table B.4 Center wavelength data for Samples A and B over a range of temperatures being pumped at 1875 nm	89
Table B.5 Center wavelength data for Samples A and B over a range of temperatures being pumped at 1900 nm	90
Table B.6 Center wavelength data for Samples A and B over a range of temperatures being pumped at 1925 nm	91
Table B.7 Center wavelength data for Samples A and B over a range of temperatures being pumped at 1950 nm	92
Table B.8 Threshold pump intensity data plotted in Figure 4.4. Samples A and B at 1950 nm pump wavelength.....	93
Table B.9 Threshold pump intensity data for Samples A and B at 1925 nm pump wavelength.....	94

Table B.10 Threshold pump intensity data for Samples A and B at 1900 nm pump wavelength.....	95
Table B.11 Threshold pump intensity data for Samples A and B at 1875 nm pump wavelength.....	96
Table B.12 Threshold pump intensity data for Samples A and B at 1850 nm pump wavelength.....	97
Table B.13 Threshold pump intensity data for Samples A and B at 1825 nm pump wavelength.....	98
Table B.14 Threshold pump intensity data for Samples A and B at 1800 nm pump wavelength.....	99
Table B.15 Threshold pump intensity data plotted in Figure 4.8. Samples A and B at 100 K	100
Table B.16 Slope Efficiency data plotted in Figure 4.5. Samples A and B at 1950 nm pump wavelength.....	101
Table B.17 Slope Efficiency data for Samples A and B at 1925 nm pump wavelength	102
Table B.18 Slope Efficiency data for Samples A and B at 1900 nm pump wavelength	103
Table B.19 Slope Efficiency data for Samples A and B at 1875 nm pump wavelength	104
Table B.20 Slope Efficiency data for Samples A and B at 1850 nm pump wavelength	105
Table B.21 Slope Efficiency data for Samples A and B at 1825 nm pump wavelength	106
Table B.22 Slope Efficiency data for Samples A and B at 1800 nm pump wavelength	107
Table B.23 Slope Efficiency data plotted in Figure 4.9. Samples A and B at 100 K.....	108

ACKNOWLEDGMENTS

I cannot express enough thanks and gratitude to my advisor Dr. Linda Olafsen. My journey to completing my degree at Baylor was not without its challenges, and Dr. Olafsen's patience and compassion were such a blessing. Simply put, I could not have asked for a better advisor.

I also would like to thank Daniella Sugijanto for being such a kind and helpful lab partner.

Thank you to all of my committee members, Dr. Jonathan Hu, Dr. Seunghyun Kim, and Dr. Carolyn Skurla, for setting aside time to help me complete this thesis work.

Patrick Hynan deserves immense thanks for always helping to solve more IT issues than I care to mention. Specifically, thank you for all your help in replacing the iHR laptop while I was trying to finish data collection.

Thank you to Dr. Meyer and his team at the Naval Research Laboratory who designed and produced the samples for this work. A special thanks to Dr. Tour and his associates at Rice University for growing and transferring the needed graphene.

I want to say thank you to both my parents and my in-laws. You have all taught me how to be a man, husband, student, and so much more. I am so thankful for your support and wise advice.

Finally, I couldn't imagine trying to earn my degree without the love and support of my wife. She made all the work worth it, and I appreciate her keeping our lives in order on the days that I was too busy working. She is truly special.

DEDICATION

To Megan and Cove. I love you more than you know.

CHAPTER ONE

Introduction

The development of the first functional interband cascade lasers (ICL) in the mid 1990's provided researchers with a novel method of generating mid-infrared (mid-IR) light, which is in the range $3.0 \mu\text{m} \leq \lambda \leq 6.0 \mu\text{m}$ [1,2]. The mid-IR region of the electromagnetic spectrum is of particular interest because it is a range where many trace chemicals can be detected sensitively. These chemicals include greenhouse gases, methane, carbon monoxide, carbon dioxide, formaldehyde, and many others. Knowing this, ICLs can feasibly be used by numerous different industries and areas of research that need accurate methods of detecting trace chemicals [3].

While ICLs have become particular popular, this was not always the case. At their first development, diode lasers and quantum cascade lasers (QCLs) were already being used as mid-IR light sources [4]. Shorter wavelength lasers function well at room temperature [5]. However, the efficiency of diode lasers greatly decreases at output wavelengths above $3 \mu\text{m}$ [6]. QCLs function well above $4 \mu\text{m}$ output at room temperature [7]. However, below $4 \mu\text{m}$ QCLs struggle with poor carrier and phonon scattering as well as insufficient conduction band offset [8].

For many years, ICLs did not function at room temperature, which made it much more difficult for widespread use. However, increased temperature functionality allowed for ICLs to become the definitive choice for mid-IR output [9]. ICLs combine the benefits of QCL cascading photon production with the long carrier lifetime of diode

lasers to make a laser that is efficient at the mid-IR region of the electromagnetic spectrum. The general ICL design has seen many improvements since the first generation [10]. The introduction of the “W” active region [11], which is diagrammed in Figure 1.1, as well as the addition of hole injection regions [8,12] drastically improved the threshold current density (J_{th}) and laser efficiency. This is evidenced by the difference in threshold current between ICLs before the incorporation of the “W” active region. Without “W” active regions, ICLs had threshold current densities of more than 6 kA/cm² at room temperature [8]. In 1998 an ICL using “W” active regions was experimentally confirmed to have a threshold current density of approximately 2 kA/cm² at 240 K [13]. Additionally, ICLs have achieved J_{th} of approximately 1 kA/cm² at 200 K [7]. Future research involves the development of ICLs with continuous wave operation at and above room temperature [12] and decreasing the threshold power needed for operation [14].

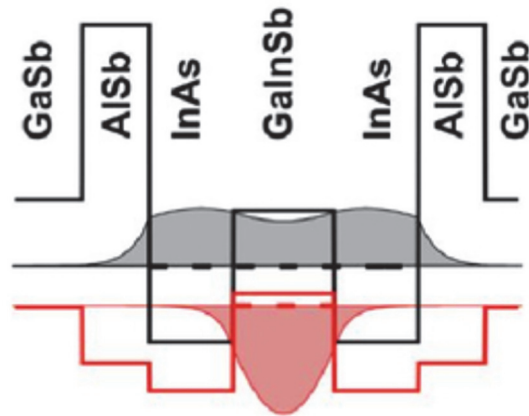


Figure 1.1. Diagram of “W” active region employed in ICLs. The conduction band is shown in black, while the valence band is shown in red. The dashed black and red lines indicate quantized states for electrons and holes respectively [15].

The limiting factor preventing efficient room temperature operation and decreased operating threshold power are not well understood. Semiconductor models indicate that increasing the number of stages in an ICL should have no effect on quantum efficiency

[16]. However, in practical applications, a decrease in quantum efficiency is seen per stage in an ICL with increasing current density [17]. This phenomenon is seen at and above room temperature. The reason for this drop in quantum efficiency has been attributed to non pinning of spontaneous emission at high temperature operation [6]. Ideal laser models predict pinning of carrier concentration [18]. Instead, non-pinning of carrier concentration at current densities above J_{th} corresponds to increases internal loss and decreases efficiency, because the extra carriers above threshold contribute to spontaneous or non-radiative emission rather than stimulated emission [6].

The work presented in this report attempts to understand how pumping conditions affect the outputted performance of optically pumped ICLs. The pumping conditions that were varied were pump intensity, pump wavelength, and sample temperature. The ICLs that were observed in this procedure were optically pumped in order to better understand hole and electron dynamics within the materials. The two samples used were from the same epitaxial growth with identical layering, except for the application of a monolayer of graphene to one of them. Graphene is a single layer of carbon atoms that is highly thermally, electrically, and optically conductive. While optically pumped samples are not intended to replace electrically stimulated alternatives for practical applications, with further development optical pumping methods can be useful for understanding carrier distribution and sources of loss in semiconductor ICLs.

Important findings in this thesis include the variation of sample center wavelength with temperature and with pump wavelength. Other results include how threshold intensity and slope efficiency of the samples, both with and without a monolayer of graphene, change with pump wavelength and temperature.

Chapter Two provides a brief introduction to laser theory as well as other pertinent background information. Chapter Thress presents the experimental setup and methods employed for data collection. The results of this experimental work are discussed in Chapter Four, and a summary and conclusion are provided in Chapter Five.

CHAPTER TWO

Laser Theory and Background Information

General Laser Theory

The first laser was demonstrated on May 16, 1960 by Theodore H. Maiman. By 2018, the laser market had developed into a \$12.9 billion industry, and lasers can be seen in many facets of everyday life as well as in cutting edge applications ranging from medicine to war fighting [19]. Despite their widespread use, lasers still captivate the imagination of many people and are the subject of much continued research and development.

The acronym LASER was first used by a Columbia University graduate student named Gordon Gould in November 1957. In his handwritten notebook, Gould coined the now famous term that stands for Light Amplification by Stimulated Emission of Radiation [19]. Two of the key characteristics that differentiate laser light from other forms of illumination are that lasers are monochromatic and collimated. Monochromatic means that a laser beam encompasses a very narrow spectrum of light, and collimated refers to the fact that the photons in a laser beam are all in phase and traveling in the same direction as each other. In other words, a laser beam is directional light as opposed to a light bulb that radiates light in all direction with no regard for phase. It is also common to hear the use of the word coherent to describe laser beams, as lasers are both spatially and temporally coherent.

Understanding how a laser functions begins by relating Planck's constant h , frequency ν , and energy E . Imagine that there is an atom that can exist in two different energy levels, E_1 and E_2 . In this scenario, E_2 is greater than E_1 . It is possible for an electron existing in energy level E_1 to be excited to E_2 through a process called absorption, where the electron absorbs the energy of an incident photon. However, in order for the transition to E_2 to occur the energy of the incident photon must be

$$E_p = h\nu \geq E_2 - E_1. \quad (2.1)$$

This equation simply means that the photon must have an energy greater than or equal to the difference in energy between the two defined states. Once an electron reaches the second energy level it will decay back to the first energy level through one of two processes: spontaneous emission or stimulated emission. Spontaneous emission is when the electron falls back to the lower state and emits a photon with energy

$$E_p = h\nu = E_2 - E_1. \quad (2.2)$$

This photon is not polarized and propagates in some random direction. Alternatively, if an excited electron comes in contact with a photon, another photon can be created with energy and direction matching that of the incident photon, also known as stimulated emission. Absorption, spontaneous emission, and stimulated emission are graphically shown in Figure 2.1. E_1 and E_2 denote two different energy levels, and each of the three figures shows how an electron can either be excited to a higher energy level or decay to a lower energy level. Each instance of $h\nu$ represents a photon.

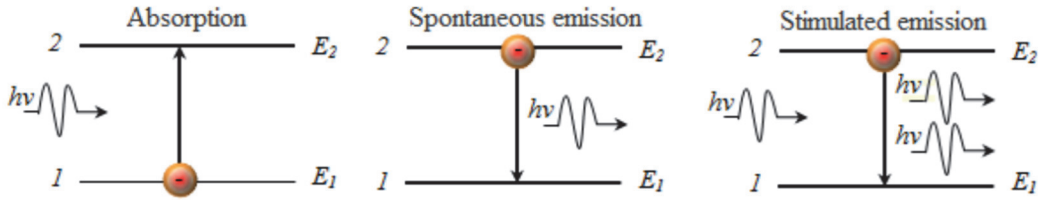


Figure 2.1. A visual representation of absorption, spontaneous emission, and stimulated emission [20].

The first of three requirements to produce a laser is population inversion [21].

Imagine that the populations of, or number of electrons occupying, the previously mentioned energy levels are N_1 and N_2 respectively. The Boltzmann distribution gives the following relationship in thermal equilibrium.

$$\frac{N_2}{N_1} = e^{\frac{-(E_2-E_1)}{k_B T}} \quad (2.3)$$

In the above equation, k_B is Boltzmann's constant and T is temperature in Kelvin. In the Boltzmann distribution, $N_1 \geq N_2$ at all times. As the difference between energy levels increases the disparity between N_1 and N_2 increases proportionally. As temperature increases so too does N_2 . However, for electrons obeying the Boltzmann distribution, it is not possible for N_2 to exceed N_1 [22]. The only way to produce a population inversion is with some form of external stimulation or pumping to inject electrons into the upper state. The most common form of external pumping is electrical. In this process, a material is doped with extra electrons, holes, or a combination of the two. These extra carriers (electrons and/or holes) produce the necessary conditions, under sufficient current injection, for a population inversion to occur where $N_2 > N_1$. Additionally, pumping can be done optically, chemically, or thermally.

The next requirement for a laser is a gain medium. A gain medium is the material that is stimulated in order to produce the population inversion and to achieve amplification. Almost any material could be a gain medium under the right excitation conditions. However, modern gain media are most commonly made of gas, semiconductor material, or a solid state crystal [20].

Finally, a laser requires a resonator in order to function. A resonator is a cavity that reflects the photons emitted in the gain medium back through the gain medium [20]. These multiple passes allow for the emitted photons to produce more stimulated photons by coming in contact with excited electrons in the gain medium. In its simplest form, a resonator would be comprised of two mirrors. The mirrors would be placed opposite of each other with the gain medium between them. One mirror would be perfectly reflective while the other would only be partially reflective. In this arrangement, a fraction of the photons escape in the form of a laser beam each time they come in contact with the partially reflective mirror. The reflected photons pass through the gain medium, reflect off of the perfectly reflective mirror, pass through the gain medium a second time, and come in contact with the partially reflective mirror again so that the process is repeated. Through stimulated emission, new photons are created as existing photons reflect back and forth across the gain medium in the resonator.

Introduction to Semiconductors

Semiconductor Characteristics

There are three different types of materials when it comes to electrical resistivity. Insulators are materials that have electrical resistivity greater than $10^9 \Omega \text{ cm}$ [23]. This

high resistivity prevents any significant flow of current. Conductors are materials that have electrical resistivities less than $10^{-2} \Omega \text{ cm}$ [23]. The low resistivity of conductors means that current flows with very little disruption. The group of materials that have resistivity values between those of the conductors and insulators are referred to as semiconductors [23].

Electrons in a semiconductor material occupy one of two energy bands known as the conduction band and valence band. The energy of the conduction band is greater than that of the valence band. However, the population of electrons is greater in the valence band when compared to the conduction band population. An energy gap (E_g) separates the two bands, and the gap is the difference between the minimum conduction band energy (E_c) and the maximum valence band energy (E_v):

$$E_g = E_c - E_v. \quad (2.4)$$

The energy gap of a semiconductor material is often measured in electron volts (eV), and a typical semiconductor material has an energy gap between zero and 4 eV. It is important to note that in the absence of doping or defects there are no electron states within the band gap [24]. Electrons can only occupy states above or below the band gap.

Figure 2.2 shows a depiction for better understanding the separation of conduction and valence bands in insulators, conductors, and semiconductors. The conduction band is the upper grey box in each material, and the valence band is the lower box filled with dots, which represent electrons. In an insulator, the band gap is very large such that it requires a large amount of energy to excite an electron from the valence band to the conduction band. Thus, there is little to no flow of electrons in these materials. In a conductor or metal, the conduction and valence bands are very close together or even

overlapped. This results in a partially filled conduction band that requires very little energy to excite and flow electrons. A semiconductor has two distinct, non-overlapping, bands. However, the gap between the two bands is relatively small, such that relatively little energy (< 4 eV) is required to excite electrons from the valence to conduction band [23].

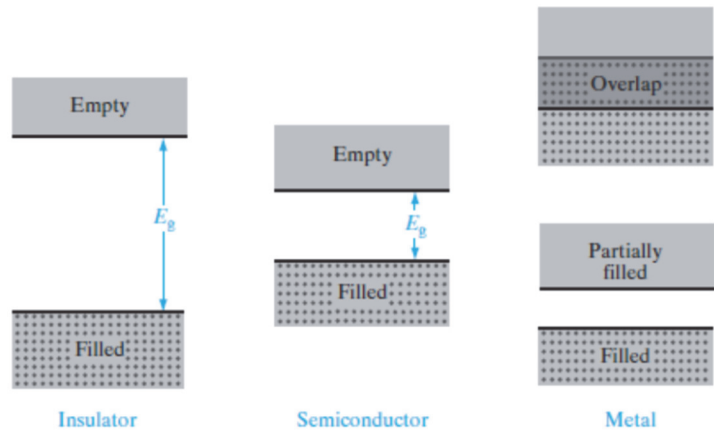


Figure 2.2. Graphical representation of the difference between insulator, conductor (metal) and semiconductor energy bands [25].

The equation that describes the probability of a given energy state being occupied by an electron is referred to as the Fermi-Dirac distribution function.

$$f(E) = \frac{1}{e^{\frac{E-E_F}{k_B T}} + 1} \quad (2.5)$$

Where E is the band energy and E_F is the fermi energy, which depend upon the material, doping, and temperature. To better understand the equation and electron occupation and probabilities, assume that the temperature is very close to 0 K. This would make the denominator of the exponential very small. Thus, when $E > E_F$ is true, the entire equation goes to 0. However, when $E < E_F$ is true, the entire equation goes to 1. The

transition between 0 and 1 occurs at $E = E_F$. Figure 2.3 shows a plot of Equation 2.2 for several different temperatures. The Fermi distribution curve develops a more gradual curve with increasing temperature.

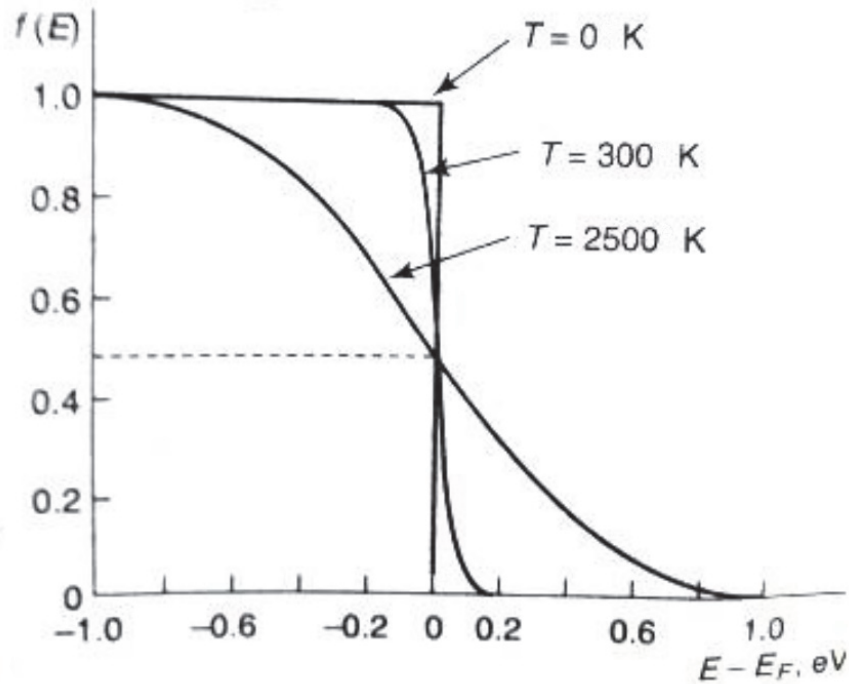


Figure 2.3. Plot of Fermi distribution for multiple temperature values [26].

Heterostructures

In addition to external stimulation or pumping, doping is an effective way of increasing the carrier density in semiconductor materials. This is done by artificially adding impurities to generate extra holes or electrons in a semiconductor to create a *p*-type or *n*-type material, respectively [25].

The simplest composite semiconductor materials are made up of a single homojunction. A homojunction is when a *p*-type semiconductor and an *n*-type semiconductor composed of the same base material (e.g. silicon) are put together. Due to the concentration gradient, the electrons diffuse to the *p*-side and the holes diffuse to the

n-side. The charge separation creates a field that attracts charge carriers back across the junction. This movement of holes and electrons creates a small current in the semiconductor material. In equilibrium, the drift current due to the field is balanced by the diffusion current due to the concentration gradient across the junction.

A heterojunction is similar to a homojunction. However, in a heterojunction, the two semiconductors being joined together are not made up of the same base material. The two materials being used are typically lattice-matched, and most commonly have different band gaps. The difference in band gaps means that the conduction and valence bands of the two materials do not lie at the same energy levels. This discontinuity is referred to as a band offset. The conduction band offset, ΔE_C it can be calculated as the difference between the electron affinities of the two materials [27]:

$$\Delta E_C = \chi_A - \chi_B \quad (2.6)$$

The electron affinity (χ) is the amount of energy required for one electron at the conduction band edge (minimum conduction band energy) to be completely free from the crystal structure [25, 28]. Multiple heterojunctions can be combined to form a heterostructure.

There are three different classifications of heterostructures. Figure 2.4 shows a visual depiction of the three different types. Type-I structures are such that the conduction band energy of material A is less than that of material B and the valence band energy of material A is greater than material B. Thus, the band gap of material A is completely within the band gap of material B. A type-II structure is one where both the conduction band energy and valence band energy of material A are less than that of material B. Because of this, the band gaps of the materials are staggered with respect to

each other. Finally, a type-III structure has the unique property that the conduction band energy of material A is less than the valence band energy of material B. This means that the band gaps of the two materials are completely separate from one another and do not overlap [29].

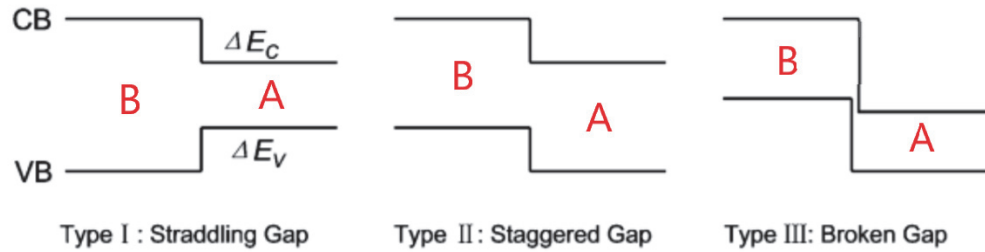


Figure 2.4. Depictions of the three different types of semiconductor heterostructures. Each is defined by the relationship between conduction and valence band minima and maxima. ΔE_v is the difference in valence band energies and ΔE_c is the difference in conduction band energies [29].

Quantum Wells

Heterojunctions can be used to make quantum wells (QW) in semiconductor materials. A quantum well is type of heterostructure where an electron or hole is trapped within an energy gap created by placing a narrow band gap semiconductor in-between two wide-gap semiconductors. As seen in Figure 2.5 the high walls of a QW, which are made by having a large energy gap between the conduction bands of the narrow and wide semiconductors, make it difficult for an electron to escape the QW through random excitation. Additionally, if the wide gap semiconductor materials are physically thick, carriers are unlikely tunnel through the barriers of the well [30].

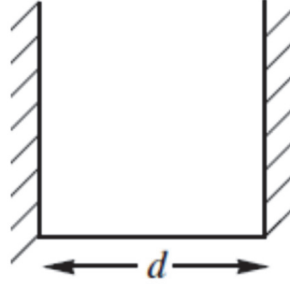


Figure 2.5. An infinite square well potential with width d [30].

The basic principles that define a quantum well are most easily described using an infinite square well. Even though the infinitely deep well is not physical, the energy levels can be solved for exactly analytically using the Schrödinger Equation. In this model, shown in Figure 2.5, a particle is capable of moving about the well. However, the well has walls of infinite potential that prevent the particle from leaving the well [31].

The infinite square well is described by the following one-dimensional potential.

$$V(z) = \begin{cases} 0 & \text{when } 0 \leq z \leq d \\ \infty & \text{otherwise} \end{cases} \quad (2.7)$$

To better understand the quantum well, observe equation 2.8, which shows Schrödinger's equation in one dimension.

$$-\frac{\hbar^2}{2m} \frac{d^2\psi}{dz^2} + V(z)\psi = E\psi \quad (2.8)$$

In equation 2.8, $V(z)$ is the same as defined above in equation 2.7. Additionally, \hbar is the modified Planck constant $\left(\frac{h}{2\pi}\right)$, m is the mass of the trapped particle, ψ is the wave function in one dimension, and E is the particle's total energy. The Schrödinger equation can be simplified by applying equation 2.4 as follows.

$$-\frac{\hbar^2}{2m} \frac{d^2\psi}{dz^2} = E\psi \quad (2.9)$$

The above can also be written as,

$$\frac{d^2\psi}{dz^2} = -k^2\psi \quad (2.10)$$

where

$$k \equiv \frac{\sqrt{2mE}}{\hbar} \quad (2.11)$$

Through the application of boundary conditions, when $z = 0$ the wave equation (ψ) also equals zero. Additionally, the wave equation equals zero when $z = d$. Thus, two conclusions can be made. First, the solution to the Schrödinger equation must be proportional to $\sin(kz)$. Second, $k = \frac{n\pi}{d}$ for any positive integer n . The application of this solution results in quantized energy levels that are defined by equation 2.8 and shown in Figure 2.5 [30].

$$E_n = \frac{\hbar^2 k^2}{2m} = \frac{n^2 \pi^2 \hbar^2}{2md^2} \quad (2.12)$$

An actual semiconductor material would be better explained using a finite square well model where the potential at the edges of the well have some finite value. In this scenario, it is possible for particles to penetrate into the barriers of the well. The finite square well potential requires a numerical rather than exact analytical solution of the Schrödinger equation. However, the infinite square well is a very good first approximation of a quantum well and describes the general dependence of energy levels on well width and electron effective mass.

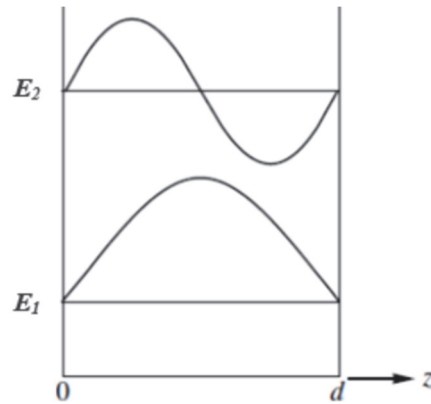


Figure 2.6. First two quantized energy levels in an infinitely deep quantum well defined by Equation (2.12) [30].

Semiconductor Laser

It was only a year after the demonstration of the first laser that the concept of a semiconductor laser was proposed. In 1962, the first laser using a semiconductor material for the gain medium was demonstrated. As previously described, a semiconductor laser requires both a resonator and a pump source. Additionally, semiconductor lasers not only can be electrically stimulated, as many lasers are, but can also be optically stimulated.

Diode Lasers

One of the simplest forms of semiconductor lasers is a diode laser. Figure 2.7 shows an example of a type-I interband diode laser. The type-I is directly related to the band configuration as shown in Figure 2.4, where the narrower band gap material is sandwiched between the wider-gap material. In this type-I example, both holes and electrons are confined within the QW of the heterostructure. Photons are emitted when interband transitions cause radiative electron-hole recombination. A laser such as the one shown in Figure 2.7, where electrons and holes recombine to emit photons, are called

bipolar lasers. In type-I lasers the band gap of the heterostructure materials limits the emitted light wavelength (λ), since

$$E = \frac{hc}{\lambda} \quad (2.13)$$

where c is the speed of light. The minimum photon energy must be equal to the separation of the energy levels in the conduction and valence bands of the quantum wells corresponding to a maximum emission wavelength.

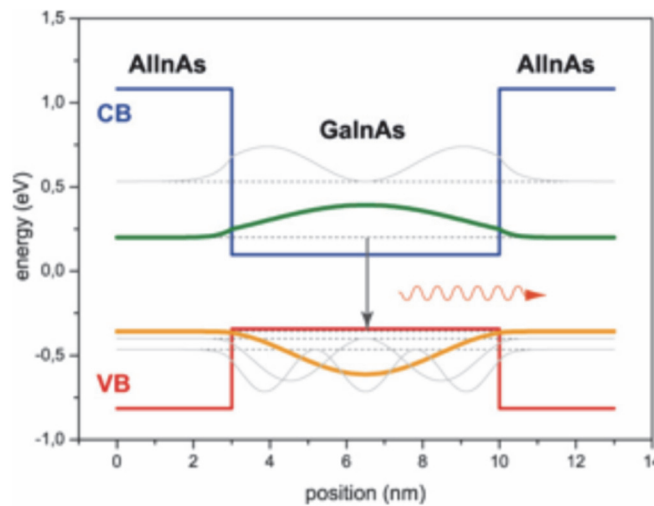


Figure 2.7. Example of a Type-I heterostructure like those used in diode lasers where the blue line is the conduction band and the red line is the valence band. The green trace represents the electron wave function, and the yellow/orange trace represents the hole wave function [32].

Quantum Cascade Lasers

Quantum Cascade Lasers (QCLs) are a form of laser that utilize intersubband transitions rather than the interband transitions that diode lasers use. Figure 2.8 shows the difference between intersubband and interband transitions. As the names may indicate, intersubband transitions are those that occur between quantized levels within the same band (conduction or valence) [4]. Interband transitions are those that occur between

conduction and valence bands. In QCLs, consecutive QWs with overlapping but dissimilar energy levels are placed side by side so that electron carriers can tunnel from the low conduction band energy level in one QW to a high conduction band energy level in another QW. A QCL has active regions, which are where an intersubband transition results in the emission of a photon [8,15]. Figure 2.9 shows a simple depiction of intersubband transitions in a cascade arrangement.

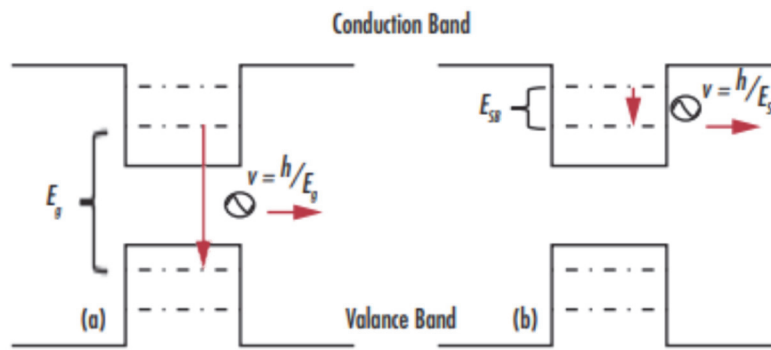


Figure 2.8. Comparison of intersubband (right) and interband (left) transitions. The vertical red lines represent electron transitions and the horizontal red lines represent emitted photons. The solid lines represent conduction or valence bands, and the dashed lines are energy levels within the bands [33].

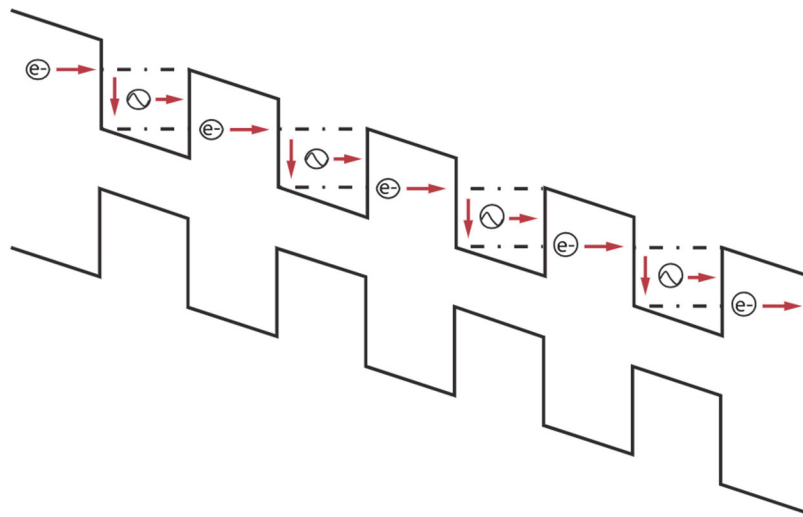


Figure 2.9. Simple diagram of intersubband transitions and the cascade arrangement. The red, solid black, and dashed lines are the same as those in Figure 2.7 [33].

Figure 2.10 shows a much more realistic view of how a QCL might be constructed to achieve the desired optical transitions and required tunneling to recycle electrons. There are many QWs, where emission does not occur, between each active region. These QWs are used by band gap engineers to tune the wavelength output of the QCL and control tunneling between stages. Unlike diode lasers, it is the epitaxial structure of the QCL (thickness and composition) that governs its output wavelength rather than the size of the band gap. The wavelength of the light can be tuned by changing the thicknesses of the QWs in the laser [8,15].

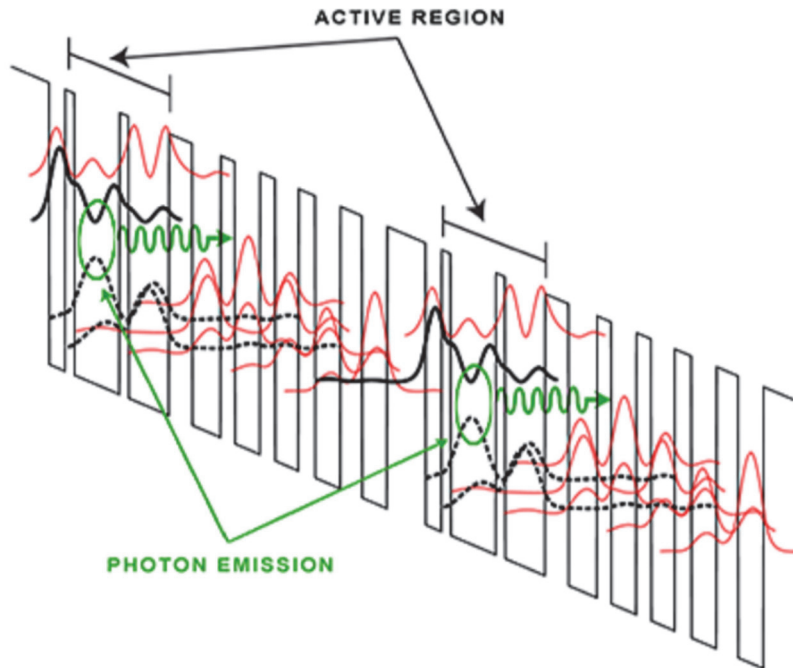


Figure 2.10. More detailed depiction of the conduction band of a QCL. The straight black lines represent the conduction band, while the curved red and black lines show electron wave functions, which are found by solving the Schrödinger equation. The curved green lines represent emitted photons [34].

QCL lasers typically have reduced threshold current density when compared to diode lasers. Threshold current density is the minimum current per unit area required for

stimulated emission to occur. Unfortunately, QCLs do require a higher threshold voltage than their diode counterparts. The threshold voltage must be greater than $\frac{M\hbar\omega}{q}$ where M is the number of QCL stages, $\hbar\omega$ is the photon energy, and q is the charge of an electron. An additional benefit of the QCL configuration is that cascading the electrons increases the gain of the laser and reduces the threshold power density required to operate the laser [8,15].

Interband Cascade Lasers

Another form of laser that builds upon those previously mentioned is the interband cascade laser. ICLs are typically designed to emit in the mid-IR region of the electromagnetic spectrum. The laser produces photons through recombination of electrons in the conduction band with holes in the valence band. Initially, this sounds very similar to how a diode laser functions. However, as the name states, the key differences is the cascade configuration that this laser employs [33].

To briefly introduce ICLs, it is important to know the three primary regions that make up one period of the laser. The optical transition region is the area where electron-hole recombination occurs to produce photons. While the first ICLs employed single type-II heterostructures, most ICL designs now use what is called a type-II ‘W’ active QW configuration [35] with a double quantum well. Each ICL period also has an electron injector and a hole injector. These regions each guide their respective carrier from one stage to the next stage so that more photons can be produced [6].

The first ICL was proposed in 1994 [3], which coincidentally was the same year that the QCL was initially demonstrated. However, the first experimentally functional ICL was not demonstrated until 1997 [19]. Initially, the QCL was much more popular

than the ICL. However, several key developments propelled the ICL into scientific prominence. The first ICLs that were built did not have the hole injector region in their structure. Within a few years of the first ICL being built, the hole injector became a staple of the modern ICL design [2]. Additionally, as mentioned before, scientists began using an active region in the “W” configuration [35]. Figure 2.11 shows 1.5 periods of a ICL under forward bias with a “W” active region, hole injector, and electron injector. The straight blue lines show the conduction band of the ICL structure. The red and blue arrows show the direction of hole and electron travel respectively. The wine and blue colored curves are electron wave functions, the red and green curves are hole wave functions, and the purple curved lines indicate photons. The “W” region gets its name from the shape of the conduction band formed by sandwiching the GaInSb hole well layer between two InAs electrons wells. The purpose of the “W” design is to produce greater optical gain through increased electron-hole wavefunction overlap [35].

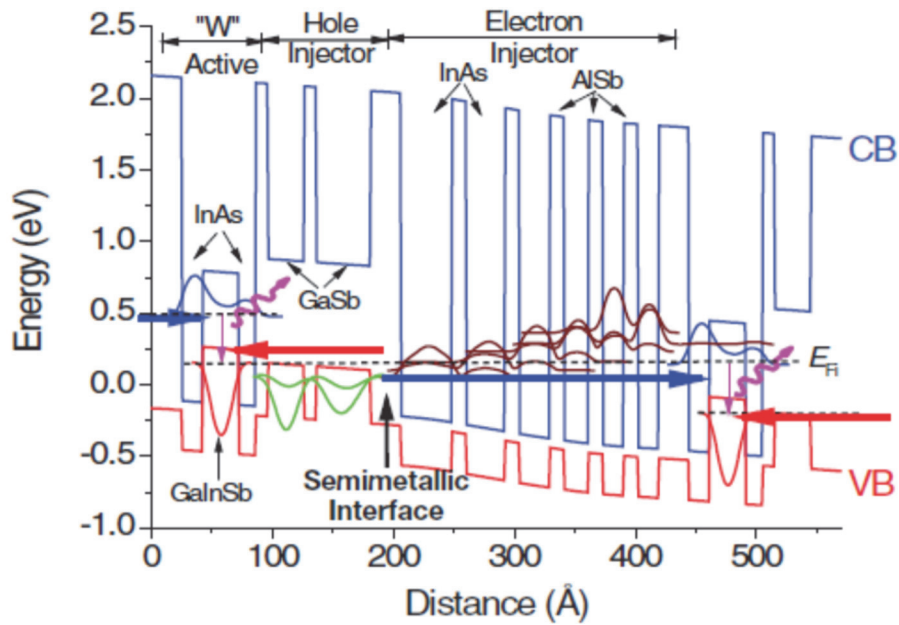


Figure 2.11. 1.5 periods of an ICL showing the active, electron injection, and hole injection regions [36].

Looking more closely at Figure 2.10 it is important to note the semimetallic interface between the hole and electron injectors. After an electron and hole recombine, the hole and electron injectors each help to guide their respective carrier to the next stage so that more photons can be emitted. Under biasing, the injectors generate additional carriers that will recombine to produce photons in the “W” wells. Without the semimetallic interface, electrons would be much more likely to tunnel back into the injector, instead of recombining with holes in the well. Instead, after recombination in the “W” well, electrons are then able to tunnel and scatter into the next electron injector’s conduction band to be reused in the next stage. This way, one electron can be used to produce multiple photons by generating one for every active stage that the laser has [2,17,36].

Figure 2.12 shows in more detail what occurs when the InAs/GaSb band edge forms a semimetallic barrier under bias. The left picture (a) shows the barrier in equilibrium, while the right picture (b) shows the barrier under bias. The solid blue lines represent the conduction band of InAs, and the solid red lines represent the valence band of GaSb. Under bias, a semimetallic overlap E_{SM} is generated that causes equal densities of electrons and holes to be created. The applied field under bias forces the holes and electrons to move away from the interface in opposite directions. The respective injectors then ferry the carriers to the next active region for photon generating recombination [37].

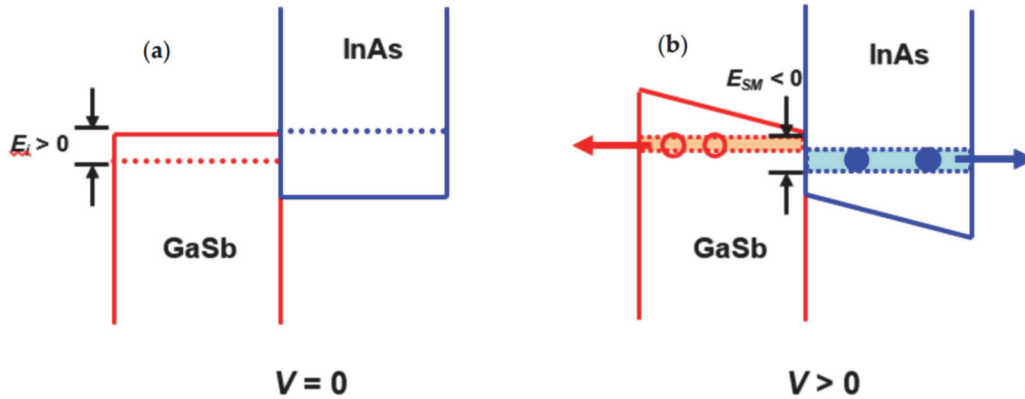


Figure 2.12. Diagram depicting how the semimetallic interface in an ICL is formed under bias. On the left, the overlap between a conduction and valence band is shown under zero bias. On the right is the same overlap but with some bias. The holes (red circles) and electrons (blue circles) are repelled from the barrier, in the direction of the corresponding arrows, due to the applied field [37].

One limitation of ICLs has always been decreased performance with increasing temperature. The first ICLs operated at cryogenic temperatures, and it was not until 2008 that the Naval Research Laboratory (NRL) developed the first ICL that functioned at room temperature. This laser had a threshold current density (J_{th}) of approximately 400 A/cm² [37]. Improvements have been made since then, and some ICLs have been shown to function with J_{th} as low as 100 A/cm² [38]. This is a great improvement from similar QCL lasers that have a J_{th} of approximately 800 A/cm² [39]. Where ICLs tend to decrease in efficiency is above room temperature. It is believed that this decrease in efficiency is due to non-pinning of carrier concentration. In a perfect laser, as forward bias increases above threshold so too does the carrier concentration. An increase in carrier concentration relates to photon density increase. An increase in photon density causes an increase in stimulated emission rate, which finally limits the carrier concentration from becoming excessive. In order for the above relations to be true, every additional injected electron-hole pair must recombine to produce a photon. Above room

temperature, this is found to not be true for ICLs [9, 15]. Researchers are still working to better understand and mitigate this phenomenon [6].

Graphene

Graphene is comprised of hexagonally arranged monolayer of carbon atoms as shown in Figure 2.13. It has become increasingly popular in recent years due to the fact that it is highly electrically and thermally conductive while also being optically transparent [40]. It has been shown that a single sheet of graphene only absorbs approximately 2.3% of visible light in the electromagnetic spectrum [41].

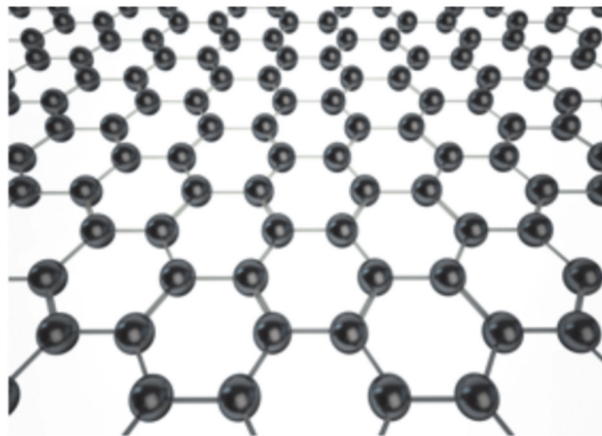


Figure 2.13. Graphene, which is a single layer of hexagonally arranged carbon atoms [42].

Graphene is studied here to explore its potential to allow for optical pumping of ICLs. Due to its optically transparent nature, continued research is being done to see if graphene can act as a transparent contact when applied to ICL samples. Figure 2.14 shows this arrangement of a graphene monolayer applied to an ICL sample, with the potential to optically pump under bias. The stimulated emission of the ICL is collected from the edge of the laser. Using graphene, any spontaneous emission can then be

measured in some other direction (e.g. surface) other than the stimulated emission edge. The ratio of spontaneous emission to stimulated emission can help researchers determine how effective the ICL material is at producing expected carrier concentration while being optically pumped [3,6,9,17].

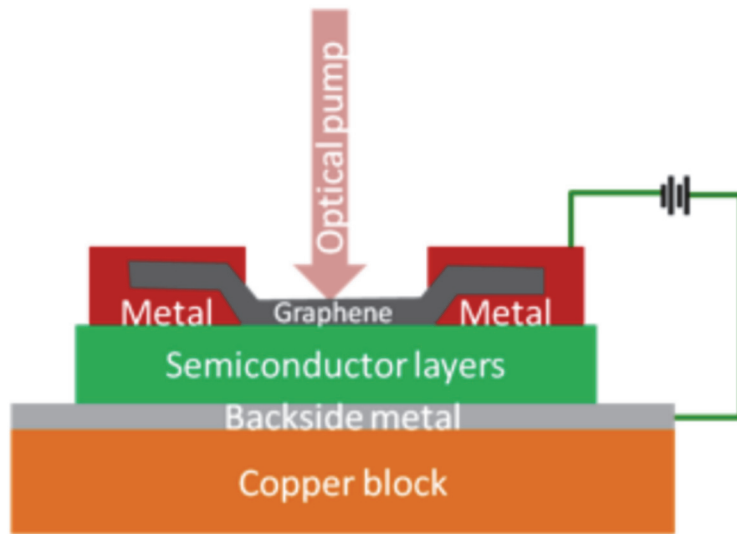


Figure 2.14. Graphical example of an optically pumped ICL laser utilizing graphene [43].

CHAPTER THREE

Methods and Experimental Setup

This chapter presents the details regarding experimental methods, equipment configuration, and data acquisition processes for acquiring light-light curves and wavelength spectra. Details about the sample ICL structures are included.

Laser and OPO

The laser used as the crux of the optical stimulation process for this data collection was a Spectra-Physics Quanta-Ray Model PRO 250-10 Pulsed Neodymium-Doped Yttrium Aluminum Garnet (Nd:YAG) laser. The transitions and functionality of Nd:YAG is highly documented and well studied [44,45], which makes it a common and reliable choice for laboratory settings that require a known pump wavelength. Figure 3.1 shows the four-level transition scheme for the Nd:YAG material, and Figure 3.2 shows the energy level diagram for Nd:YAG.

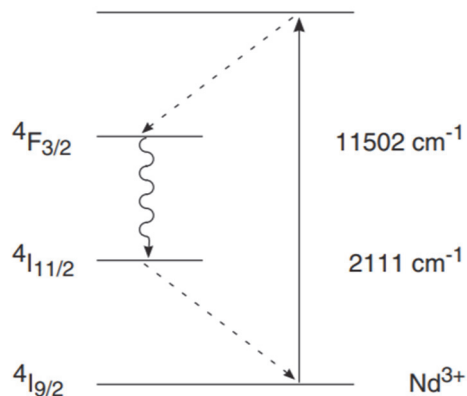


Figure 3.1 Four level transition diagram of Nd:YAG laser [45].

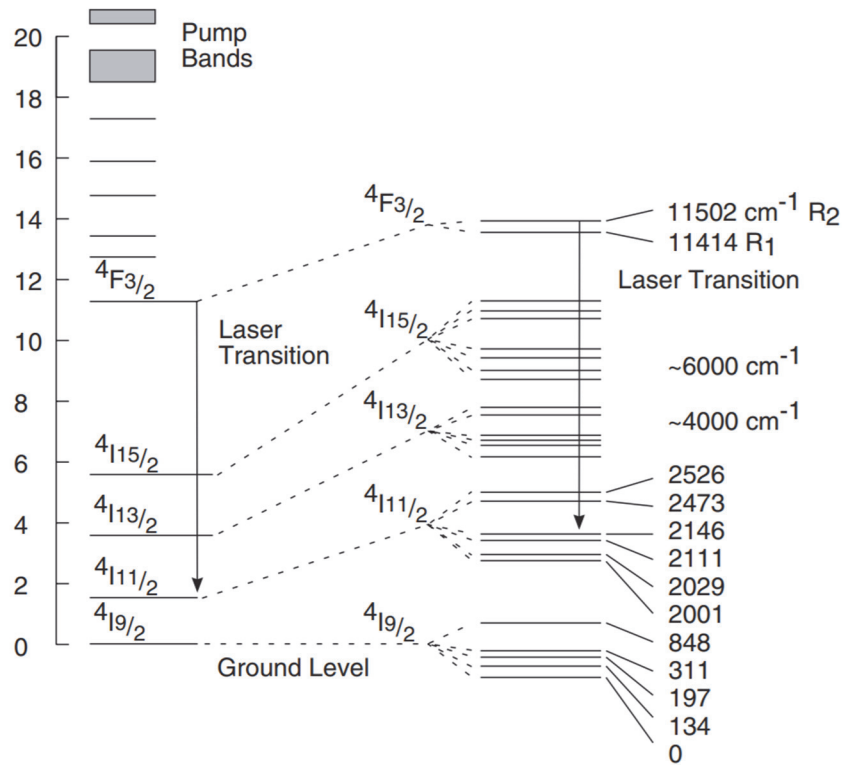


Figure 3.2 Energy level diagram for neodymium-doped yttrium aluminum garnet [45].

The Nd:YAG material has many different possible transitions and corresponding output wavelengths. However, the most probable transition is that from $F_{3/2}$ to $I_{11/2}$. Excited electrons are initially excited by the flash lamps to an upper pump band before quickly falling to $F_{3/2}$. Electrons remain at the $F_{3/2}$ level for approximately 230 μs before making the optical transition to $I_{11/2}$, which emits a photon at 1064 nm. Finally, the electron quickly falls from $I_{11/2}$ back to the ground state. The long time that an electron remains at $F_{3/2}$ and the quick transition from $I_{11/2}$ to ground result in a population inversion, which is a key facet of making this laser work. Additionally, the other transitions of Nd:YAG (1319, 1338, and 946 nm) all have higher thresholds and lower gain than that of the 1064 nm transition. Ultimately, this explains why 1064 nm is the most likely transition and the output wavelength of the Nd:YAG laser. When using this

Nd:YAG laser, there was a very specific power up sequence that was followed in order to ensure longevity in the life of the laser as well as proper functionality. Initially, the laser was put into a “lamps only” mode. In this stage, the flash lamps, which were used to optically pump the active medium, were turned on and allowed to warm up for approximately 20 minutes. Once the lamps had a sufficient time to warm up, the laser was put into long pulse mode, and finally a Q-switch mode. Each of these different stages allowed the laser to safely come to temperature as well as peak and stabilize its output power before being used to pump the optical parametric oscillator.

In order to produce the high peak output power that the Spectral-Physics laser is capable of, a Q-switch is used. The Q-switch causes the pulse of the laser to shorten while drastically increasing power. The Q-switch is made up of four components: a polarizer, Pockels cell, quarter-wave plate, and high reflector. The Q-switch functionality takes advantage of the fact that the upper lasing transition in Nd:YAG has a long lifetime. Because of this, a large population inversion is produced. By preventing oscillation, the population inversion can be maximized until the electrons can quickly transition together producing a high power laser pulse.

Figure 3.3 shows a diagram of how the components of the Q-switch are laid out in the Nd:YAG laser. The Pockels cell is a crystal that changes polarization depending on an applied voltage. While the population inversion is building, the Pockels cell has no voltage applied to it. Thus, as light passes through the polarizer, it is horizontally polarized. The horizontally polarized light passes through the Pockels cell with little to no attenuation. Next, the quarter-wave plate changes the light to circular polarization before it is reflected off of the high reflector. The circular polarized light is converted to

vertical polarization as it passes through the quarter-wave plate for a second time. With no voltage applied, the Pockels cell only passes horizontal polarized light. Once the population inversion has maximized, a voltage is applied to the Pockels cell which essentially adds another polarizing component to the path of the light. Now, rather than reflecting the light out of the resonator, the Pockels cell passes the reflected light through itself and into the cavity. When this occurs, all of the stored up energy in the cavity is dumped in a pulse with tens of megawatts of power and <10 ns pulse width.

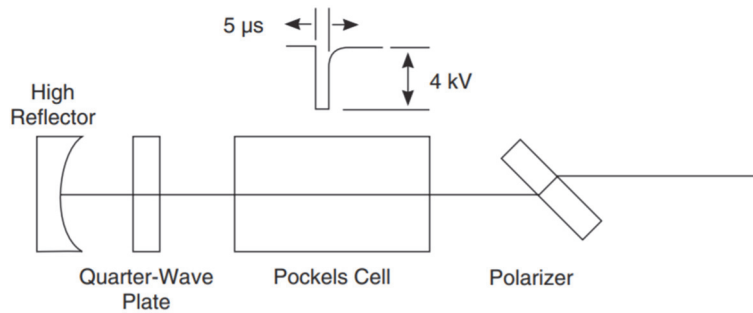


Figure 3.3. Diagram of Q-switch inside of the pump laser used in this procedure [45].

While the laser was vitally important to this procedure, it was only half of the pump generation. In order to study how changing pump wavelength affects the light output from the semiconductor samples, an effective way of adjusting the pump wavelength needed to be implemented. A Spectra-Physics primoScan Optical Parametric Oscillator (OPO) was used to convert the Nd:YAG 355 nm output, which was the third harmonic of the fundamental 1064 nm output, to the needed pump wavelengths of 1800 nm to 1950 nm. The OPO can do this conversion by using a nonlinear beta-Barium Borate (BaB_2O_4) crystal that produces a second-order nonlinear process that yields two different laser outputs. The first output is referred to as the signal, and it is the higher frequency signal of the two outputs. The second output is called the idler output. The

sum of the signal and idler frequencies is equal to the frequency of the pump beam [46]. By changing the angle of the nonlinear crystal, the frequency, and by association, the wavelength of the signal and idler can be precisely controlled. Figure 3.4 shows a general outline of how this process is configured.

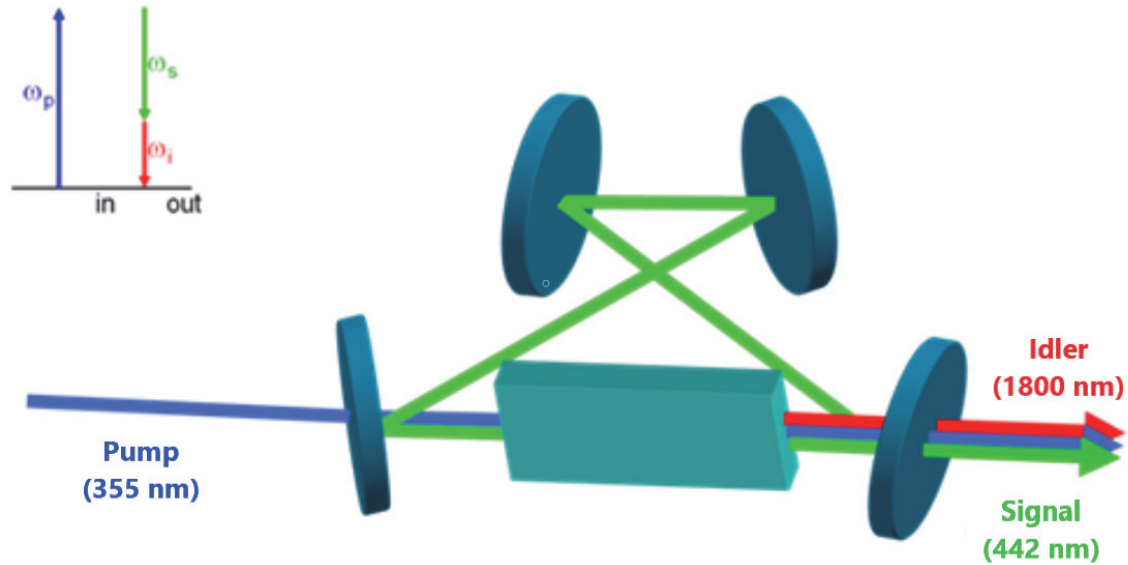


Figure 3.4. A very general model of how an OPO crystal is utilized [46].

The OPO was installed with a graphical user interface for controlling the OPO. However, a LabVIEW program was written to control all functionality of the OPO as well as allow for future automation. LabVIEW is a programming suite produced by National Instruments. Unfortunately, due to complications with moving lab equipment from a computer running Windows 7 to a computer running Windows 10, this LabVIEW program was not used during this thesis procedure. However, it is prepared for future use in the laboratory, and pictures of the program are shown in the appendix to this thesis.

The created program had five primary user operations that it facilitates: establishing a connection to the OPO, writing individual commands, running OPO

programs, automatically creating programs, and manually creating OPO programs. These five processes were each assigned to separate tabs in the program between which the user can easily navigate. To carry out any desired processes, the LabVIEW program must first establish a connection to the OPO. In order to do this, a user must initially use the interface provided by the OPO manufacturer to set the OPO to remote control mode. Once this is accomplished, the user must specify the IP address and port for the device to which they wish to connect. The LabVIEW file auto-fills these inputs with the IP address and port number of the OPO in the laboratory, and it is up to the user if they wish to change these inputs. A virtual toggle switch can then be used to initiate communication with the OPO. The toggle switch turns from red to green and a virtual green LED illuminates on the screen to indicate that a connection has been successfully established with the OPO.

Once the line of communication has been established with the OPO, the most commonly used program functionality is to send manual or individual commands to the device. A text input line is provided to the user so that they can type in any valid command that they wish to send to the OPO. In order for this to work, the user must know the proper syntax for any command they want to use, which can be found in the instruction manual for the OPO. Most commonly, this feature is used to set the OPO to a desired output wavelength. The most commonly used wavelengths have been assigned virtual push buttons so that the user need not type in the full command. Rather they can simply press the button corresponding to the desired wavelength setting. Besides sending instructions to the OPO, this page can be used to query the OPO. One of the most used queries is to request the current wavelength setting. As with every other page, the manual

command tab has a window that displays any response from the OPO once a command or query has been sent.

The OPO has a feature that allows the user to create a “program” for the OPO to follow. These programs consist of a list of wavelengths, steps, and pulses or milliseconds (ms) per step. When specified, the OPO can automatically step through a desired range of wavelength outputs. On the program control panel, the designed LabVIEW program allows a user to load, start, pause, and stop a program as well as check the status of a running program. In order to run a program, a file name for an existing OPO program must be provided and the program must be loaded using a text input field and appropriately labeled push button. Once loaded, the user can start, stop, pause, and check a program’s status.

The LabVIEW control has the capability of automatically creating a new OPO program from a few user inputs. The user must provide a file name, author’s name, short file name (file nickname), starting wavelength, end wavelength, number of steps, and the number of pulses or milliseconds per step. The difference between pulses and milliseconds per step is an important one. If a user specifies that they wish to use pulses per step, then the laser will remain at the current wavelength until the specified number of pump laser pulses occurs. If the user requires the OPO to hold at a wavelength for a increment of time rather than pulses, the OPO will hold for the user specified number of milliseconds and then move to the next wavelength regardless of the number of pump laser pulses that have occurred. In addition to being able to automatically create a program, this tab also provides the user the capability of checking to make sure that the program was written properly. This is done through the use of two helpful pushbuttons.

The first button loads the previously created file and lists every wavelength as well as the number or time duration for each different wavelength. The second button provides the number of “items” in a program. An item is one wavelength in the program. For example, if a user created a program that started at 1800 nm and ended at 1900 nm in five steps, then the second button should return a value of five if the OPO instructions were created properly.

Finally, if a user wishes to have more control over the creation of an OPO program, they can use the manual program creation tab. On this tab, new programs can be written and existing programs can be edited. This page has all of the same functionality as the automatic program creation page. However, the user must individually add each desired wavelength along with the corresponding pulse or time hold. The user can also individually enable, disable, and delete items in an existing program. This page is useful for OPO programs that do not have uniform wavelength steps or do not have the same hold duration at each wavelength. To illustrate this, if a user used the automatic program creation function to write a program that started at 1800 nm and ended at 1900 nm with 5 steps and a 10 pulse pause at each step, the LabVIEW file would create an OPO program that stopped at 1800 nm, 1825 nm, 1850 nm, 1875 nm, and 1900 nm with a 10 pulse pause at each wavelength. However, if a user wanted to specifically look at 1800 nm, 1820 nm, 1830 nm, 1860 nm, and 1900 nm with a different hold time at each step, there is no way to automatically create this file. The user would have to individually create each item using the manual creation page.

Beam Path

Once the pump beam excited the OPO, it had approximately 4.5 m to travel before coming in contact with the sample. Due to the diverging nature of the laser beam, carefully selected mirrors and lenses were used to minimize divergence and direct the beam to the sample. Figure 3.5 shows the entire beam path with all mirrors and lenses that were used to guide the beam, and Table 3.1 shows the corresponding optics descriptions. Immediately after leaving the OPO, two mirrors (2,3) were used to adjust the height of the pump beam as well as level it. Two different pairs of plano-convex to plano-convex (4,5) and plano-convex to plano-concave (11,12) lenses, which were referred to as telescopes, were used to collimate the beam at different points along the beam path. The first telescope (4,5) was used directly after the first height adjustment. In the telescope configuration, the plano-concave lens (4) was used to expand the beam, because the rate that a laser beam diverges is inversely proportional to the diameter of the beam. Expanding the beam limited its divergence while traveling to the sample. The plano-convex lens (5) was used in an attempt to collimate the beam at the desired beam diameter of approximately one inch. A second set of mirrors (8,9) was used to further adjust the height of the laser beam after crossing to a second optical table. This second adjustment ensured that the beam was at the proper height to come in contact with the ICL sample and was level. A second telescope (11,12) was used to narrow the pump beam down to the desired diameter as to maximize the amount of beam coming in contact with the semiconductor sample.

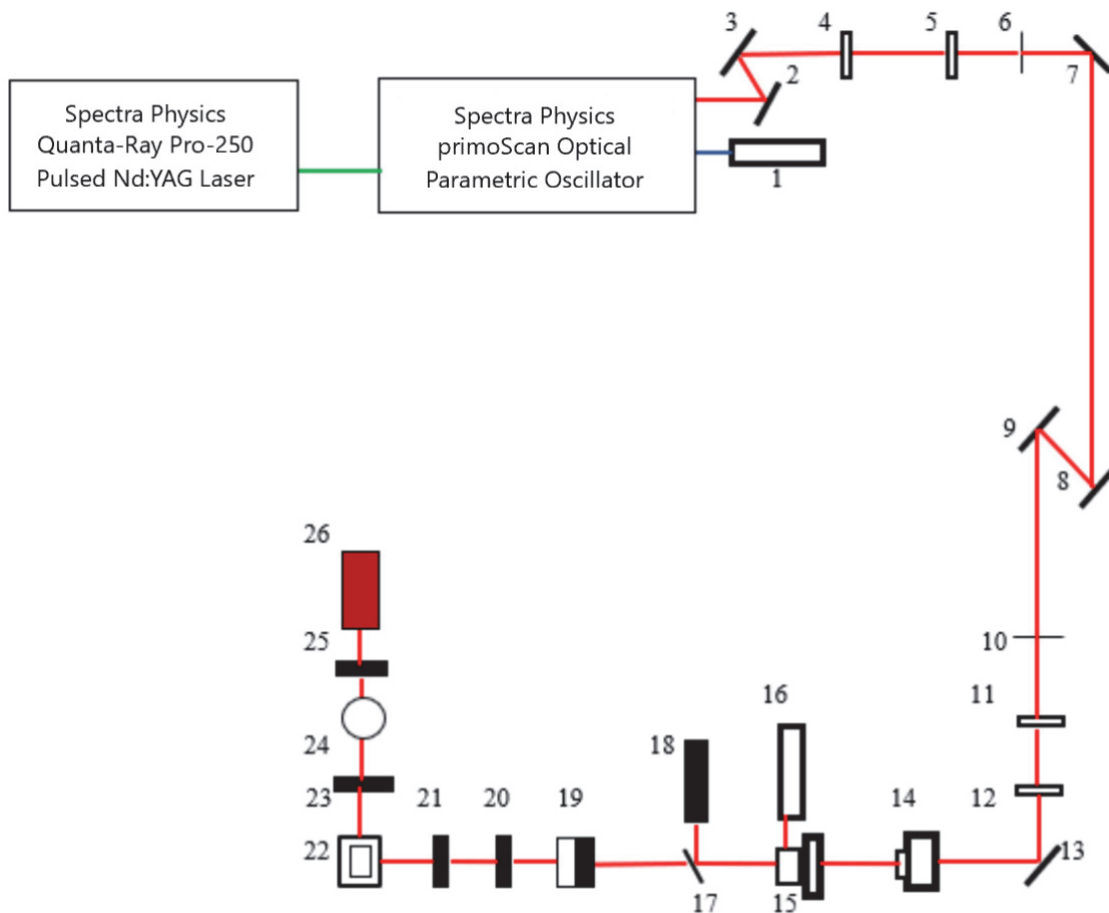


Figure 3.5. Basic schematic of the beam path for this procedure with all lenses, windows, and other optical equipment. See Table 3.1 for the key to each listed number.

Table 3.1. Descriptions of the optics and equipment listed in Figure 3.5.

Designation	Description
1	Beam dump.
2	Metallic mirror w/ protected Al coating, R > 90% (450 nm – 2 μ m), 25.4 mm Dia.
3	Metallic mirror w/ protected Al coating, R > 90% (450 nm – 2 μ m), 25.4 mm Dia.
4	LC2679 plano-convex lens, f = -30.0 mm, 25.4 mm Dia.
5	LA1256 plano-convex lens, f = 300.00 mm, 50.8 mm Dia.
6	Mounted iris diaphragm – variable aperture 1-25 mm Dia.
7	Metallic mirror w/ protected Al coating, R > 96.0%, 76.2 mm Dia.
8	Metallic mirror w/ protected Al coating, R > 96.0%, 50.8 mm Dia.
9	Metallic mirror w/ protected Al coating, R > 96.0%, 50.8 mm Dia.
10	Mounted iris diaphragm – variable aperture 1-25 mm Dia.
11	N-BK7 plano-convex lens, f = 200.0 mm, 50.8 mm Dia.
12	SF11 bi-concave lens, f = -50.0 mm, 25.4 mm Dia.
13	Metallic mirror w/ protected Al coating, R > 98.5%, 25.4 mm Dia.
14	Custom made achromatic half-wave retarder, 22 mm Dia.
15	Polarizing cube beamsplitter in manual rotation stage.
16	Beam dump.
17	Custom made 45 degree incidence broadband beamsplitter.
18	Pyroelectric energy probe.
19	Removable neutral density filters.
20	BK7 plano-convex cylindrical lens, f = 200.0 mm, 50.8 mm Square.
21	BK7 plano-convex cylindrical lens, f = 150.0 mm, 50.8 mm square.
22	Semiconductor laser sample.
23	CaF ₂ bi-convex lens, f = 70.0 mm, 50.8 mm Dia.
24	Metallic neutral density filters, OD = 0.3, 1.0, 1.45, and 2.0 for 2.0 μ m < λ < 5.0 μ m.
25	CaF ₂ bi-convex lens, f = 50.0 mm, 50.8 mm Dia.
26	Indium Antimonide photovoltaic detector.

Once the pump beam had traveled most of the distance to the sample, a rotatable achromatic half-wave retarder (14) combined with a broadband polarizing cube beam splitter (15) were used to control the intensity of the pump beam. The half-wave retarder controlled the polarization of the pump beam, and the polarizing cube beam splitter only allowed horizontally polarized light to pass through. By using the half-wave retarder to adjust the pump beam polarization, the intensity of light reaching the sample could be controlled. Any vertically polarized component of the pump beam was reflected into a

beam dump (16) by the beam splitter (15). After the cube beam splitter, the pump beam came into contact with a broadband beam splitter (17) that again reduced the pump intensity by transmitting some light and reflecting the rest into a pyroelectric energy probe (18) being monitored by a Laser Probe dual channel energy meter. The ratio of energy passing through the beam splitter to energy reflected by the beam splitter could be determined by placing a second pyroelectric energy probe in the beam path after the beam splitter.

Neutral density filters (19) were used to further adjust the pump beam intensity before it came in contact with the sample. These filters could be chosen by experimenter to maximize the sample beam output while not damaging the samples. Finally, two cylindrical lenses (20,21) were used to focus the pump beam onto the sample (22) as an approximately 2 mm long and 1 mm wide stripe.

For the procedure discussed in this thesis, two samples were mounted inside of a Advanced Research Systems optical cryostat. The cryostat had windows made of calcium fluoride, which allowed for a vacuum to be held within the cryostat while also not significantly attenuating the pump or sample beams. An Alcatel mechanical vacuum pump was used to produce a vacuum of ≤ 5 mTorr within the cryostat. Then an oil-free liquid-nitrogen-cooled sorption pump was used to further evacuate the cryostat to less than 1 mTorr. Keeping a vacuum within the cryostat was crucial as it prevented unwanted molecules from condensing on the samples' surfaces and reducing device functionality.

As shown in Figure 3.6, the ICL samples were mounted to a oxygen free high thermal conductivity (OFHC) copper heat sink. A Si resistance temperature detector mounted very close to the samples on the back side of the copper block was used to

monitor the sample temperature within the cryostat. A Lakeshore Model 330 temperature controller was used to monitor and control the sample temperature. A heater was employed because the cryostat was cooled by liquid nitrogen being constantly flowed from a storage tank, through a transfer line, and into the cryostat. This combination of liquid nitrogen flow and heating allowed for the sample temperature to be controlled anywhere within the desired range of 80 K to 300 K. The cryostat was mounted to a three-axis translation stage, which provided complete control of the position and alignment of the samples. A picture of the cryostat, translation stage, dewar, and storage tank is shown in Figure 3.7, and a close up picture of the cryostat mounted on the translation stage is show in Figure 3.8.



Figure 3.6. Both samples mounted on the copper block with silver paint. The top sample did not have graphene, while the bottom sample had a graphene top contact.

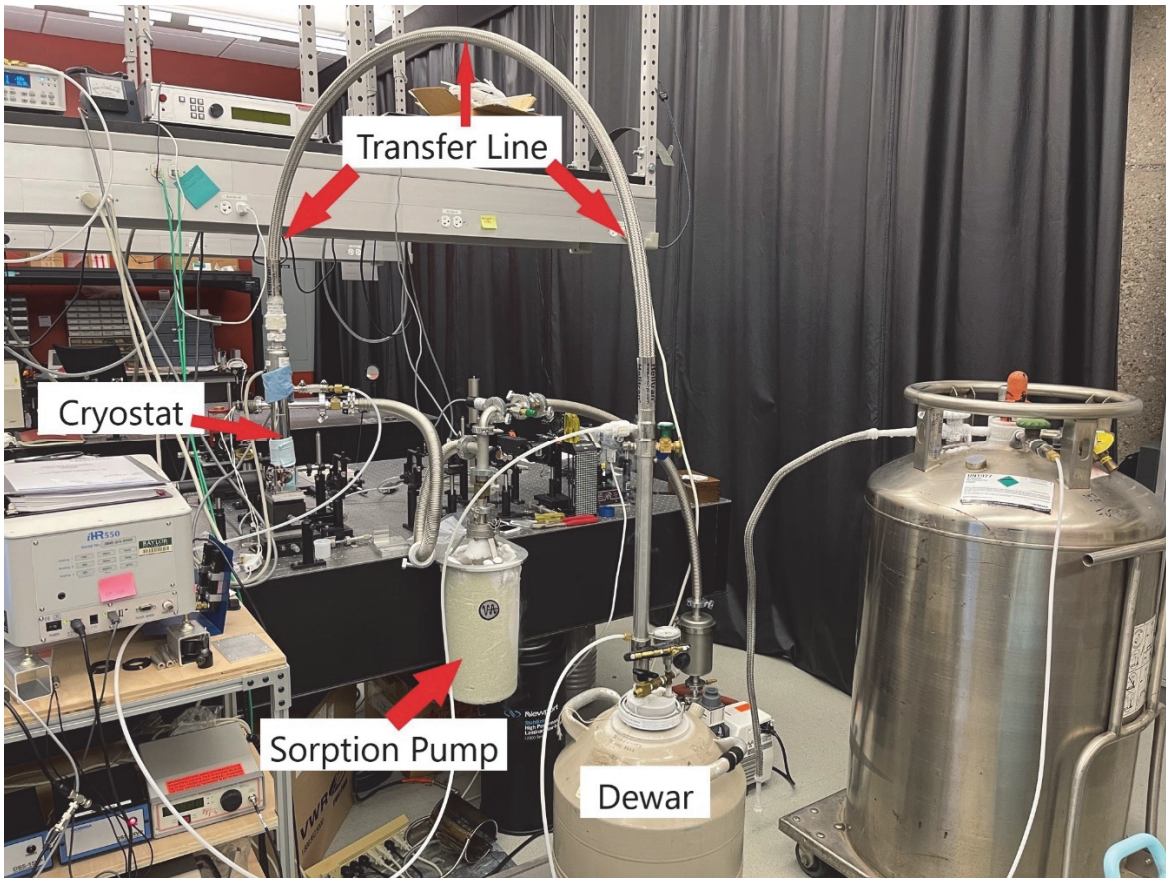


Figure 3.7. Picture of nitrogen dewar, transfer line, sorption vacuum pump, and cryostat setup.

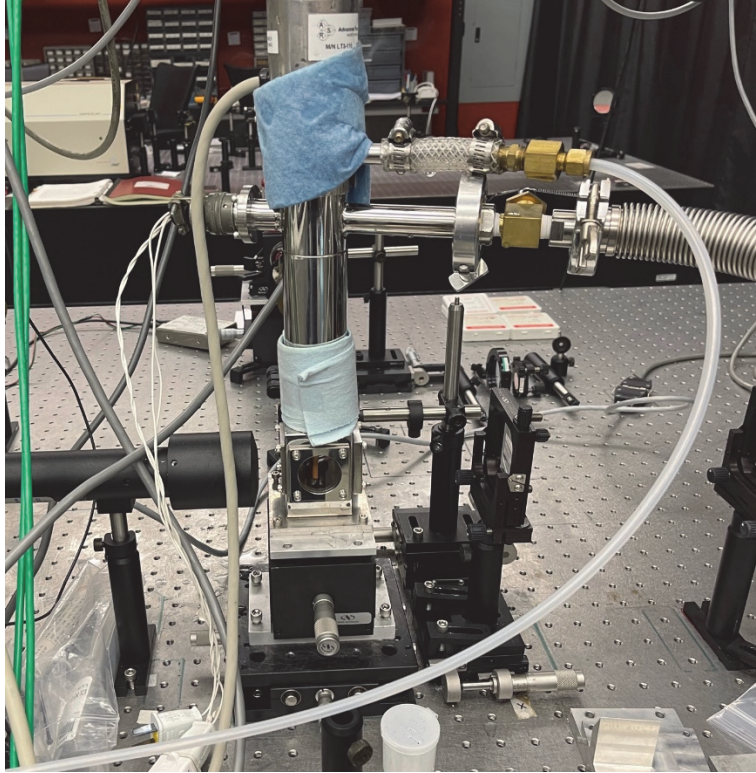


Figure 3.8. Close up picture of the optical cryostat used in this procedure.

The beam output from the samples had a much shorter distance to travel than the pump beam. Regardless, a bi-convex lens (22) immediately outside the calcium fluoride cryostat window was used to collimate the beam and prevent divergence. Another neutral density filter (24) was the next optic in the output beam path. This interchangeable filter prevents the sample output beam from saturating the detector. Another bi-convex lens (25) was used to focus the collimated beam onto a Judson Technologies photovoltaic indium antimonide detector (26). Figure 3.9 shows a schematic of the path from sample beam output to the Judson detector.

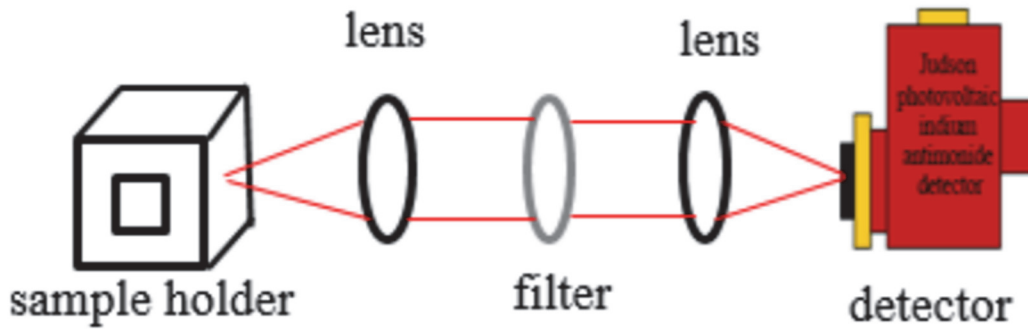


Figure 3.9. The beam path from the cryostat to the Judson detector [43].

When the sample beam needed to be directed into a spectrometer, the beam path was changed using two gold mirrors. As seen in Figure 3.10, the mirrors caused the beam to make two 90 degree turns so that it could travel through the front entrance slit of the spectrometer. The gold mirrors also changed the height of and leveled the laser beam. As with the previous arrangements, two bi-convex lenses were used to collimate and focus the beam after leaving the cryostat and before entering the spectrometer, respectively.

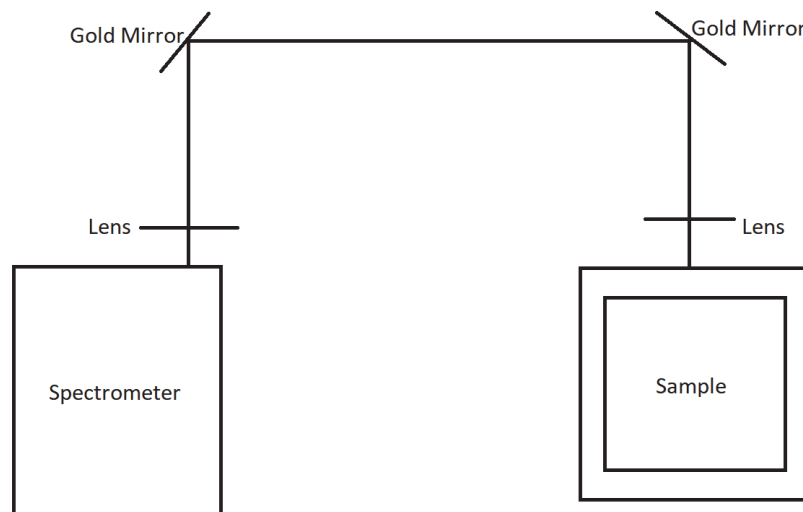


Figure 3.10. Top-down diagram of beam path from cryostat to spectrometer.

Spectrometer

A Horiba iHR550 Mid-Focal Length Imaging spectrometer was used to measure the emitted spectra from the samples. The entire spectrometer system is made up of several different components that all work in conjunction to allow for spectral data collection. These different devices are the spectrometer itself, a PC running LabSpec6 Software, a Stanford Research Systems (SRS) Model SR810 DSP Lock-in Amplifier, a DSS-15VP Low Noise Power Amplifier, and a DSS-IS020L Indium Antimonide Solid State Detector.

Figure 3.11 shows the layout of the spectrometer, which is configured with one entrance slit and two exit slits. The entrance and exit slits have adjustable widths that range from completely closed to 7 mm when fully open. This feature allows the user to limit the amount of light that is entering the spectrometer, especially if the laser beam is diverging and is excessively wide or intense. Once light passes through the entrance slit, a mirror mounted on the back wall of the spectrometer collimates the light and reflects it towards the diffraction grating turret. The turret is a rotating stage that has three different gratings mounted on it. For this thesis, a grating with 300 grooves per nm that was blazed at 4000 nm was used. The light being reflected from the turret is directed onto a focusing mirror. The mirror directs the focused light towards the front exit of the spectrometer. The light being measured either travels out the front exit and into a short-wavelength lead selenide detector, or is diverted by a final mirror to direct the laser beam out through the side exit and into a liquid-nitrogen-cooled Indium Antimonide detector.

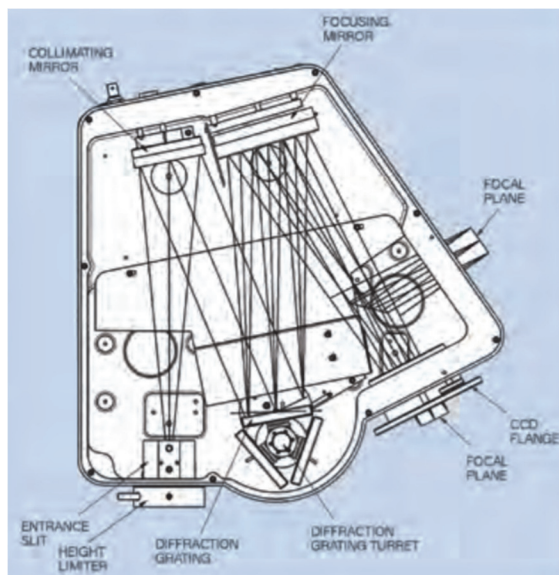


Figure 3.11. Diagram of the Horiba iHR 550 Spectrometer that was used to collect spectral data for this thesis [47].

In order to control the functionality of the iHR 550, a laptop computer running Horiba Scientific's LabSpec6 software was used. Once all the various components of the spectrometer system had been powered on and set up, the PC was used to acquire spectra. Through the LabSpec6 software, all of the moving components in the spectrometer were controlled. These included entrance and exit slit widths, diffraction grating settings, and putting the exit slit mirror in and out of place. After inputting the expected wavelength of the measured light, the software turned the grating into the proper position to reflect the light into the focusing mirror.

The LabSpec6 software enabled the initial data visualization. The software allowed the user to select multiple options for axis labels, data scales, wavelength scanning ranges, plot colors, and other features. All data could be saved in multiple file formats including LabSpec6 and text. This expedited exporting data for analysis to other software tools such as Origin and Excel for analysis.

Mounted to the exit slit of the spectrometer was a DSS-IS020L Indium Antimonide Solid State Detector. This detector was powered by a DSS-15VP Low Noise Power Amplifier. Figure 3.12 shows the relative spectral response for the detector. From the figure it can clearly be seen that this liquid-nitrogen-cooled sensor is specifically designed for detecting mid-IR light sources. For the samples tested in this presentation, the emitted light was between 3 and 4 μm , which falls directly in the accessible range for the IS020L. The detector was connected via BNC cable to a Stanford Research Systems (SRS) Lock-in Model 810 for data collection.

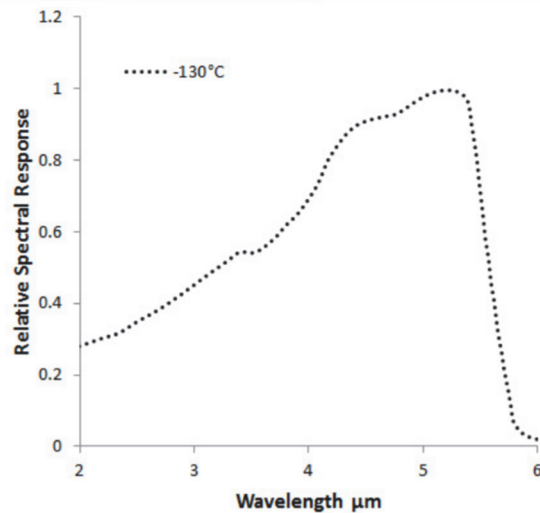


Figure 3.12. Relative spectral response for the DSS-IS020L detector [48].

The SRS lock-in was vitally important to being able to detect any signal. A lock-in is used to detect very small AC signals that are often mixed with noise that is much greater than the signal itself. A lock-in uses phase sensitive detection to find the desired signal. Phase sensitive detection requires a user to provide a reference data signal so that the lock-in can determine the frequency of the incoming data signal. The lock-in uses

digital signal processing to parse the data signal out of any noise [49]. For the data collected in this thesis, the data signal was provided to the lock-in through the BNC connection to the mid-IR detector mounted to the spectrometer, and the reference input was from the reference (trigger) output of the laser Q-switch. For ease of use, the lock-in had several seven segment displays so that the user can see the up-to-date frequency, phase, and amplitude of the signal. This amplitude and other pertinent data was sent to the PC running LabSpec6 for plotting.

Data Collection

For light-light data acquisition, the collected Judson signal was passed through a preamplifier with two different gain stages. For this procedure, the high gain (second) stage was used to better visualize the data. The output from the preamplifier was routed to a Stanford Research Systems Model SR250 gated integrator and boxcar averager. The boxcar produced a gated output signal, which was the maximum value of the signal passed from the detector. This output was sent to an oscilloscope for visualization. The oscilloscope visualization also allowed the user to adjust the position of the boxcar gate relative to the data signal so as to maximize the averager reading. The boxcar averager was triggered using the Q-switch output of the pump laser, and the busy output of the boxcar was used to trigger the oscilloscope.

LabVIEW programs were used to control and communicate with the boxcar, energy meter, half-wave plate, and temperature controller. A program written in LabVIEW (called the light-light program) was also used to collect all data coming from the boxcar averager and produce light-light curves, which are plots of output power vs

input (pump) intensity. This data will be further discussed in the results section of this report.

Calibrations

In order to most accurately produce light-light curves, the amount of energy provided by the pump beam that is incident on the sample must be known. This was accomplished by determining the shape of the pump beam both perpendicular and parallel to the sample cavity. This was done by measuring the perpendicular (ω_{\perp}) and parallel (ω_{\parallel}) intensity profiles of the pump beam. Figure 3.13 illustrates the knife edge method was employed to measure the intensity profiles.

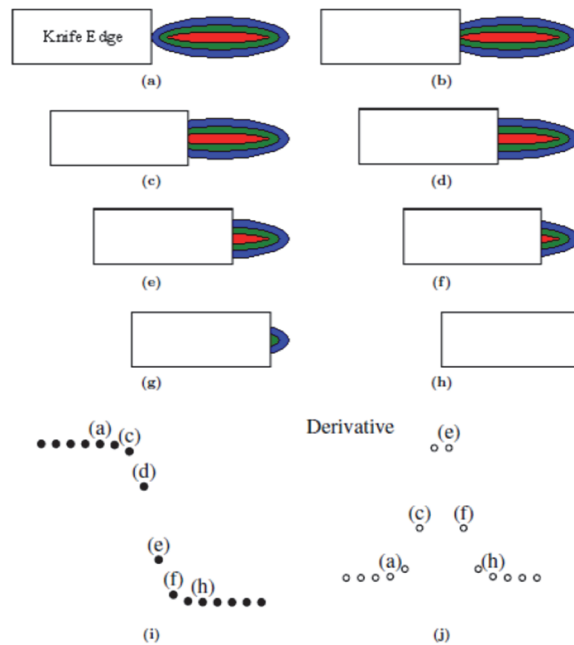


Figure 3.13 Illustration of the knife edge method of beam profile collection. (a) through (h) diagrams how the knife edge is used to progressively block more and more of the pump beam. (i) shows the corresponding intensity data points for (a) through (h). (j) shows the derivative of (i), which is the actual beam profile [50].

The knife edge method uses a sharp edge placed at the sample position to systematically block more and more of the beam. A second pyroelectric energy probe was placed behind the blade, so that any amount of the beam not being blocked would shine into the probe. The energy of the unblocked beam was measured as a function of the blade position. Taking a derivative of this data with respect to the sharp blade's position produces a beam intensity profile along the desired direction. A Gaussian curve was then fitted to the beam profile so that the full width half maximum (FWHM) of the data could be determined. This FWHM in each direction provided a measure of the width of the beam at the sample position. Table 3.2 shows the FWHM data in both the vertical and horizontal directions of the pump beam.

Table 3.2 FWHM data for the horizontal and vertical directions of the pump beam.

Direction	Pump Wavelength (nm)	FWHM (mm)
Horizontal	1800	1.972
	1825	1.888
	1850	1.862
	1875	2.105
	1900	2.112
	1925	2.460
	1950	2.579
Vertical	1800	0.945
	1825	0.861
	1850	0.809
	1875	0.843
	1900	0.860
	1925	0.802
	1950	0.715

Detector Collection Efficiency

The detector collection efficiency (DCE) is crucial to producing proper light-light curves, because the sample beam output had a larger diameter than that of the detector element. Thus, knowing the fraction of the sample beam actually being intercepted by the detector allowed an accurate calculation of the total beam energy. The DCE was found in a very similar fashion to the pump beam profiles. Because the detector could be translated horizontally and vertically, there was no need for a blade to block the signal. The detector was moved through the sample beam to determine cross sections of the sample beam intensity profiles. Combined with the sample beam profiles, this data was used to determine the total pump intensity and the sample output power.

Pulse Duration Response

Due to the use of a brand new OPO for this collection of data, the pulse duration response (PDR) of the new device needed to be determined. This correction was necessary because the time constant of the Judson detector was $2.5 \mu\text{s}$. However, the OPO idler pulsed at approximately 10 ns, which was not enough time to trigger a full response from the detector. This can be seen in Figure 3.14, which shows that in order to produce a full response, the idler pulse would need to be much longer. The full width half maximum of the time duration of the idler pulses from the OPO were input to a previously written LabVIEW program that calculated the PDR [50]. The PDR values affected the output power values calculated in the light-light program. Figure 3.15 shows a plot of the OPO idler pulse widths for each pump wavelength used in this procedure. Each pulse width is between 6 and 12 ns, which is far less than the time constant of the

Judson detector (2.5 μ s) Correction was done in the light-light program to account for the actual detector response.

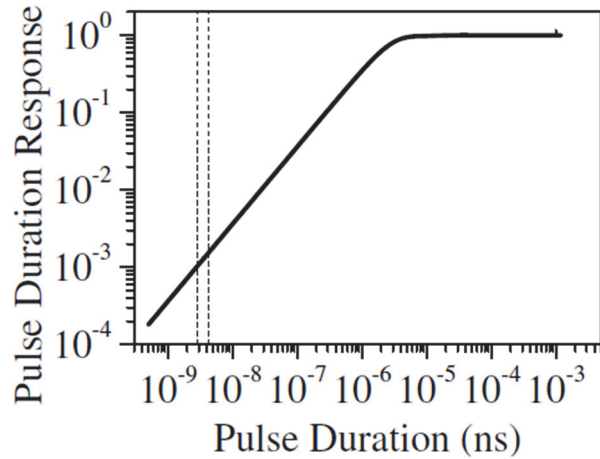


Figure 3.14. Plot of pulse duration response verses pulse duration to show the necessary pulse duration to achieve a full detector response [50]

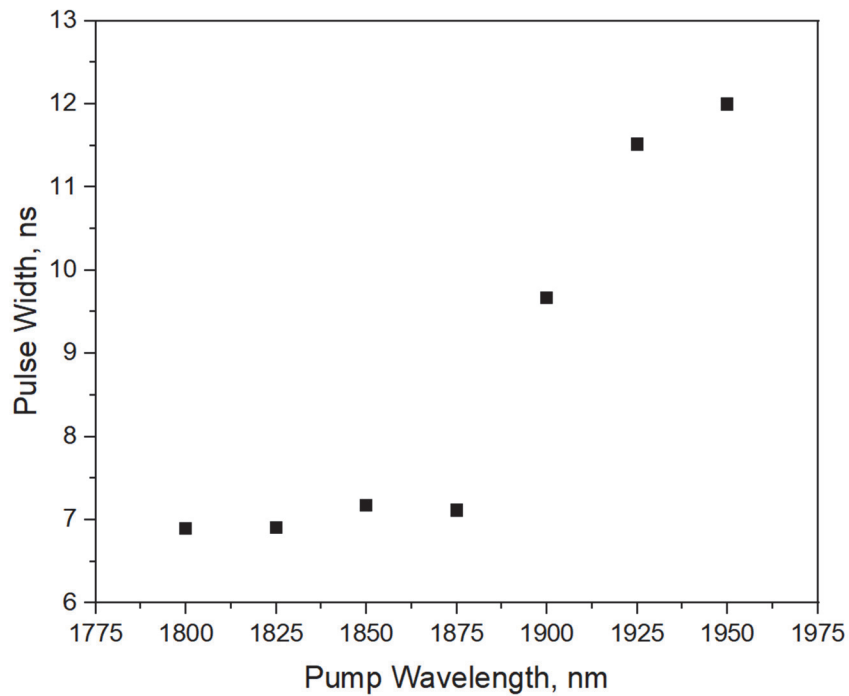


Figure 3.15. Plot of pulse widths for the OPO idler at each of the pertinent pump wavelengths.

Data Processing

The two key data sets needed to produce a light-light curve are the peak pump intensity and the peak output power. The light-light LabVIEW program produced Microsoft Excel files that contained all of the data necessary to calculate these values as well as the values themselves. The peak pump intensity is found from:

$$I_i = \frac{\bar{E}_i R_{BS} T_p \kappa}{L_c \omega_{\perp} \tau_p} \quad (3.1)$$

\bar{E}_i is the average total energy per pulse of the pump beam over 30 consecutive pulses.

R_{BS} is the broadband beam splitter's transmission to reflection ratio, which was set to 1 for this experiment. T_p , which is dependent on pump wavelength, is the value of all transmission for every optic between the broadband beam splitter and the sample multiplied together. κ is the fraction of the energy incident on ICL sample. $L_c \omega_{\perp} \tau_p$ is the product of the cavity length, perpendicular pump beam FWHM, and the pump pulse duration, respectively.

The peak output power, P_i is:

$$P_i = \frac{\bar{V}_i - \bar{V}_{min}}{T_C \xi_C \xi_d T_{peak} T_{\lambda}(\lambda) T_{\tau}(\tau)} \quad (3.2)$$

The numerator is the difference between the average peak detector voltage, \bar{V}_i , and the minimum measured average peak detector voltage, \bar{V}_{min} . The denominator is the product of the product of all transmission values for the optics between the sample and the detector, T_C , the lens collection efficiency, ξ_C , the detector collection efficiency, ξ_d , and the Judson detector transfer function, $T_{peak} T_{\lambda}(\lambda) T_{\tau}(\tau)$. T_{peak} is the peak responsivity of the detector, $T_{\lambda}(\lambda)$ is the spectral response, and $T_{\tau}(\tau)$ is the pulse duration response. The Judson detector transfer function was provided by the manufacturer of the detector.

ICL Samples

The ICL samples that were studied in this procedure were grown at the Naval Research Laboratory (NRL) in Washington, DC. Molecular beam epitaxy was used to grow the samples on *n*-GaSb substrates. The active “W” wells were grown using InAs and GaInSb, the electron injectors were made with InAs and AlSb, and the hole injectors were composed of GaSb and AlSb (similar to the schematic in Figure 2.11). In each of the injectors, four of the InAs wells are *n*-doped at $4 \times 10^{17} \text{cm}^{-3}$. Transition regions of *n*-doped InAs and AlSb (400-600 nm layer of $\sim 10^{16} \text{cm}^{-3}$ doping) surrounded the active region, and these transition regions are additionally surrounded by *n*-doped GaSb (50 nm layers of $\sim 10^{17} \text{cm}^{-3}$ doping). The transition layers help to ensure that the doping levels throughout the sample are high near the contacts and low near the active regions. Table 3.3 shows the layer thickness for the ICL “W” regions, which were identical for both samples. The NRL designation for this ICL wafer was T080122

Table 3.3. “W” active region layer thicknesses in angstroms (Å).

Layers	Thickness (Å)
AlSb	10
InAs	16
GaInSb	25
InAs	20
AlSb	25

Table 3.4 lists the samples used for this report as well as their respective emission wavelength. Figure 3.16 shows a diagram of the general structure of an optically pumped ICL sample as used in this procedure. The pump stripes had a cavity length of 2 mm and

a strip width of approximately 1 mm in the 1800 to 1950 nm pump wavelength range. The active region of the two samples used for this procedure were layered with 10 periods each. As previously discussed in Chapter 2, a period in an ICL is an optical transition region, electron injector, and hole injector. The thickness of the InAs layers in the “W” wells within the ICLs primarily controls the emission wavelength.

Table 3.4. Semiconductor ICL Samples Used in This Thesis

Sample	Denoted As	Cavity Length (mm)
T080122	A	3
T080122 (graphene monolayer)	B	2

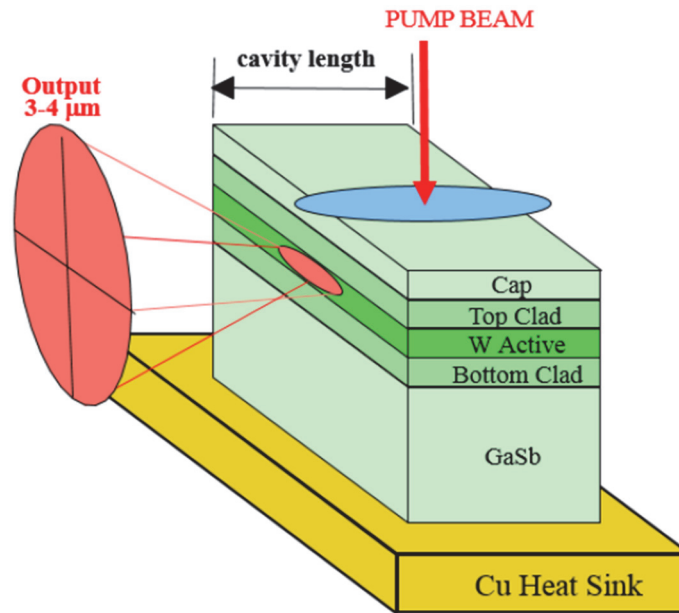


Figure. 3.16 Structure of optically pumped ICL [43].

Professor James Tour’s research group at Rice University applied the graphene to a section of the T080122 wafer. The graphene was grown on a copper substrate using

chemical vapor deposition before being transferred to the ICL sample. The sample was cleaved to a length of 2 mm before being mounted to the copper heat sink.

CHAPTER FOUR

Results

Optical pumping results are presented in this chapter for both light output as a function of pump intensity and wavelength, all as a function of optical pump wavelength and sample temperature.

Light-Light

Two different samples of T080122 were optically pumped for this procedure, with one sample having a graphene monolayer applied to it (sample B). While the samples were designed epitaxially for electrical stimulation, optically pumping has been proven to be a successful method of inducing lasing activity [51]. A measure of device performance is power versus pump intensity, which for optical pumping may be called a light-light curve. Figure 4.1 shows a light-light curve, which is a plot of peak output power on the y-axis and pump intensity on the x-axis, for sample B with a pump wavelength of 1800 nm at 180 K.

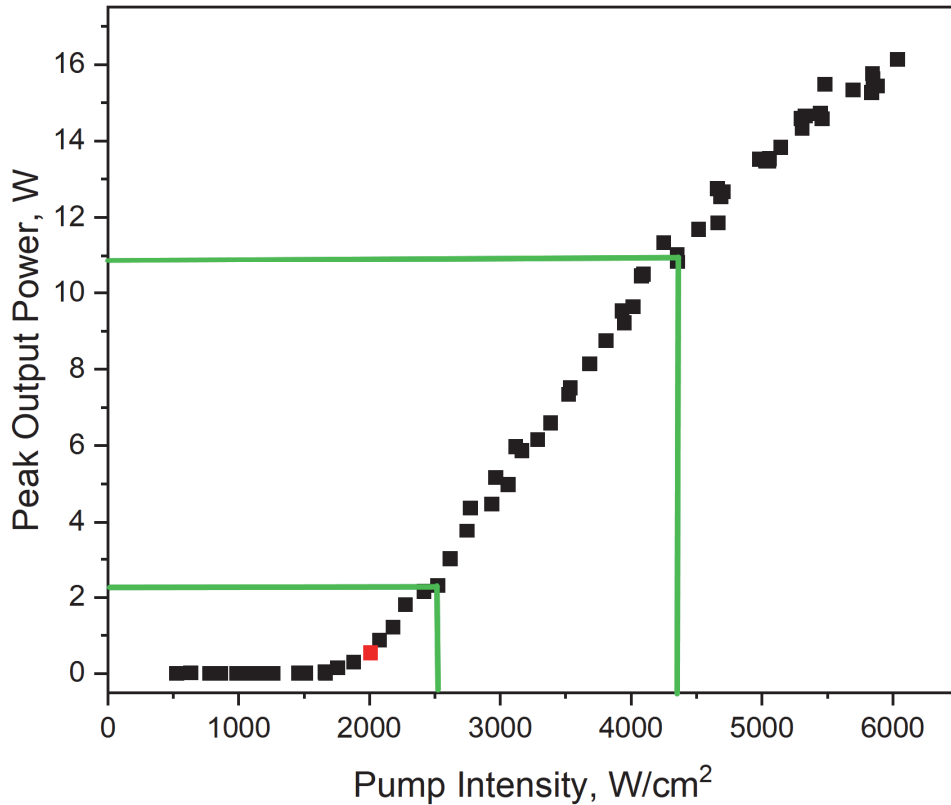


Figure 4.1. Plot of peak output power versus pump intensity for sample B at 1800 nm pump wavelength and 180 K.

In addition to overall output power achieved, there are two important characteristics to derive from the light-light curve. The first is the threshold pump intensity, which is the minimum pump intensity that produces lasing. The threshold pump intensity is indicated with the red data point, and it was found by identifying the first data point where the curve begins to show a linear trend and finding the corresponding pump intensity at that point. For the light-light curve in Figure 4.1, the threshold pump intensity is at approximately 2000 W/cm². The second important characteristic is the slope efficiency, which indicates how the peak output power is changing with pump intensity. The slope efficiency is simply calculated by taking the change in peak power (rise) and dividing by the change in pump intensity over the same range (run) over a range of linear

data points. For the plot in Figure. 4.1, the slope efficiency was approximately 23.43%. The green lines on the plot indicate the maximum and minimum output power and pump intensity data points that were used to calculate the slope efficiency. The non-linear portion of the curve at high powers is due to over saturation due to the pump intensity being too high, resulting in heating and loss.

A general expectation for the ICL samples used in this thesis is that the threshold intensity will increase and the slope efficiency will decrease as temperature increases. This phenomenon was observed in the collected data. One such example of this is the plot shown in Figure 4.2. which is a view of a fan of light-light curves for sample A at 1950 nm pump wavelength over a range of temperatures. Each curve on the plot represents a different temperature. While some exceptions can be seen in the plot, generally speaking the lower temperature curves have lower thresholds and greater slope efficiencies than the curves at higher temperatures.

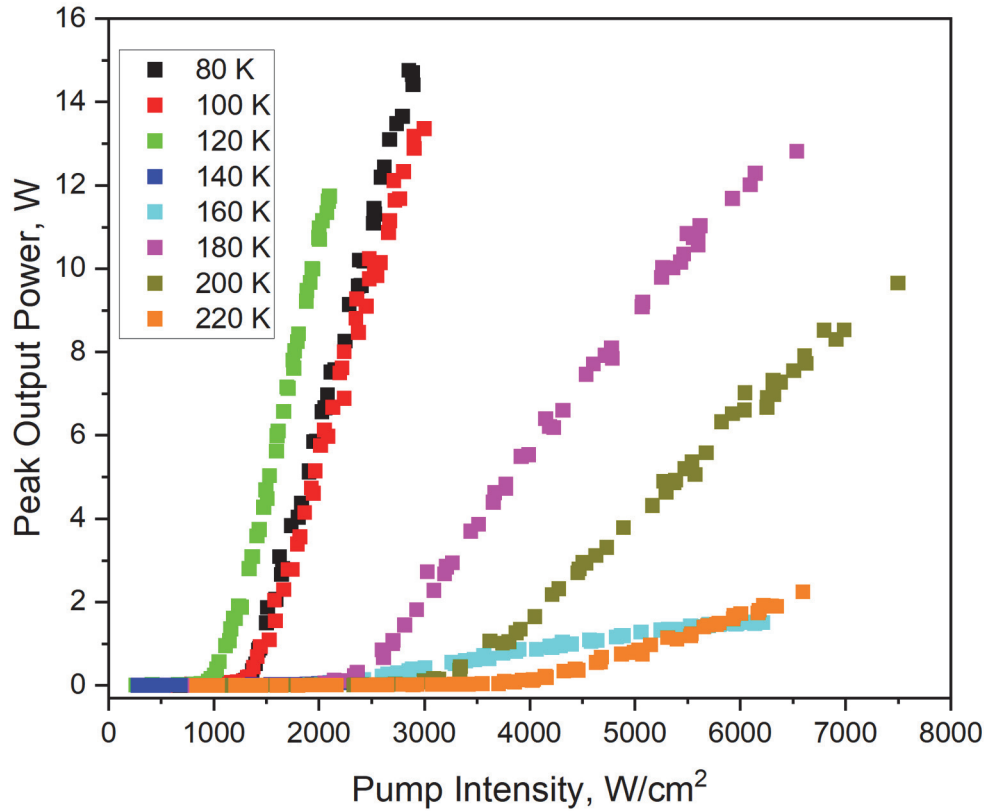


Figure 4.2. Fan of light-light curves over a range of temperatures for sample A being pumped at 1950 nm.

To compare with the plot shown in Figure 4.2, Figure 4.3 shows the same fan but for sample B. Again, the pump wavelength was at 1950 nm and the data is shown over the same range of temperatures from 80 K to 220 K. With a couple of exceptions (e.g. 140 K and 160 K), the same expected trend appears of increasing threshold intensities and decreasing slope efficiencies with increasing temperature.

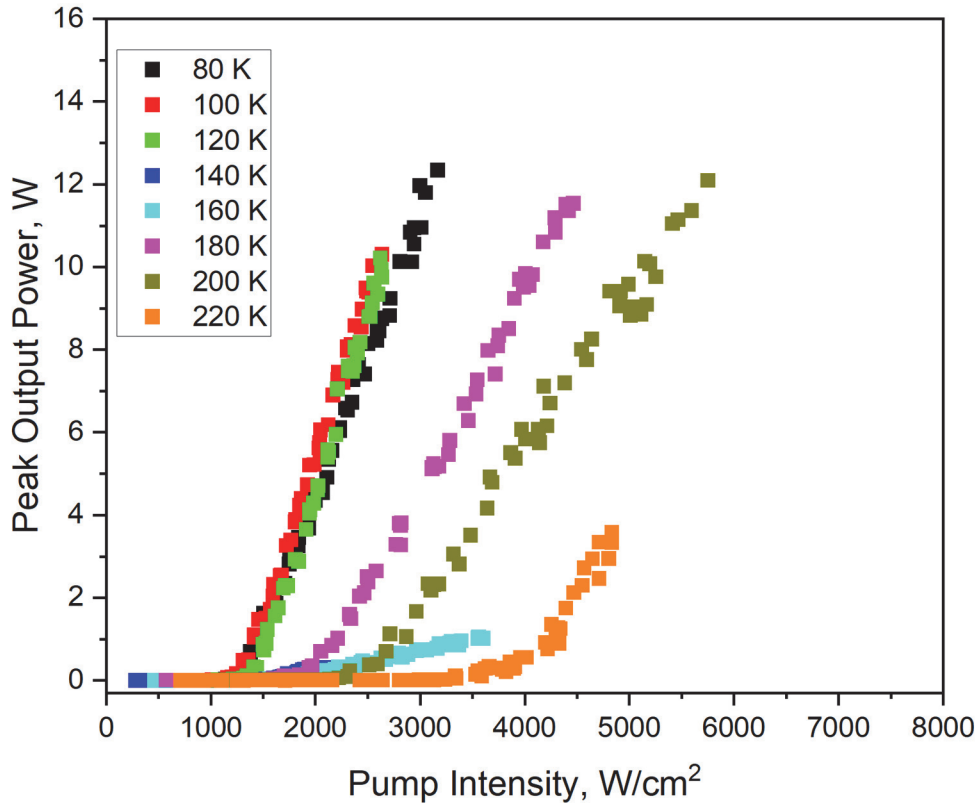


Figure 4.3. Plot of light-light curves over a range of temperatures for sample B with a pump wavelength of 1950 nm.

Because the key difference between the two samples was the use of graphene on sample B, it was important to determine any variations between results from the two sample types. Figures 4.4 shows the threshold pump intensity versus temperature for both samples under the same conditions as in Figures 4.2 and 4.3. First, with increasing temperature there is a general trend of increasing threshold intensity. From previous work [52], the expected trend is to see an exponential increase in threshold pump intensity with increasing temperature. The data was plotted with a logarithmic y-axis, which is the common practice for this sort of data, and an exponential fit was applied to the curves for each sample. The characteristic temperatures derived from the fits were 61.3 K and 43.2 K for Sample A and Sample B, respectively. Sample A did exhibit an exponential

increase, as expected. While sample B did show an increase in threshold intensity with increasing temperature, the R-square value indicated a less reliable fit than for Sample A. Sample B had a higher threshold intensity than sample A at all but one temperature value. The extent to which the graphene on sample B may be the source of these differences will be the subject of further investigation.

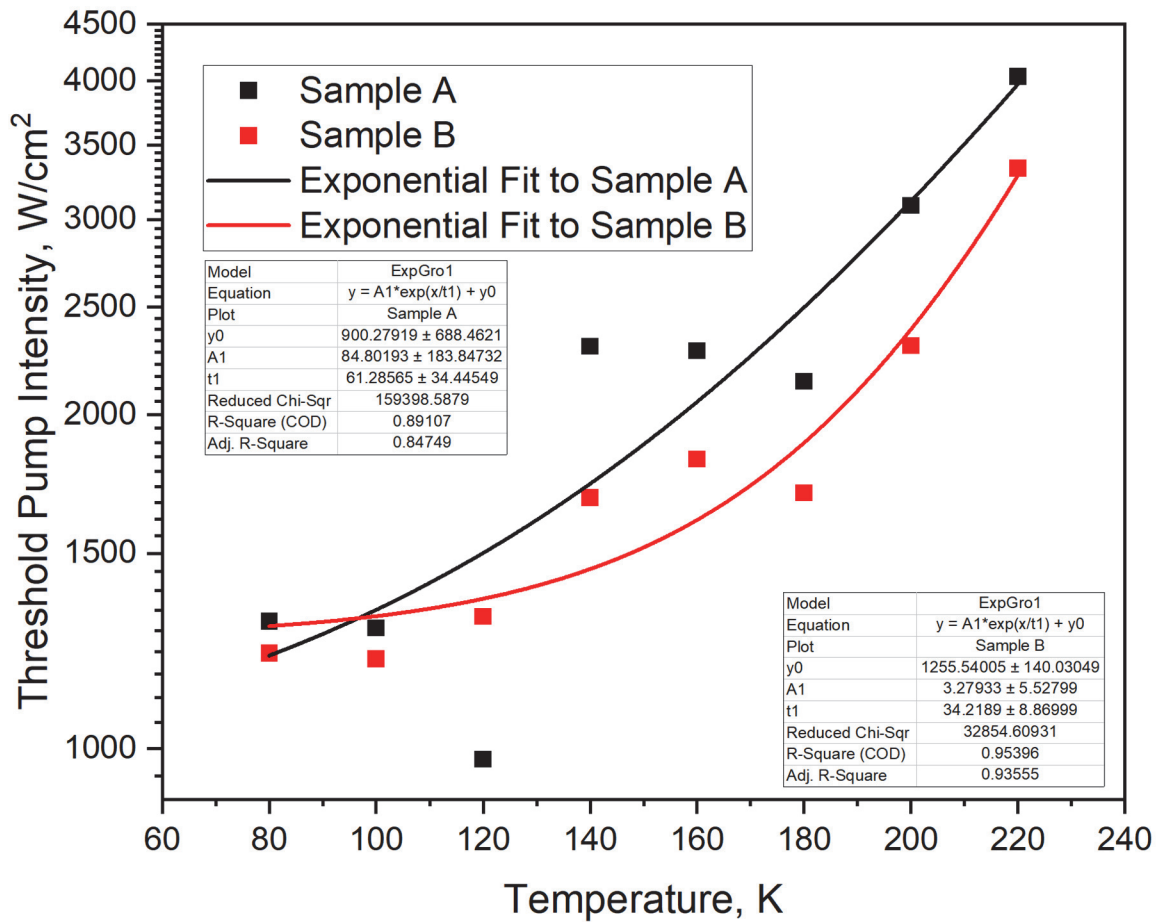


Figure 4.4. Threshold pump intensity versus temperature for samples A and B at 1950 nm pump wavelength. Exponential fits were applied to both curves and the relevant fit data is shown in the included tables.

Figure 4.5 shows a plot of slope efficiency versus temperature for samples A and B. As with the previous figure, this data is over a temperature range from 80 K to 220 K

and at a pump wavelength of 1950 nm. There is an overall trend of decreasing slope efficiency with increasing temperature, which is the expected phenomenon consistent with electrically injected and optically pumped laser devices. Sample B was noted to have higher slope efficiency than sample A at low temperatures, with the opposite being true at high temperatures. By comparing the data at 140 K and 160 K to the surrounding data, the data at those temperatures are strongly suspected to be unreliable, and future work will be done to confirm this assumption and to rectify this problem. It is possible that, because this data was collected over several days, an adjustment in alignment from day-to-day caused the discrepancies seen at 140 K and 160 K. Changes in alignment could also have caused different parts of the samples to be stimulated, which could account for the possible problems. Finally, information regarding the filters being used could have been incorrectly recorded in the light-light LabVIEW program, which would result in miscalculation of data. Again, the 140 K and 160 K data points cannot be confirmed to be invalid without further testing and data confirmation.

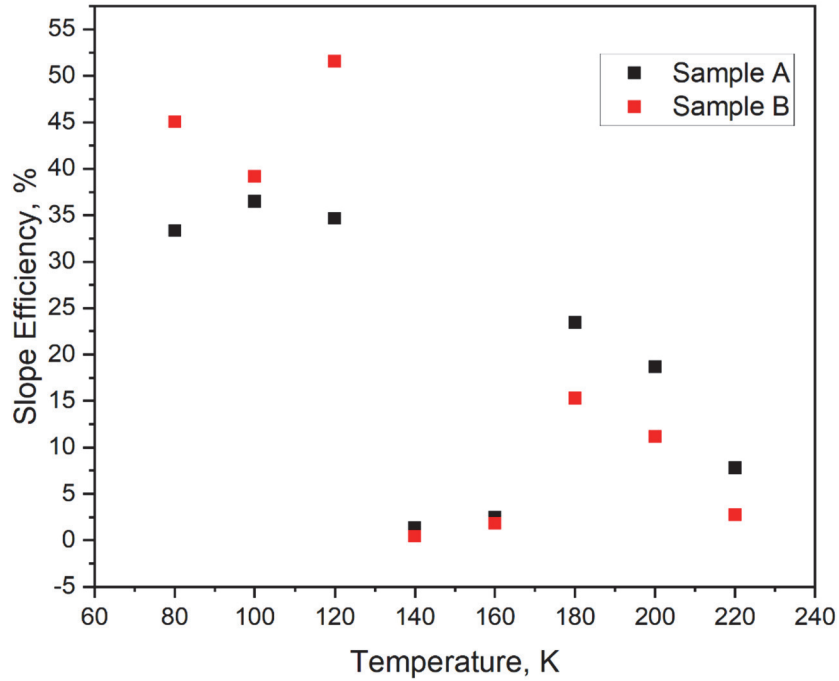


Figure 4.5. Plot of slope efficiency versus temperature for samples A and B at 1950 nm pump wavelength.

In addition to evaluating light-light curves with a fixed pump wavelength and a range of temperatures, it can be valuable to plot with a fixed temperature and a range of pump wavelengths. Figure 4.6 shows a fan of light-light curves for sample A at 100 K over a range of pump wavelengths from 1800 nm to 1950 nm. Figure 4.7 also shows a fan of light-light curves at 100 K over a range of pump wavelengths from 1800 nm to 1950 nm, but for sample B instead. There seems to be a general trend of increasing threshold intensity and decreasing slope efficiency with increasing pump wavelength, with some exceptions.

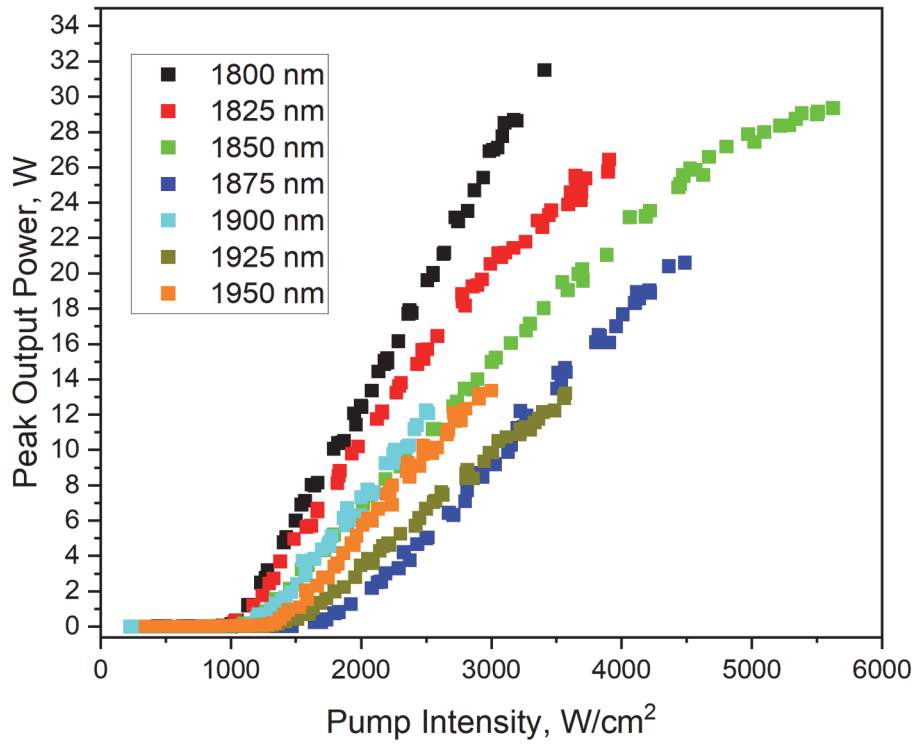


Figure 4.6. Fan of light-light curves for sample A at 100 K over a range of pump wavelengths.

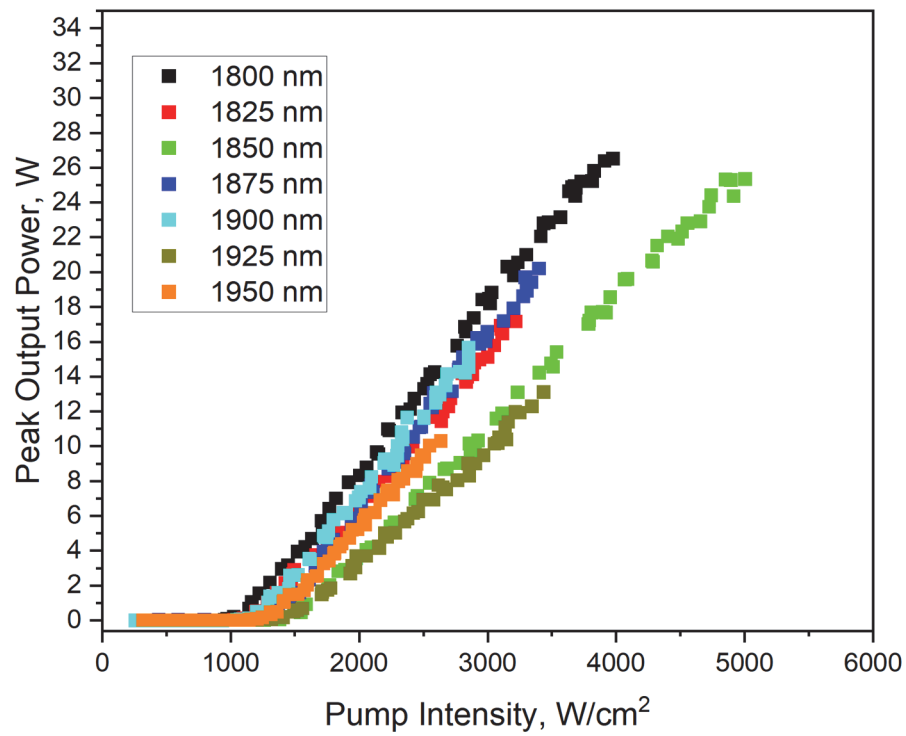


Figure 4.7. Fan of light-light curves for sample B at 100 K over a range of pump wavelengths.

Figure 4.8 shows a plot of threshold pump intensity versus pump wavelength for both samples A and B. The trend regarding threshold intensity dependence on pump wavelength is much less obvious when compared to the temperature dependence. In this case, an increase in threshold intensity with increasing pump wavelength does occur, and that is seen by the slope of the linear fit lines applied to both data sets. However, the very low R-Square values for each curve indicate that there is not a reliable trend in the data. There is not an obvious distinction to be made between the pump intensities of samples A and B as they relate to pump wavelength, though generally for a given pump wavelength at 100 K the threshold for Sample A was lower than the threshold for Sample B.

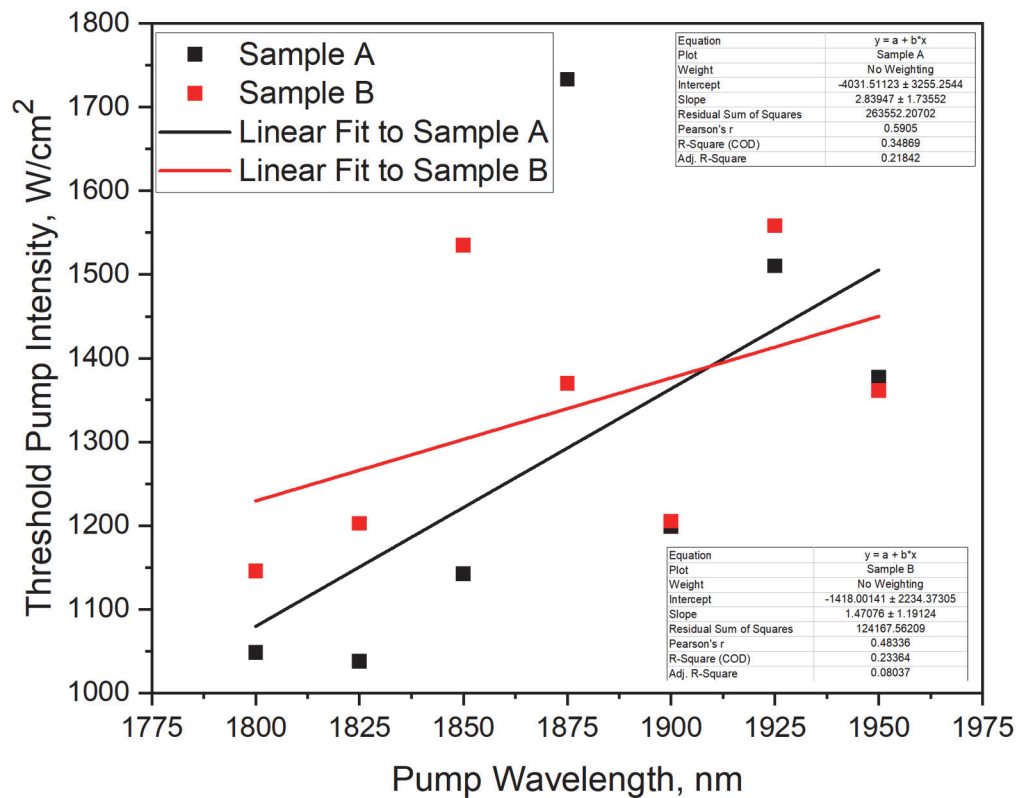


Figure 4.8. Plot of threshold intensity versus pump wavelength for samples A and B at 100 K. Linear fits were applied to both data sets and the pertinent fit data is included in the corresponding tables.

Figure 4.9 shows a plot of slope efficiency versus pump wavelength for samples A and B. Again the dependence of slope efficiency on pump wavelength is much less obvious when compared to the temperature dependence presented earlier in this thesis. There is still a slight decrease in slope efficiency with increasing pump wavelength, which is evidenced by the slope of the linear fits applied to both data sets. However, the R-Square values for both linear fits do indicate that there is not a reliable trend in the data. Like the threshold intensity above, there is not an obvious distinction to be made between sample A and B. It does not appear that graphene strongly affects either the slope efficiency or threshold intensity as pump wavelength changes, though at 100 K, there is more consistent behavior and less variation for Sample B than for Sample A.

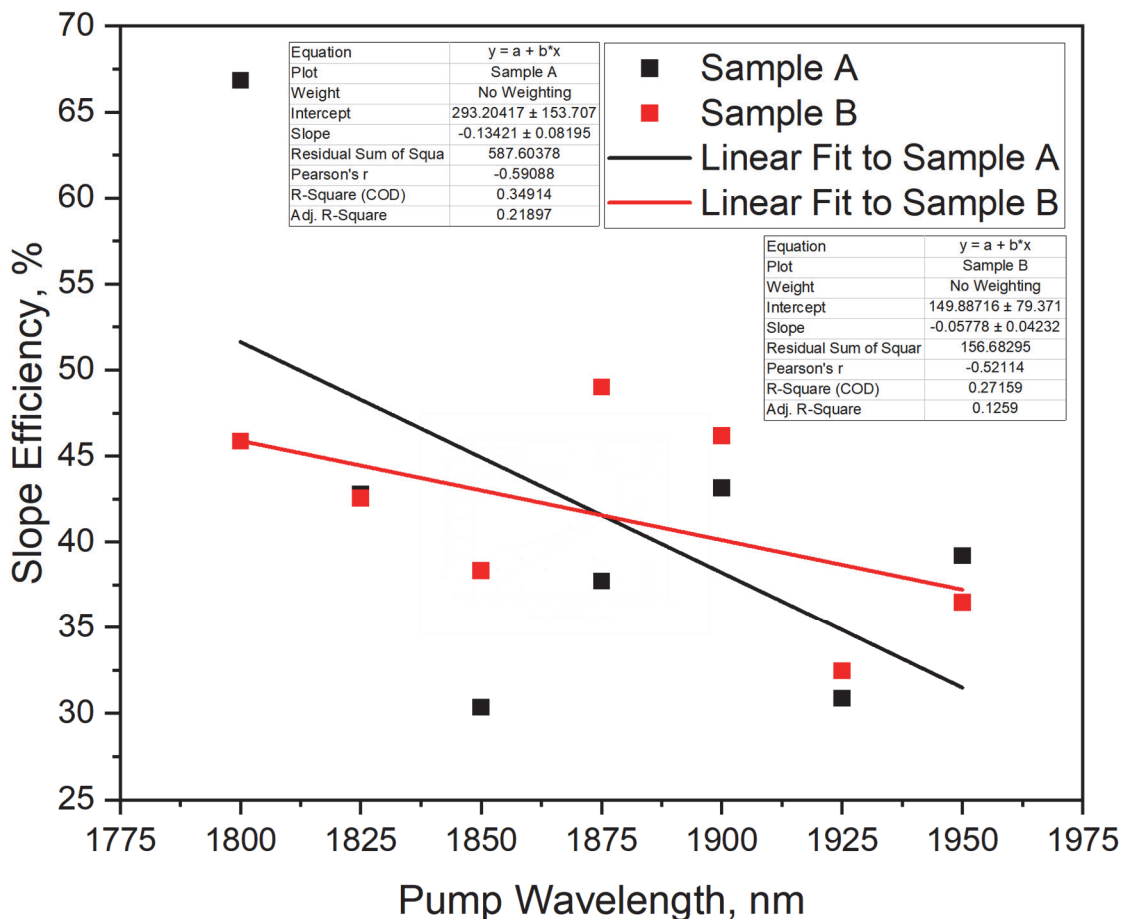


Figure 4.9. Plot of slope efficiency versus pump wavelength for samples A and B at 100 K. Linear fits were applied to both data sets and the pertinent fit data is included in the corresponding tables.

The peak output power for all light-light curves is the subject of ongoing work. Based on previous data, a reasonable peak output power was expected to be approximately an order of magnitude less than the data that was collected. While much calibration work was done to evaluate these larger sample powers, nothing seemed to effect a significant correction. One possible explanation for the large powers is that the pump stripe width for the collected data was very wide compared to that of previous work (1 mm compared to 0.2-0.3 mm). A wider pump stripe would mean that a larger area of each sample was being pumped, and thus the effective gain medium volume was

larger than expected. Compared to previous work, the pump stripe was approximately three times as large. In principle, this would produce three times as much output power. Also, a wider pump stripe would result in a wider sample output beam. Because the diameter of the detector was fixed, a wider output beam would mean that less of the beam overlapped with the detector, which resulted in a lower calculated detector collector efficiency. Both factors could explain the much higher measured powers. However, future work is still required to confirm the validity of the measured power data. All this considered, the general nature of the sample output can be observed, because the powers should all scale together.

While the light-light data collected was important in observing performance and potential of the ICL samples, another important aspect of this work was collection of spectral data for samples A and B. With the use of the laboratory's new Horiba iHR550 spectrometer, the spectral data for samples A and B with varying temperature and pump wavelength were collected. The measurement as a function of pump wavelength is one of the novel aspects of this thesis work. Figures 4.10 and 4.11 show the emitted spectra for Sample A and Sample B, respectively at 80 K over a pump wavelength range of 1800 nm to 1950 nm. From visual inspection, it appears that there is no significant trend in changing center wavelength or FWHM with varying pump wavelength. The center wavelength and FWHM are found from Gaussian fits to the spectra data is shown in tables in Appendix B. The decrease in amplitude in the 1875 nm and 1900 nm data is believed to be due to a reduced level of liquid nitrogen in the spectrometer detector at the time of collection. This phenomenon is not seen at other temperatures, which leads to the belief that it is not due to changes in intensity and is not actual amplitude.

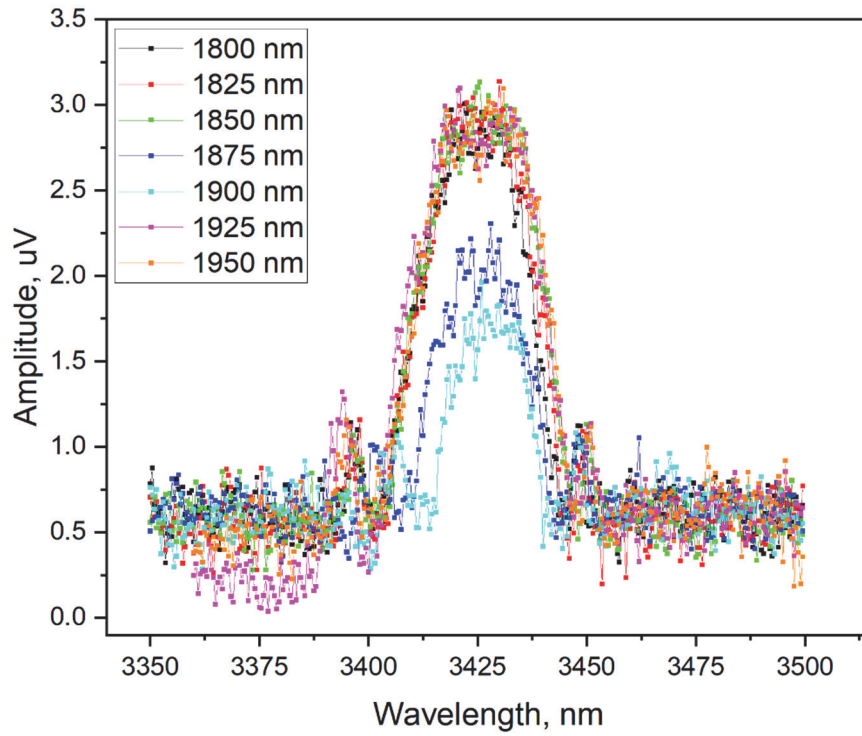


Figure 4.10. Spectral output of sample A at 80 K over a variety of pump wavelengths.

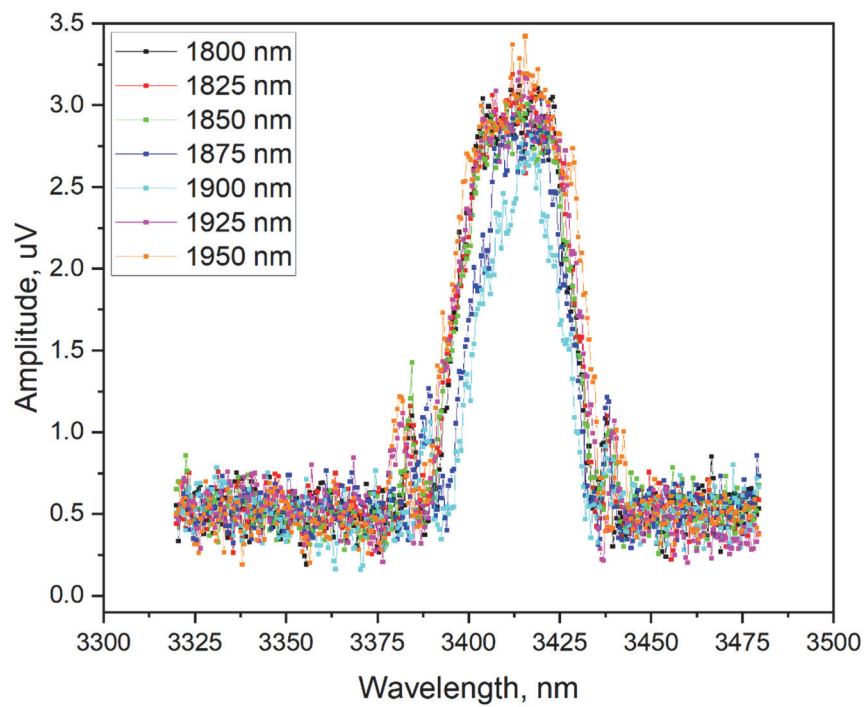


Figure 4.11. Spectral output of sample B at 80 K over a variety of pump wavelengths.

While pump wavelength does not seem to have an effect on sample output wavelength at a given temperature, it is clear that there is a relationship between sample temperature and output wavelength. Figures 4.12 and 4.13 show the spectra for 1800 nm pump wavelength at temperatures ranging from 80 K to 200 K for samples A and B respectively. With increasing temperature the center wavelength of the samples increases.

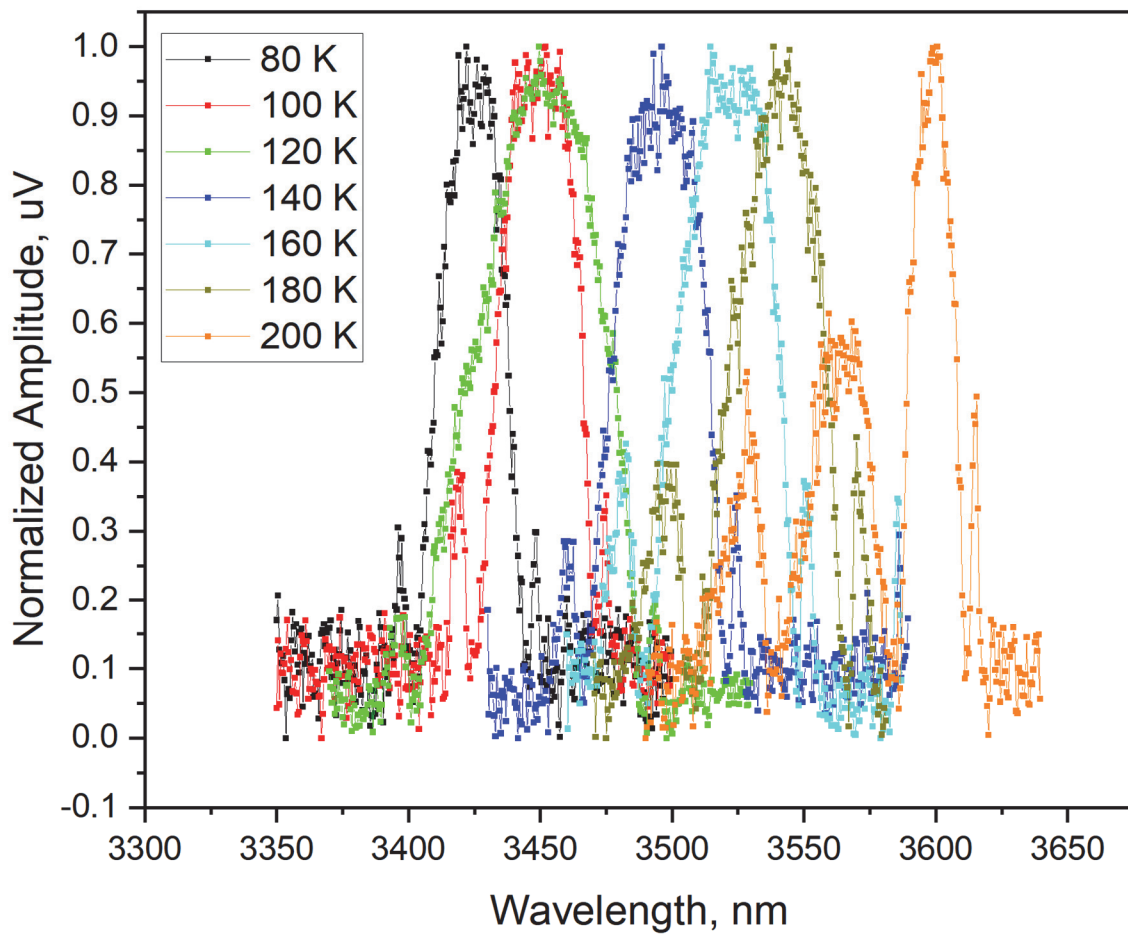


Figure 4.12. Spectral output of sample A at 1800 nm pump wavelength and temperatures from 80 K to 200 K.

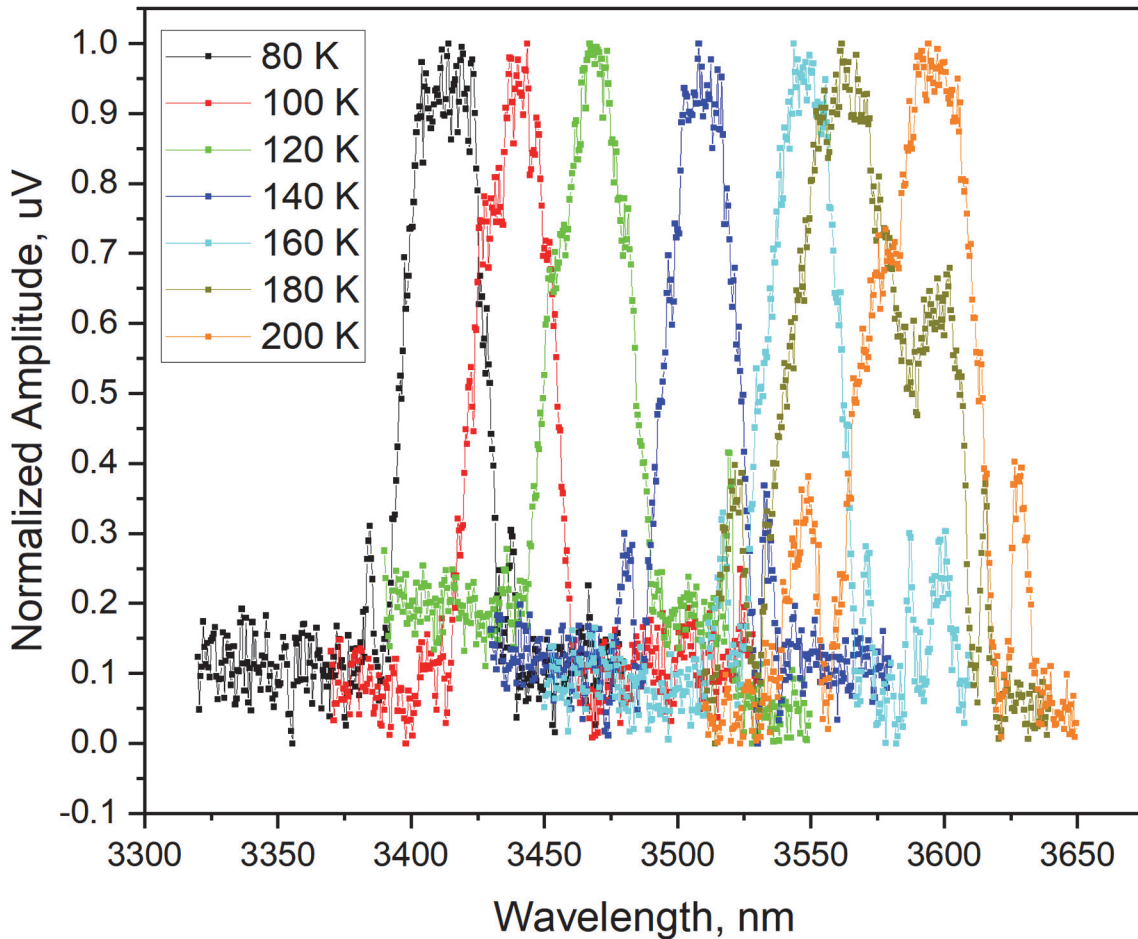


Figure 4.13. Spectral output of sample B at 1800 nm pump wavelength and temperatures from 80 K to 200 K.

Figure 4.14 shows a plot of center wavelength versus temperature for sample A, and it shows that there is an increase in center wavelength variation with increasing temperature. Changing pump wavelength does not significantly affect the center wavelength of the output spectra. Also, Figure 4.14 shows the sample graph for sample B, and the same observation is verified. However, it was observed that the range of center wavelengths (maximum – minimum) at a given temperature was greater in sample A than in sample B. These center wavelengths were found by fitting a Gaussian curve to each of the curves in Figures 4.12 and 4.13. The data seems to indicate that sample B, which had

the graphene monolayer did not experience as much variation in center wavelength with changing temperature when compared to sample A, which had no graphene. Another way of putting this is that sample B, with the graphene, appears to be slightly more stable when it comes to center wavelength than sample A. Figure 4.16 plots the range in center wavelengths versus temperature for samples A and B. The ranges were calculated by finding the difference between the maximum and minimum center wavelength at each temperature. There is a linear increase in the range in center wavelengths with increasing temperature. This is shown by the linear fit lines shown in Figure 4.16. The R-Square values for both fits indicate a linear relationship. However, more data points (e.g. additional wavelengths and temperatures) are needed to confirm the linearity of that trend.

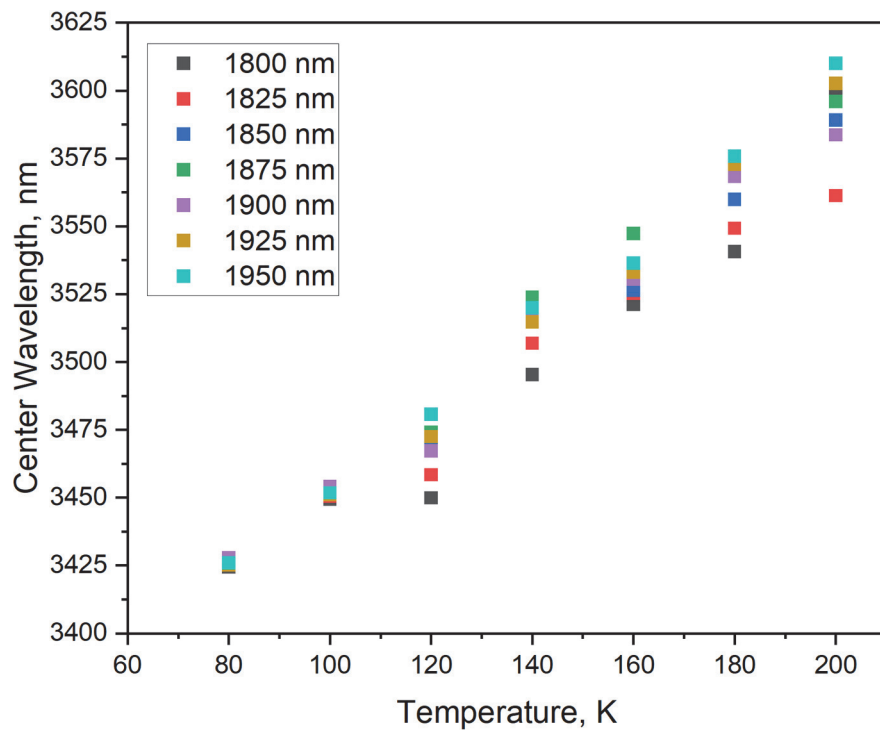


Figure 4.14. Center wavelength versus temperature for Sample A.

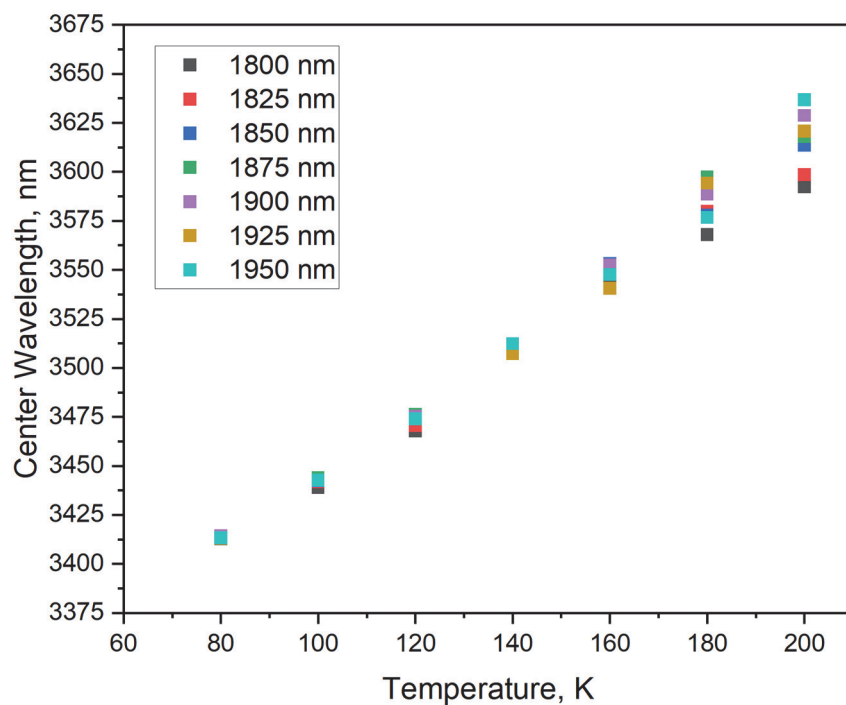


Figure 4.15. Center wavelength versus temperature for Sample B.

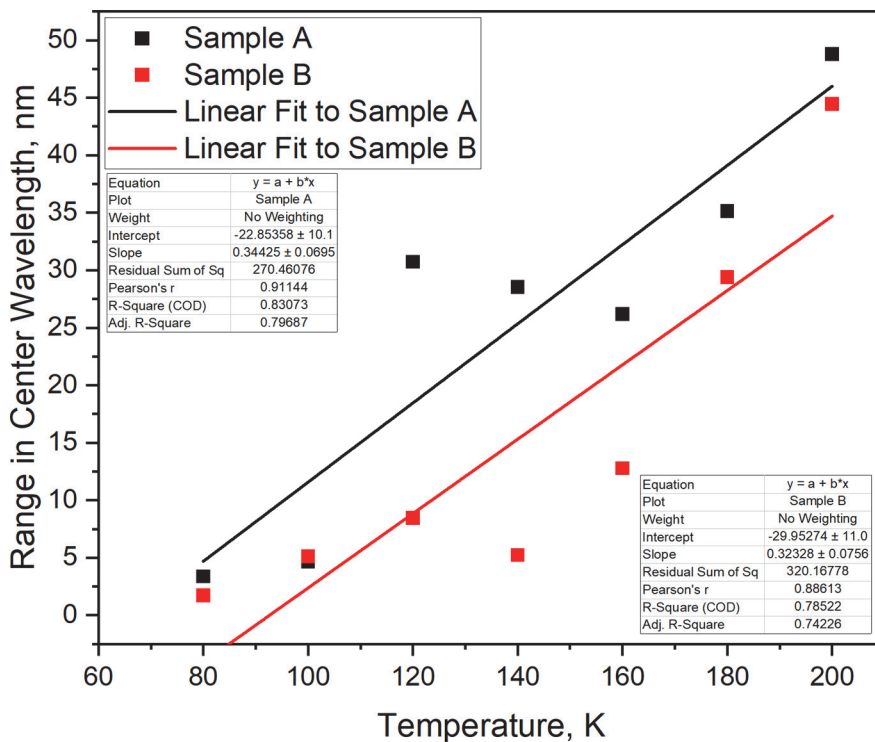


Figure 4.16. Range in sample A and B center wavelengths versus temperature.

From the data in Figures 4.14 and 4.15, it is possible to develop an approximation for how much the center wavelength of the samples changes per degree Kelvin. This data was found by making linear fits to center wavelength versus temperature for each pump wavelength. This information is valuable for future research, as it can provide a method of accurately predicting the center wavelength and thus the sample output wavelength based on the temperature of the sample. Table 4.1 shows the change in center wavelength for both samples A and B at all tested pump wavelengths, and Figure 4.17 is a plot of the same data. From the included linear fit lines, there is a clear linear increase in the change in center wavelength per degree Kelvin with increasing temperature for Sample B. The R-Square value of 0.90 for the Sample B fit shows that the fit is reliable. The linearity of the trend for Sample B warrants further investigation of how the graphene contact may bend bands or effect carrier dynamics. Based on the slope of the applied fit to Sample A, there is a clear increase in center wavelength with increasing temperature. However, the R-Squared value of 0.25 indicates a less reliable linear trend than for Sample B.

Table 4.1. Change in center wavelength per degree Kelvin for both samples.

Sample	Pump Wavelength (nm)	Change in Center Wavelength per Degree Kelvin (nm/K)
T080122	1800	1.453
	1825	1.134
	1850	1.360
	1875	1.417
	1900	1.299
	1925	1.479
	1950	1.534
T080122 (graphene monolayer)	1800	1.496
	1825	1.546
	1850	1.672
	1875	1.697
	1900	1.786
	1925	1.730
	1950	1.861

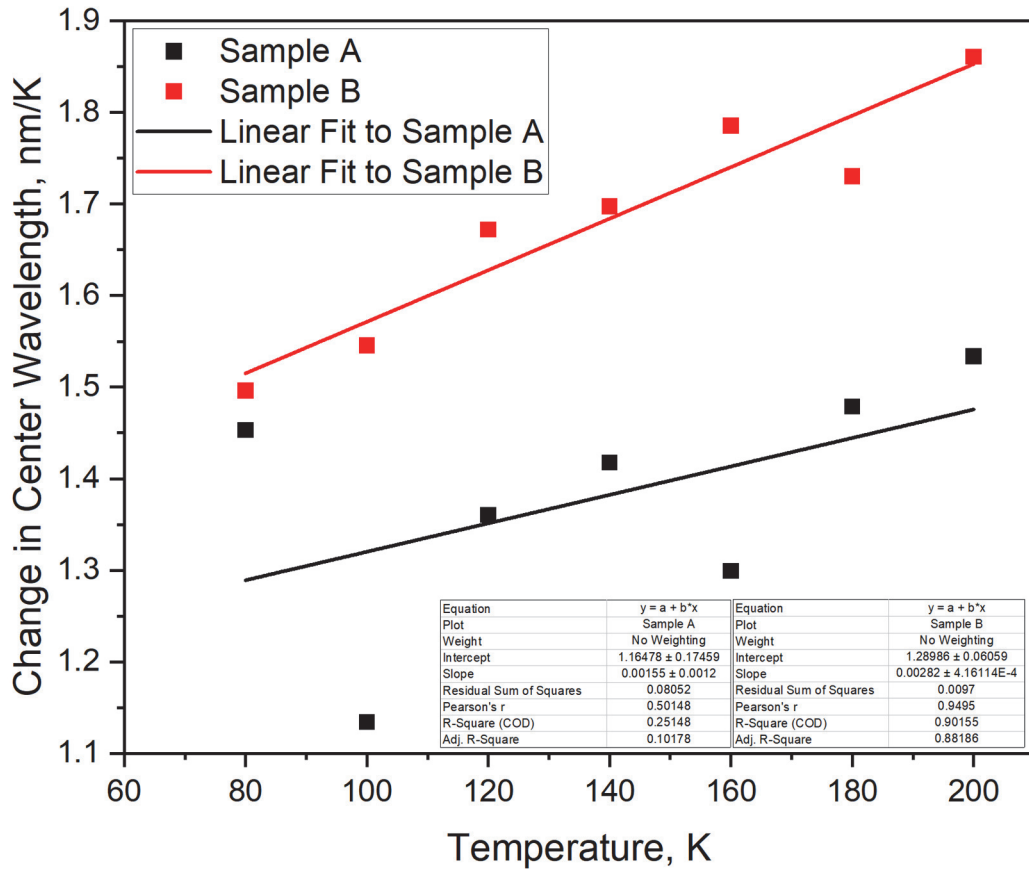


Figure 4.17. Plot of the change in center wavelength per degree Kelvin for both samples A and B. Linear fits were applied to both data sets and the pertinent fit values are shown in the included tables.

All of this data is useful for future data collection, because it provides information for an experimenter to predict how different ICL sample characteristics change with temperature and pump wavelength. There is some work needed to verify or correct for the very high powers measured in the light-light figures. However, the trends and characteristics observed in the data are all still believed to be accurate and reliable.

CHAPTER FIVE

Conclusion

This study shows preliminary results of the effects of temperature and pump wavelength on the output of two different ICL samples. With and without a graphene top contact. A Nd:YAG laser was used to pump an OPO, which was in turn being used to control the pump wavelength. The pump beam was guided from the OPO output to the samples using various mirrors and lenses that did height adjustment, telescoping, and intensity control using polarization. Neutral density filters were used to further control the overall intensity of the pump beam and sample output beam. While future work is needed to verify or correct observed output sample powers, there were trends of note in spectral data and threshold intensities as a function of temperature and of pump wavelength. With increasing temperature, the center wavelength of the sample output increases approximately 1.5 nm/K (see Table 4.1 for exact values). This data can be used during future data collection to help accurately predict the center wavelength of the two tested samples. Of particular interest is the potential effect of graphene on stability of spectra as a function of pump wavelength as well as the linear increase in the change of center wavelength per temperature as a function of pump wavelength. This warrants further investigation of the effect of the graphene-semiconductor top contact. This is especially valuable as one future goal of this laboratory is to study the sources of loss in ICL semiconductor materials. In order to best accomplish this goal, it is crucial to know as many operating parameters as possible so that loss can be isolated and future device designs may be improved.

As mentioned, there is much promising future work to be carried out regarding semiconductor ICLs. This data is a stepping stone to further understanding of how ICLs function and can be employed in various environments.

APPENDICES

APPENDIX A

LabVIEW Program Figures

OPO LabVIEW Control

Due to not being able to move the halfwave plate driver from the Windows 7 computer to the Windows 10 computer in the laboratory, the OPO LabVIEW control program was not used for this procedure. However, due to the amount of work needed to develop the program and the future applications, it was important to discuss. Figure A.1 shows the connection control panel for the OPO program.

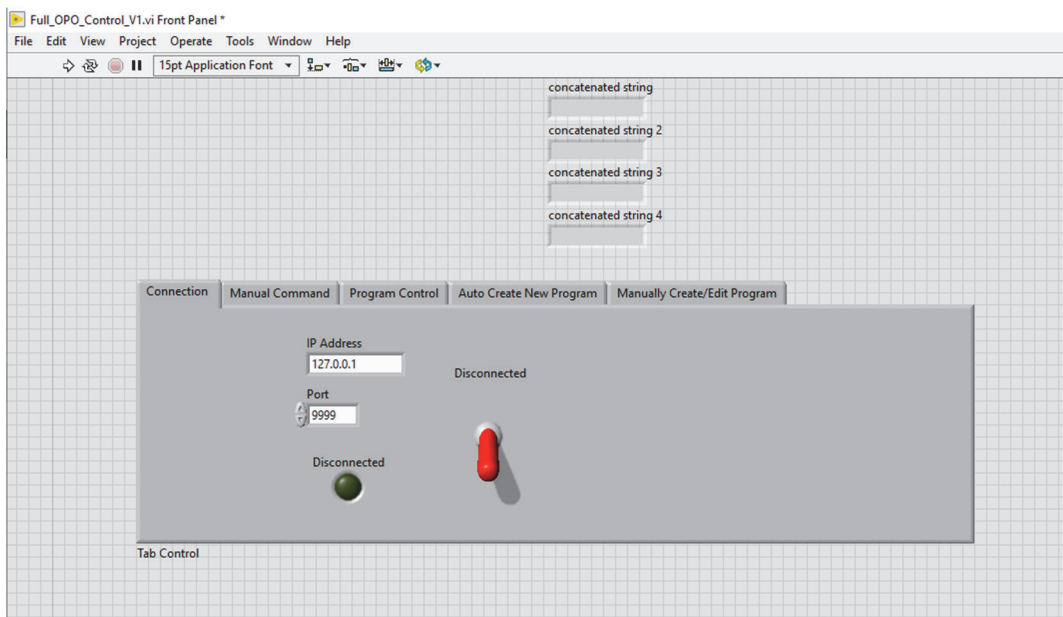


Figure A.1. Connection control panel of OPO program.

Besides the connection panel, the manual command tab was the most used function of the OPO control program. Figure A.2 shows the manual command input panel of the OPO

control that allows the user to write in specific, individual commands that are sent to the OPO.

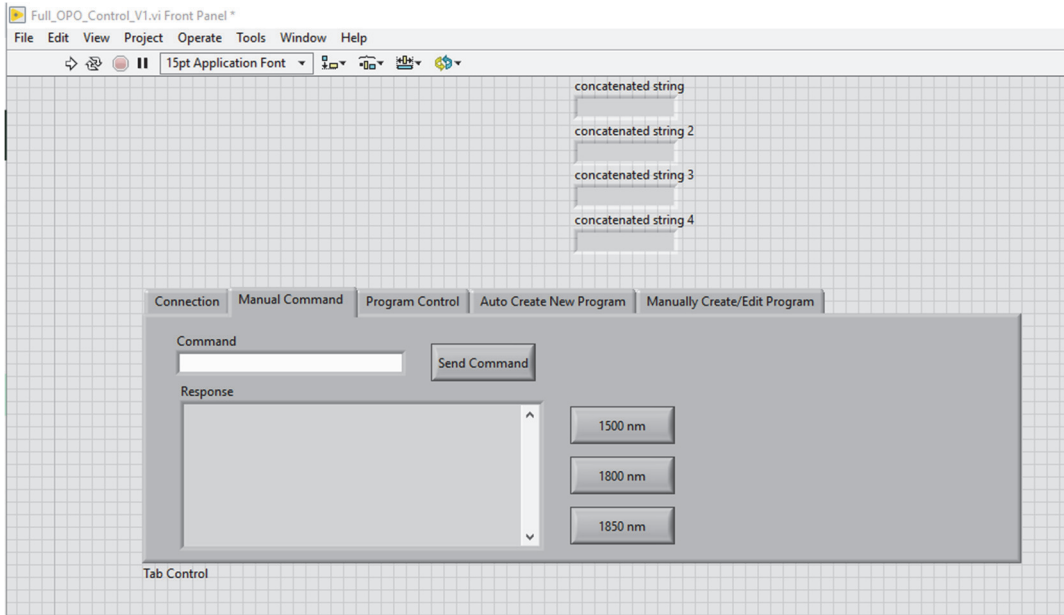


Figure A.2. Manual command input panel of OPO control.

The next panel in the program was the program control section, which allowed the user to load and run existing programs. Figure A.3 shows the program control panel of the OPO control LabVIEW program.

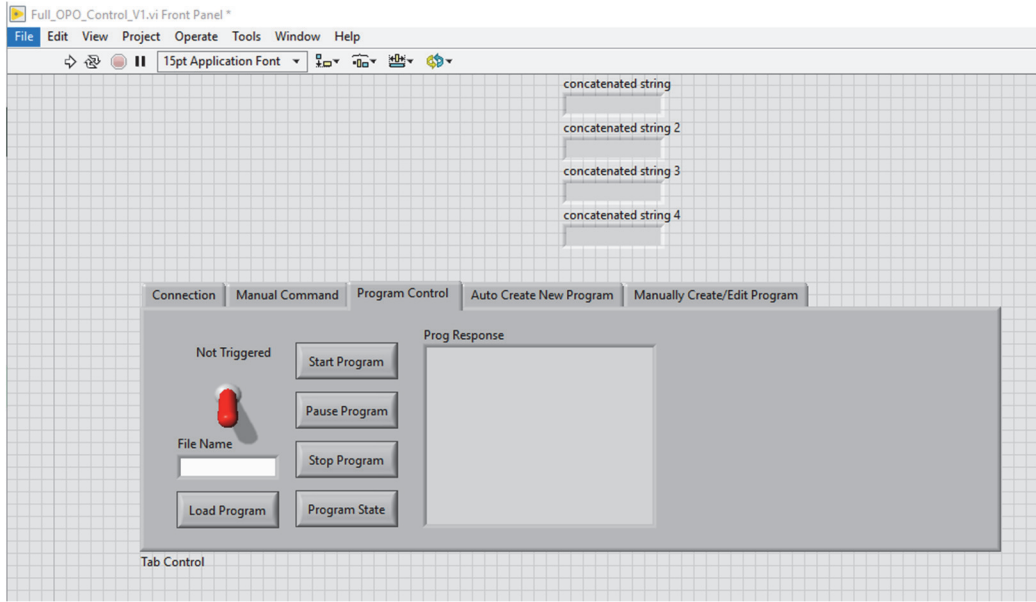


Figure A.3. The program control panel of the OPO control.

The first of the two program creation panels was the auto create new program tab. This section allowed the user to auto generate new programs based on user inputs. Figure A.4 shows the auto create new program front panel.

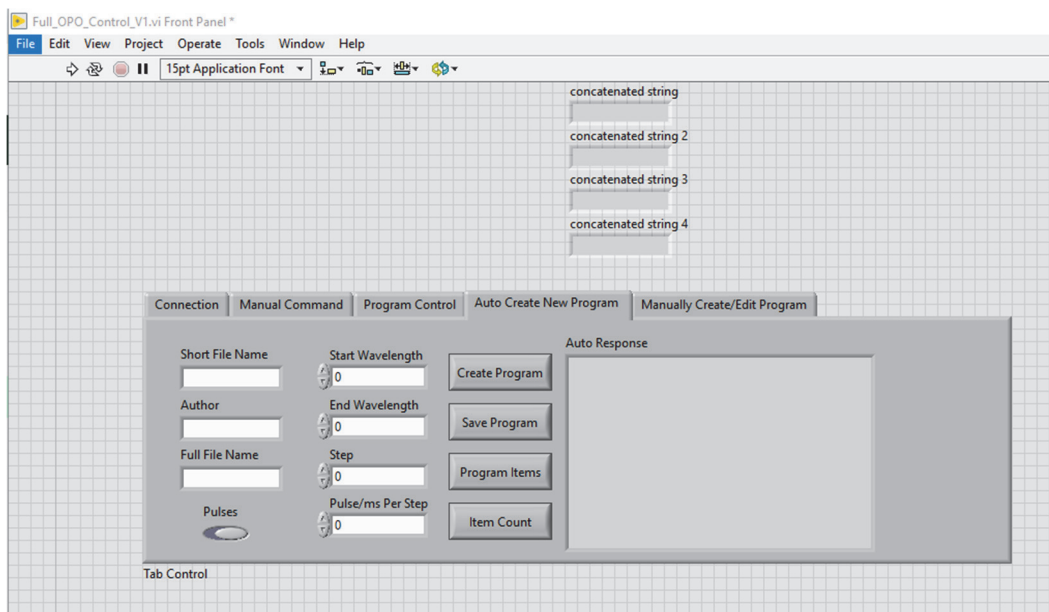


Figure A.4. The auto create new program panel of the OPO control.

The final section of the OPO control was the manually create/edit program panel. This tab allowed the user to create programs with much more detailed control than that provided on the auto program panel. The manually create/edit program section is shown in Figure A.5.

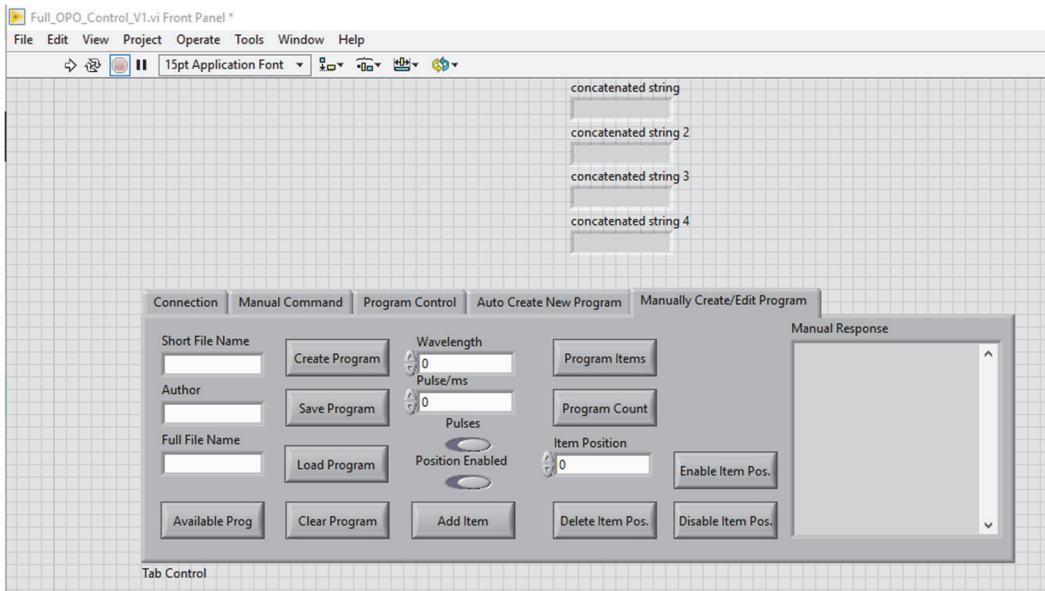


Figure A.5. The manually create/edit program tab of the OPO control program.

Light-Light Program Control

The following figures show the different tabs available to the user in the light-light program used to produce much of the data in this thesis. The program was modified from those previously used in the same laboratory. Primarily, the communication protocol used to communicate with Boxcar Averager was updated, because updates to the laboratory setup prevented communication with the device. Also, a large, green LED icon was added to the program as a visual cue to the use to change the pump wavelength at the appropriate time during data collection.

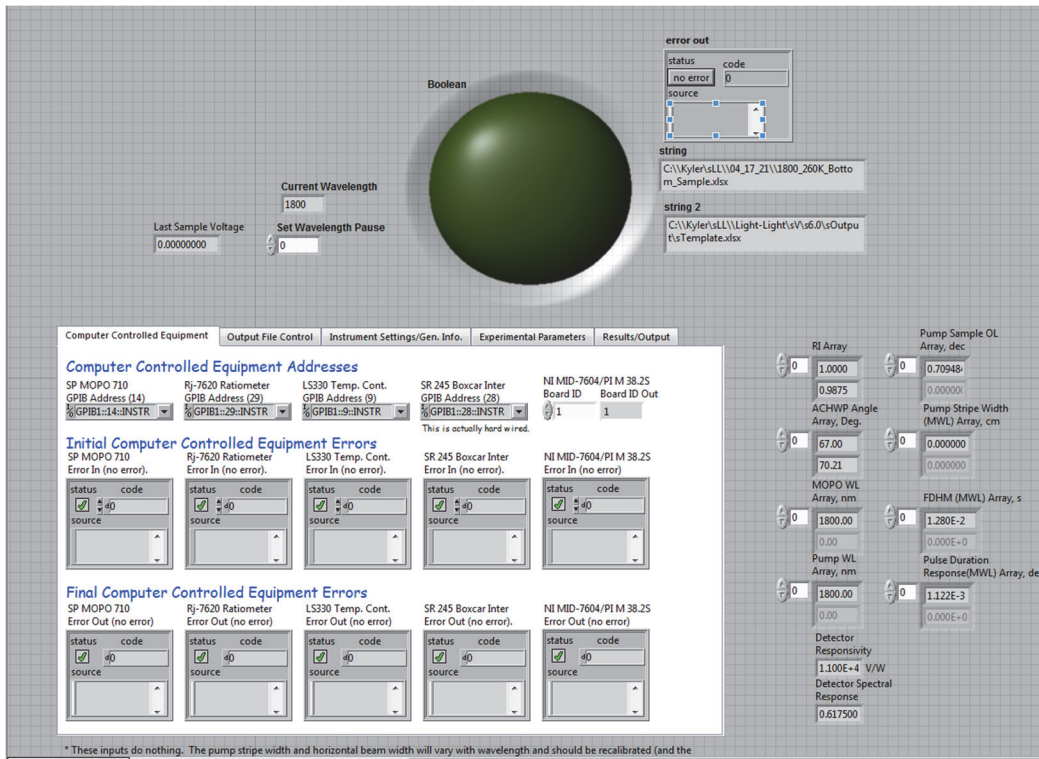


Figure A.6. The computer-controlled equipment panel of the light-light program.

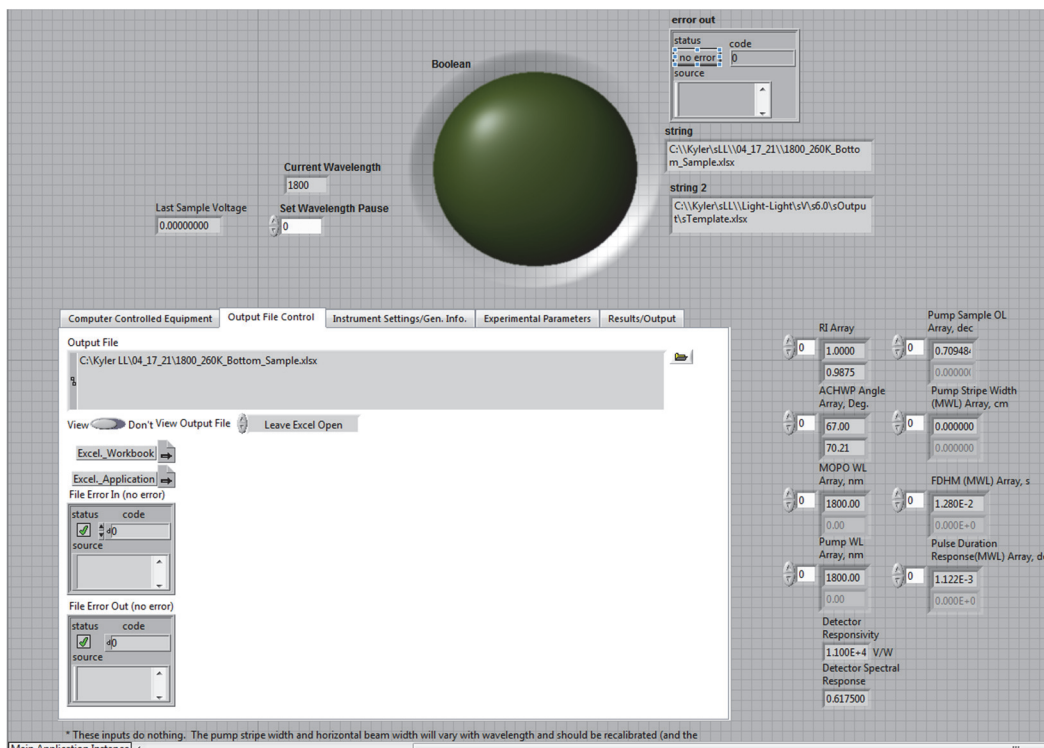


Figure A.7. The output file panel of the light-light program.

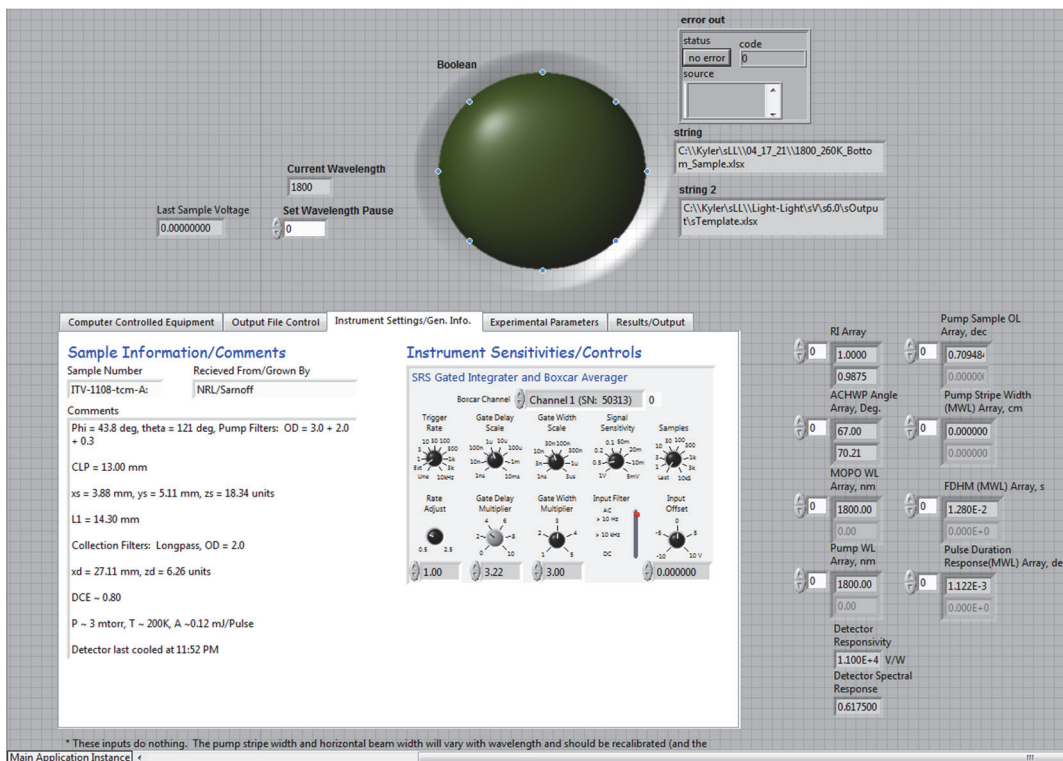


Figure A.8. The instrument settings/general info panel of the light-light program.

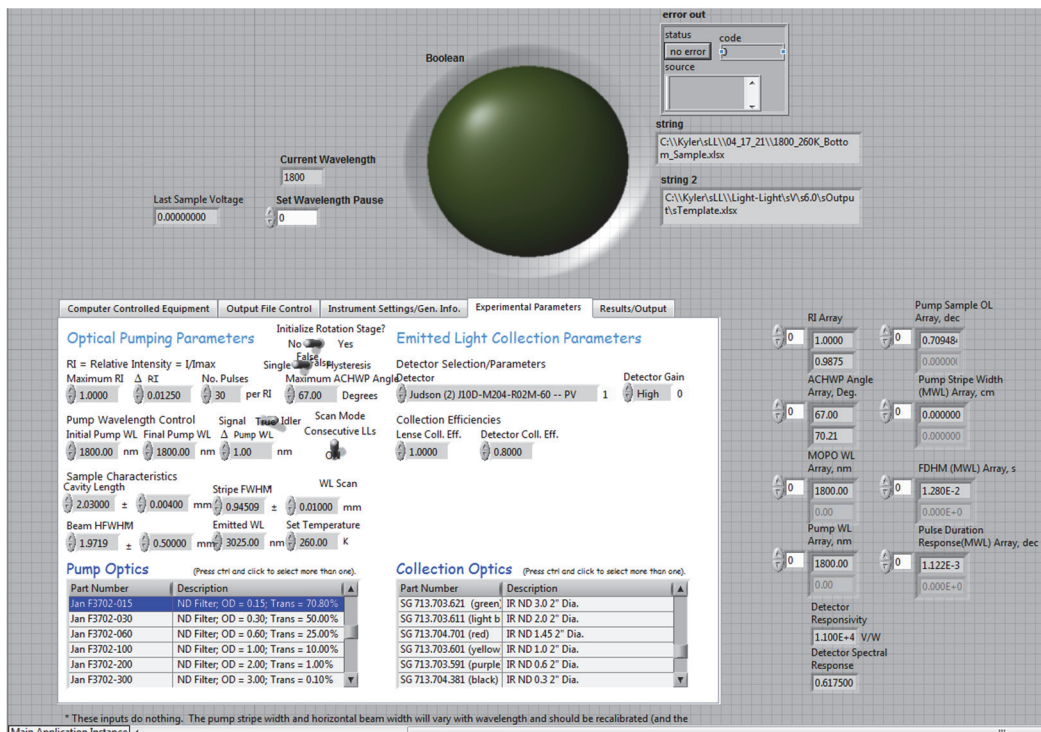


Figure A.9. The experimental parameters panel of the light-light program.

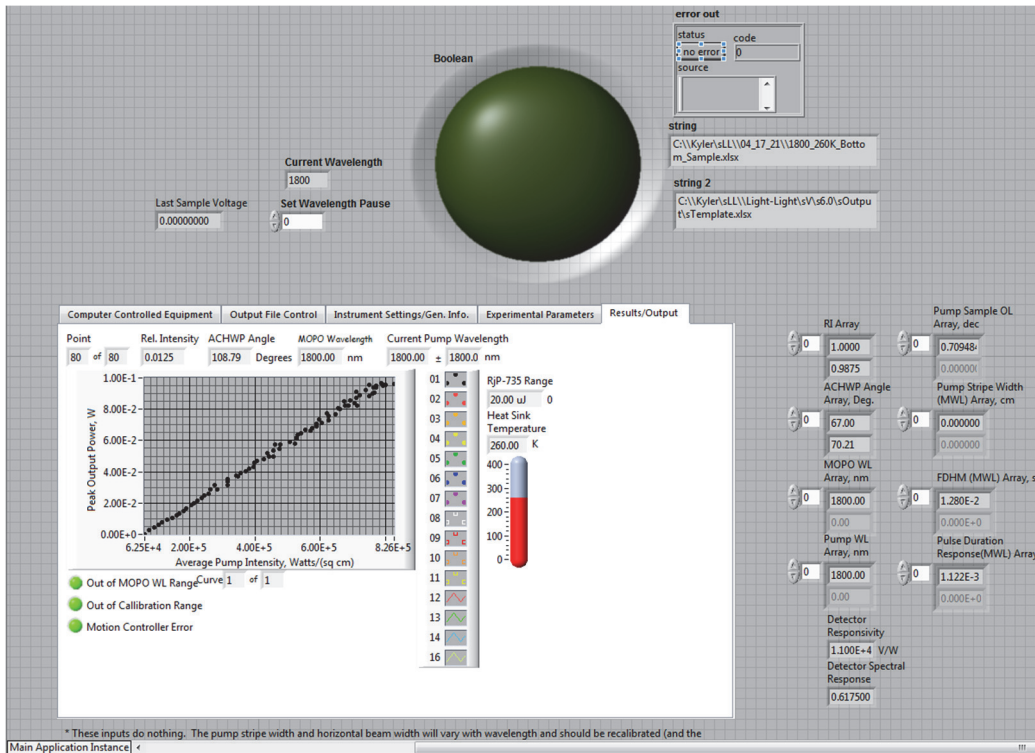


Figure A.10. The results/output panel of the light-light program.

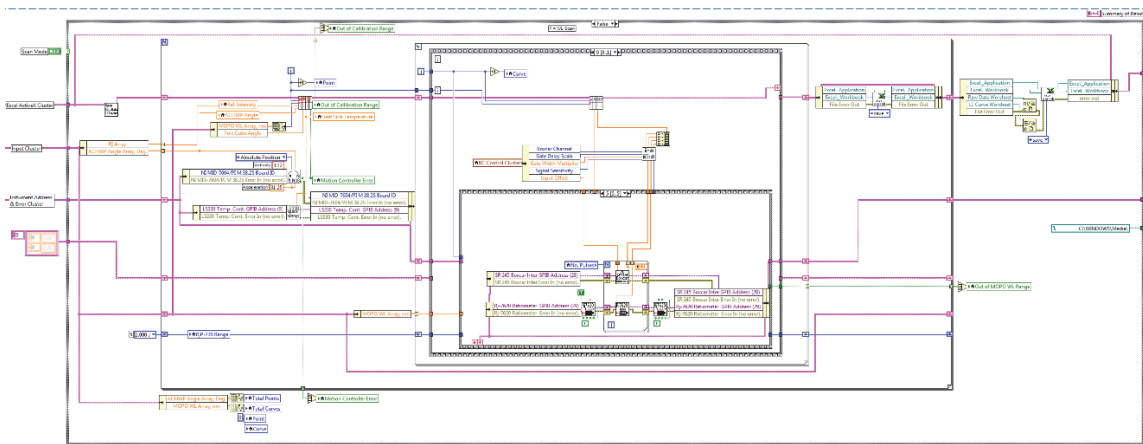


Figure A.11. Block diagram of light-light program when doing a single scan. Not shown in this figure is the many sub layers in this loop, the loop doing configuration, and setup to the left of this figure, and the process of closing any opened files and putting equipment in standby mode to the right of this figure.

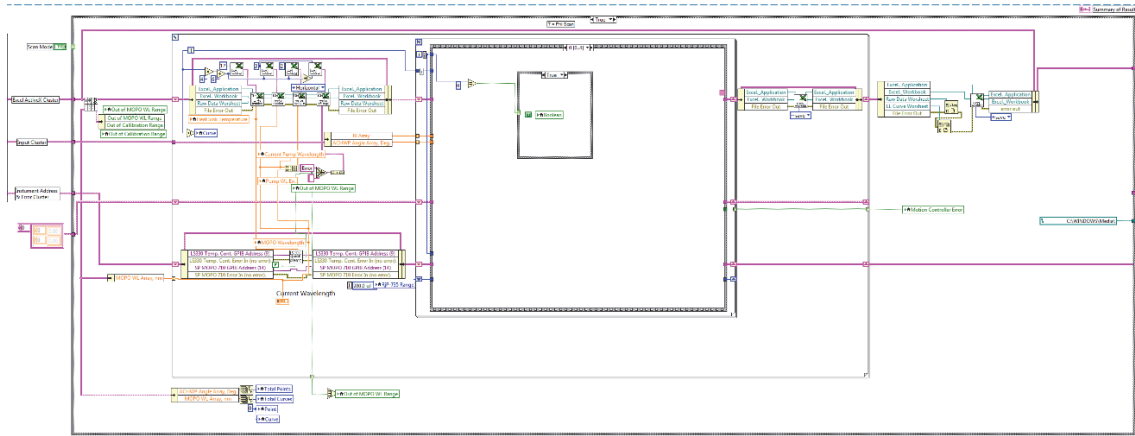


Figure A.12. Block diagram for of light-light program when doing a hysteresis scan. Not shown in this figure is the many sub layers in this loop, the loop doing configuration, and setup to the left of this figure, and the process of closing any opened files and putting equipment in standby mode to the right of this figure.

APPENDIX B

Additional Data Tables

Center Wavelengths

Table B.1 Center wavelength data for Samples A and B over a range of temperatures being pumped at 1800 nm

Sample	Temperature (K)	Center Wavelength (nm)
T080122	80	3424.40
	100	3449.51
	120	3449.96
	140	3495.33
	160	3521.13
	180	3540.66
	200	3598.77
T080122 (graphene monolayer)	80	3412.72
	100	3438.89
	120	3467.81
	140	3508.93
	160	3546.96
	180	3567.90
	200	3592.27

Table B.2 Center wavelength data for Samples A and B over a range of temperatures being pumped at 1825 nm

Sample	Temperature (K)	Center Wavelength (nm)
T080122	80	3425.17
	100	3450.52
	120	3470.48
	140	3509.99
	160	3549.68
	180	3579.90
	200	3598.50
T080122 (graphene monolayer)	80	3413.04
	100	3441.83
	120	3458.38
	140	3506.94
	160	3525.21
	180	3549.24
	200	3561.24

Table B.3 Center wavelength data for Samples A and B over a range of temperatures being pumped at 1850 nm

Sample	Temperature (K)	Center Wavelength (nm)
T080122	80	3425.91
	100	3451.81
	120	3468.07
	140	3521.49
	160	3526.38
	180	3559.93
	200	3589.17
T080122 (graphene monolayer)	80	3412.93
	100	3442.32
	120	3475.43
	140	3511.16
	160	3553.35
	180	3577.89
	200	3613.60

Table B.4 Center wavelength data for Samples A and B over a range of temperatures being pumped at 1875 nm

Sample	Temperature (K)	Center Wavelength (nm)
T080122	80	3425.86
	100	3453.00
	120	3474.11
	140	3523.86
	160	3547.32
	180	3571.71
	200	3595.94
T080122 (graphene monolayer)	80	3414.31
	100	3444.00
	120	3476.28
	140	3511.48
	160	3548.62
	180	3597.28
	200	3618.00

Table B.5 Center wavelength data for Samples A and B over a range of temperatures being pumped at 1900 nm

Sample	Temperature (K)	Center Wavelength (nm)
T080122	80	3427.76
	100	3454.15
	120	3467.16
	140	3518.13
	160	3530.44
	180	3568.34
	200	3583.67
T080122 (graphene monolayer)	80	3414.44
	100	3442.80
	120	3475.17
	140	3511.09
	160	3552.36
	180	3588.57
	200	3628.71

Table B.6 Center wavelength data for Samples A and B over a range of temperatures being pumped at 1925 nm

Sample	Temperature (K)	Center Wavelength (nm)
T080122	80	3425.17
	100	3451.12
	120	3472.47
	140	3514.77
	160	3533.06
	180	3572.73
	200	3602.62
T080122 (graphene monolayer)	80	3413.11
	100	3442.60
	120	3473.95
	140	3507.08
	160	3540.58
	180	3594.22
	200	3620.75

Table B.7 Center wavelength data for Samples A and B over a range of temperatures being pumped at 1950 nm

Sample	Temperature (K)	Center Wavelength (nm)
T080122	80	3425.99
	100	3451.75
	120	3480.68
	140	3519.93
	160	3536.43
	180	3575.80
	200	3610.04
T080122 (graphene monolayer)	80	3413.41
	100	3442.69
	120	3473.97
	140	3512.32
	160	3547.63
	180	3576.70
	200	3636.72

Threshold Intensities

Table B.8. Threshold pump intensity data plotted in Figure 4.4. Samples A and B at 1950 nm pump wavelength.

Sample	Temperature (K)	Threshold Pump Intensity (nm)
T080122	80	1302.96
	100	1284.33
	120	977.68
	140	2305.61
	160	2284.86
	180	2143.98
	200	3088.49
	220	4036.30
T080122 (graphene monolayer)	80	1218.88
	100	1204.44
	120	1315.42
	140	1683.67
	160	1824.13
	180	1701.03
	200	2307.71
	220	3337.59

Table B.9. Threshold pump intensity data for Samples A and B at 1925 nm pump wavelength.

Sample	Temperature (K)	Threshold Pump Intensity (nm)
T080122	80	1374.00
	100	1510.15
	120	2897.29
	140	2900.02
	160	2996.01
	180	2214.92
	200	2861.17
	220	4566.23
T080122 (graphene monolayer)	80	1515.17
	100	1492.24
	120	1610.72
	140	3906.33
	160	2756.06
	180	1956.62
	200	3021.47
	220	4132.73

Table B.10. Threshold pump intensity data for Samples A and B at 1900 nm pump wavelength.

Sample	Temperature (K)	Threshold Pump Intensity (nm)
T080122	80	1376.79
	100	1198.91
	120	3563.07
	140	2586.96
	160	2588.81
	180	3202.25
	200	3042.80
	220	3895.82
T080122 (graphene monolayer)	80	1228.89
	100	1205.09
	120	1166.94
	140	1444.67
	160	1853.68
	180	1866.11
	200	2898.35
	220	4668.04

Table B.11. Threshold pump intensity data for Samples A and B at 1875 nm pump wavelength.

Sample	Temperature (K)	Threshold Pump Intensity (nm)
T080122	80	1186.96
	100	1787.77
	120	3612.51
	140	2989.46
	160	2550.44
	180	4181.84
	200	2743.60
	220	4661.78
T080122 (graphene monolayer)	80	1650.91
	100	1369.66
	120	1337.50
	140	1556.58
	160	2444.86
	180	1880.84
	200	3562.82
	220	4277.85

Table B.12. Threshold pump intensity data for Samples A and B at 1850 nm pump wavelength.

Sample	Temperature (K)	Threshold Pump Intensity (nm)
T080122	80	1268.82
	100	1266.83
	120	3934.92
	140	3175.49
	160	3294.02
	180	2620.25
	200	2473.94
	220	3621.08
T080122 (graphene monolayer)	80	4366.22
	100	1535.03
	120	1288.38
	140	1660.36
	160	3018.43
	180	1997.60
	200	2158.34
	220	3850.82

Table B.13. Threshold pump intensity data for Samples A and B at 1825 nm pump wavelength.

Sample	Temperature (K)	Threshold Pump Intensity (nm)
T080122	80	1038.38
	100	1037.74
	120	3764.70
	140	3509.39
	160	2912.64
	180	2525.46
	200	2272.98
	220	3662.23
T080122 (graphene monolayer)	80	1297.33
	100	1202.53
	120	1188.83
	140	1320.49
	160	1457.38
	180	1583.58
	200	1952.79
	220	2837.96

Table B.14. Threshold pump intensity data for Samples A and B at 1800 nm pump wavelength.

Sample	Temperature (K)	Threshold Pump Intensity (nm)
T080122	80	957.59
	100	1048.26
	120	4481.27
	140	3920.41
	160	2022.81
	180	3027.73
	200	2124.00
	220	5133.18
T080122 (graphene monolayer)	80	1214.05
	100	1145.56
	120	1388.36
	140	1148.34
	160	1482.71
	180	2299.86
	200	1921.08
	220	2315.09

Table B.15. Threshold pump intensity data plotted in Figure 4.8. Samples A and B at 100 K.

Sample	Pump Wavelength (nm)	Threshold Pump Intensity (nm)
T080122	1800	1048.26
	1825	1037.74
	1850	1142.20
	1875	1733.23
	1900	1198.91
	1925	1510.15
	1950	1376.96
T080122 (graphene monolayer)	1800	1145.56
	1825	1202.53
	1850	1535.03
	1875	1369.66
	1900	1205.09
	1925	1558.49
	1950	1361.40

Slope Efficiencies

Table B.16. Slope efficiency data plotted in Figure 4.5. Samples A and B at 1950 pump wavelength.

Sample	Temperature (K)	Slope Efficiency (%)
T080122	80	33.33
	100	36.49
	120	34.65
	140	1.35
	160	2.49
	180	23.43
	200	18.69
	220	7.81
T080122 (graphene monolayer)	80	45.03
	100	39.20
	120	51.57
	140	0.44
	160	1.83
	180	15.31
	200	11.18
	220	2.75

Table B.17. Slope efficiency data for Samples A and B at 1925 pump wavelength.

Sample	Temperature (K)	Slope Efficiency (%)
T080122	80	46.31
	100	31.70
	120	6.93
	140	0.65
	160	1.59
	180	13.19
	200	8.76
	220	2.60
T080122 (graphene monolayer)	80	27.40
	100	31.98
	120	31.38
	140	2.42
	160	2.08
	180	27.10
	200	14.27
	220	3.35

Table B.18. Slope efficiency data for Samples A and B at 1900 pump wavelength.

Sample	Temperature (K)	Slope Efficiency (%)
T080122	80	30.45
	100	45.95
	120	15.78
	140	1.21
	160	1.83
	180	1.53
	200	4.95
	220	2.99
T080122 (graphene monolayer)	80	37.40
	100	44.71
	120	35.28
	140	5.83
	160	5.34
	180	20.13
	200	19.33
	220	7.52

Table B.19. Slope efficiency data for Samples A and B at 1875 pump wavelength.

Sample	Temperature (K)	Slope Efficiency (%)
T080122	80	51.46
	100	42.02
	120	16.10
	140	1.17
	160	2.44
	180	1.35
	200	6.24
	220	2.02
T080122 (graphene monolayer)	80	34.02
	100	49.76
	120	45.03
	140	7.59
	160	2.75
	180	34.25
	200	19.48
	220	11.22

Table B.20. Slope efficiency data for Samples A and B at 1850 pump wavelength.

Sample	Temperature (K)	Slope Efficiency (%)
T080122	80	38.35
	100	29.19
	120	13.61
	140	0.68
	160	1.03
	180	1.00
	200	6.12
	220	2.11
T080122 (graphene monolayer)	80	0.47
	100	38.18
	120	41.62
	140	7.59
	160	5.70
	180	22.78
	200	16.08
	220	9.86

Table B.21. Slope efficiency data for Samples A and B at 1825 pump wavelength.

Sample	Temperature (K)	Slope Efficiency (%)
T080122	80	58.38
	100	38.49
	120	12.46
	140	0.69
	160	1.20
	180	0.97
	200	6.42
	220	2.83
T080122 (graphene monolayer)	80	42.29
	100	44.12
	120	43.24
	140	8.02
	160	6.27
	180	17.26
	200	12.48
	220	14.35

Table B.22. Slope efficiency data for Samples A and B at 1800 pump wavelength.

Sample	Temperature (K)	Slope Efficiency (%)
T080122	80	59.66
	100	64.85
	120	8.92
	140	0.96
	160	1.88
	180	1.27
	200	5.78
	220	3.24
T080122 (graphene monolayer)	80	37.65
	100	46.49
	120	41.08
	140	7.74
	160	4.95
	180	16.55
	200	8.92
	220	2.48

Table B.23. Slope efficiency data plotted in Figure 4.9. Samples A and B at 100 K.

Sample	Pump Wavelength (nm)	Slope Efficiency (%)
T080122	1800	66.84
	1825	42.80
	1850	30.35
	1875	37.72
	1900	43.14
	1925	30.89
	1950	39.20
T080122 (graphene monolayer)	1800	45.86
	1825	42.55
	1850	38.32
	1875	49.01
	1900	46.17
	1925	32.47
	1950	36.49

REFERENCES

- [1] R. Q. Yang, "Infrared laser based on intersubband transitions in quantum wells," *Superlatt. and Microstruc.*, vol. 77, no. 17, pp. 77–83, 1995.
- [2] C. H. Lin, R. Q. Yang, D. Zhang, S. J. Murry, S. S. Pei, A. A. Allerman, and S. R. Kurtz, "Type-II interband quantum cascade laser at 3.8 μm ," *Electronics Letters*, vol. 33, pp. 598–599, 1997.
- [3] S. Höfling, R. Weih, A. Bauer, M. Kamp, and A. Forchel, "Room temperature continuous wave interband cascade lasers for gas sensing," vol. 8432, pp. 84 320N1– 84 320N8, 2012.
- [4] J. Faist, F. Capasso, D. Sivco, C. S. A. Hutchinson, and A. Cho, "Quantum cascade laser," *Science*, vol. 264, pp. 553–556, 1994.
- [5] L. Shterengas, G. Belenky, T. Hosoda, G. Kipshidze, and S. Suchalkin, "Continuous wave operation of diode lasers at 3.36 μm at 12°C," *Applied Physics Letters*, vol. 93, no. 1, p. 011103, 2008.
- [6] A. Bauer, Matthias, M. Kamp, S. Höfling, L. Worschech, and A. Forchel, "Shortened injector interband cascade lasers for 3.3 to 3.6 μm emission," *Optical Engineering*, vol. 49, p. 111117, 2010.
- [7] S. B. Slivken, A. Evans, W. Zhang, and M. Razeghi, "High-power, continuous operation intersubband laser for wavelengths greater than 10 μm ," *Applied Physics Letters*, vol. 90, no. 15, p. 151115, 2007.
- [8] R. Q. Yang, J. L. Bradshaw, J. D. Bruno, J. T. Pham, and D. E. Wortman, "Midinfrared type-II interband cascade lasers," *IEEE Journal of Quantum Electronics*, vol. 38, no. 6, pp. 559–568, 2002.
- [9] B. A. Ikyo, I. P. Marko, A. R. Adams, S. J. Sweeney, C. L. Canedy, I. Vurgaftman, C. S. Kim, M. Kim, W. W. Bewley, and J. R. Meyer, "Temperature dependence of 4.1 μm mid-infrared type II "W" interband cascade lasers," *Applied Physics Letters*, vol. 99, no. 2, p. 021102, 2011.
- [10] C. J. Hill, B. H. Yang, and R. Q. Yang, "Low-threshold interband cascade lasers operating above room temperature," *Physica E*, vol. 20, pp. 486–490, 2004.
- [11] J. R. Meyer, C. A. Hoffman, F. J. Bartoli, and L. R. Ram-Mohan, "Type-II quantum-well lasers for the mid-wavelength infrared," *Applied Physics Letters*, vol. 67, no. 6, pp. 757–759, 1995.

- [12] W. W. Bewley, C. L. Canedy, C. S. Kim, M. Kim, C. D. Merritt, J. Abell, I. Vurgaftman, and J. R. Meyer, "Continuous-wave interband cascade lasers operating above room temperature at $\lambda = 4.7\text{-}5.6\ \mu\text{m}$," *Optics Express*, vol. 20, pp. 3235–3240, 2012.
- [13] Olafsen, L.J.; Aifer, E.H.; Vurgaftman, I.; Bewley, W.W.; Felix, C.L.; Meyer, J.R.; Zhang, D.; Lin, C.H.; Pei, S.S. Near-room-temperature mid-infrared interband cascade laser. *Appl. Phys. Lett.* 1998, 72, 2370–2372
- [14] I. Vurgaftman, W. Bewley, C. Canedy, C. Kim, M. Kim, C. Merritt, J. Abell, J. Lindle, and J. Meyer, "Rebalancing of internally generated carriers for midinfrared interband cascade lasers with very low power consumption." *Nature Communications*, vol. 2, p. 585, 2011.
- [15] C. D. Merritt, W. W. Bewley, C. S. Kim, C. L. Candey, I. Vurgaftman, J. R. Meyer, and M. Kim, "Gain and loss as a function of current density and temperature in interband cascade lasers," *Applied Optics*, vol. 54, no. 31, pp. F1–F7, 2015.
- [16] Krzysztof Ryczko, Grzegorz Sęk, "Optimization of the active region of interband cascade lasers emitting in the MIR," *Proc. SPIE 10765, Infrared Remote Sensing and Instrumentation XXVI, 107650S* (18 September 2018); <https://doi.org/10.1117/12.2324642>
- [17] I. Vurgaftman, R. Weih, M. Kamp, J. R. Meyer, C. L. Canedy, C. S. Kim, M. Kim, W. W. Bewley, C. D. Merritt, J. Abell, and S. Höfling, "Interband cascade lasers," *Journal of Physics D*, vol. 48, pp. 3235–3240, 2015.
- [18] A. Yariv, *Quantum Electronics* (Wiley, New York, 1987).
- [19] H. Hogan, and M. Rose, "A History of the Laser: 1960 – 2019" 2020, [Online; accessed [17-June-2021]. [Online]. Available: https://www.photonics.com/Articles/A_History_of_the_Laser_1960_-_2019/a42279
- [20] Physics of atoms and molecules. *Physical Bog*. [Online]. Available: http://www.bog5.in.ua/lection/quantum_optics_lect/lect7_quant_eng.html
- [21] A. Einstein, "The quantum theory of radiation," *Physikalische Zeitschrift*, vol. 18, p. 121, 1917.
- [22] V. V. Mitin, V. A. Kochelap, and M. A. Strosio, *Quantum Heterostructures: Microelectronics and Optoelectronics*. New York: Cambridge University Press, 1999.
- [23] P. Y. Yu and M. Cardona, *Fundamentals of Semiconductors: Physics and Materials Properties*, 3rd ed. Berlin: Springer, 2001.

- [24] Wikipedia contributors, “Quantum cascade laser — Wikipedia, the free encyclopedia,” 2019, [Online; accessed 2-June-2019]. [Online]. Available: https://en.wikipedia.org/w/index.php?title=Quantum_cascade_laser&oldid=883963939
- [25] B. G. Streetman and S. Banerjee, Solid state electronic devices. Upper Saddle River, N.J.: Prentice Hall, 2000.
- [26] Electronics | Projects | Focus. What is Fermi Dirac Distribution? Energy Band Diagram, and Boltzmann Approximation. [Online] Available: <https://www.elprocus.com/fermi-dirac-distribution-energy-band-diagram-and-boltzmann-approximation/>
- [27] S. Wang, Fundamentals of Semiconductor Theory and Device Physics. Englewood Cliffs: Prentice Hall, 1989.
- [28] H. Kroemer, Quantum Mechanics: For Engineering, Materials Science, and Applied Physics. Englewood Cliffs: Prentice Hall, 1994.
- [29] R.-Q. Sun, J. Zhang, M. Zhang, and X. Wang, “A facile band alignment of polymeric carbon nitride semiconductors to construct isotype heterojunctions.” Chemie International Edition, vol. 51, pp. 10 145–10 149, 2012.
- [30] E. A. Johnson, Low Dimensional Semiconductor Structures: Fundamentals and Device Applications, K. Barnham and D. Vvedensky, Eds. Cambridge: Cambridge U P, 2001.
- [31] D. J. Griffiths, Introduction to Quantum Mechanics, 2nd ed. Upper Saddle River, NJ: Pearson Prentice Hall, 2005.
- [32] M. Kamp. Mid-infrared semiconductor lasers. [Online]. Available: https://wuecampus2.uni-wuerzburg.de/moodle/pluginfile.php/519978/mod_resource/content/1/Talk
- [33] “Quantum, Cascade Lasers”. Edmund Optics. [Online]. Available: <https://www.edmundoptics.com/knowledge-center/application-notes/lasers/quantum-cascade-lasers/>
- [34] “Quantum cascade lasers basics,” Wavelength electronics. [Online]. Available: <https://www.teamwavelength.com/quantum-cascade-laser-basics/>
- [35] J. R. Meyer, C. A. Hoffman, F. J. Bartoli, and L. R. Ram-Mohan, “Type-II quantum-well lasers for the mid-wavelength infrared,” Applied Physics Letters, vol. 67, no. 6, pp. 757–759, 1995.
- [36] I. Vurgaftman, W. W. Bewley, C. L. Canedy, C. S. Kim, M. Kim, J. R. Lindle, C. D. Merritt, J. Abell, and J. R. Meyer, “Mid-IR type-II interband cascade lasers,” IEEE Journal of Selected Topics in Quantum Electronics, vol. 17, no. 5, pp. 1435–144, 2011.

- [37] J. R. Meyer, W. W. Bewley, C. L. Canedy, C. S. Kim, M. Kim, C. D. Merritt, and I. Vurgaftman, "The Interband Cascade Laser," *Photonics*, vol 7, no. 3, 75, 2020.
- [38] I. Vurgaftman, W. W. Bewley, C. L. Canedy, C. S. Kim, M. Kim, C. D. Merritt, J. Abell, and J. R. Meyer, "Interband cascade lasers with low threshold powers and high output powers," *IEEE Journal of Selected Topics in Quantum Electronics*, vol. 19, no. 4, p. 1200210, 2013.
- [39] A. Lyakh, R. Maulini, A. Tsekoun, R. Go, and C. K. N. Patel, "Tapered 4.7 μm quantum cascade lasers with highly strained active region composition delivering over 4.5 watts of continuous wave optical power," *Optics Express*, vol. 20, no. 4, pp. 4382–4388, Feb 2012.
- [40] A. A. Balandin, S. Ghosh, E. Bao, I. Calizo, D. Teweldebrhan, F. Miao, and C. N. Lau, "Superior thermal conductivity of single-layer graphene," *Nano Letters*, vol. 8, no. 3, pp. 902–907, 2008.
- [41] R. R. Nair, P. Blake, A. N. Grigorenko, K. S. Novoselov, T. J. Booth, T. Stauber, N. M. R. Peres, and A. K. Geim, "Fine structure constant defines visual transparency of graphene," *Science*, vol. 320, no. 5881, pp. 1308–1308, 2008. [Online]. Available: <https://science.sciencemag.org/content/320/5881/1308>
- [42] What is graphene. Digital trend. [Online]. Available: <https://www.digitaltrends.com/cool-tech/what-is-graphene/>
- [43] N. Rumman, "Characterization of Optically Pumped Interband Cascade Lasers," Baylor University, 2019. [Online]. Available: <https://baylor-ir.tdl.org/handle/2104/10718>
- [44] William T. Silfvast, *Laser Fundamentals*, Cambridge, Eng. ; New York, NY, USA : Cambridge University Press, 1996
- [45] Spectra-Physics. Quanta-Ray Lab-Series Pulsed Nd:YAG Lasers User's Manual. [Online]. Available: http://publish.illinois.edu/ae-lambros/files/2017/07/Lab-Series-Users-Manual_Nd_YAG.pdf
- [46] FinLight Blog. What are Optical Parametric Oscillators?. 2017. [Online] Available: <https://www.findlight.net/blog/2017/07/18/optical-parametric-oscillators/>
- [47] Horiba. iHR Series Brochure. [Online]. Available: https://static.horiba.com/fileadmin/Horiba/Products/Scientific/Optical_Components_and_OEM/iHR_Series/iHR_Series_Brochure.pdf
- [48] Horiba. DSS-IS020L Indium Antimonide Solid State Detector Brochure. [Online]. Available: https://static.horiba.com/fileadmin/Horiba/Products/Scientific/Optical_Components_and_OEM/Single_Point_Detectors/Solid_State_Detectors/DS-S-IS020L.pdf

- [49] thinkSRS. About Lock-In Amplifiers. [Online]. Available:
<https://www.thinksrs.com/downloads/pdfs/applicationnotes/AboutLIAs.pdf>
- [50] T. C. McAlpine, "Cavity Length Study of a Resonantly Pumped W-Opic Semiconductor Laser," 2003. [Online] Available:
<https://citeseerx.ist.psu.edu/viewdoc/download?doi=10.1.1.453.7299&rep=rep1&type=pdf>
- [51] L. J. Olafsen and N. Rumman, "Optically-Pumped Mid-Infrared Interband Cascade Lasers," *2020 IEEE Texas Symposium on Wireless and Microwave Circuits and Systems (WMCS)*, Waco, TX, USA, pp. 1-4 (2020).
- [52] L. J. Olafsen and T. C. McAlpine, "Transparency pump intensity and differential gain in resonantly pumped W optical pumping injection cavity lasers," *Journal of Applied Physics* 108 053106 (2010)